AN APPROXIMATE METHOD FOR REAL TIME HEALTH MONITORING AND DAMAGE ASSESSMENT OF MID-TO-HIGH RISE REINFORCED CONCRETE BUILDINGS

by

Selahattin Akalp

B.S., Civil Engineering, Gaziantep University, 2011

M.S., Civil Engineering, Boğaziçi University, 2015

Submitted to the Institute for Graduate Studies in
Science and Engineering in partial fulfillment of
the requirements for the degree of
Master of Science

Graduate Program in Civil Engineering

Boğaziçi University

2022

ACKNOWLEDGEMENTS

I would like to sincerely thank my thesis supervisor Prof. Cem Yalçın for his help, guidance and friendly encouragement.

I would like to express my gratitude to my thesis progress members Prof. Ercan Yüksel and Prof. Hilmi Luş for their support.

I would also like to thank my friends Burak Horoz, Tarık Tufan, Ferit Yardımcı, and Ziya Dalkılıç who helped broadening my perspective with their valuable comments and critics.

ABSTRACT

AN APPROXIMATE METHOD FOR REAL TIME HEALTH MONITORING AND DAMAGE ASSESSMENT OF MID-TO-HIGH RISE REINFORCED CONCRETE BUILDINGS

Two separate methods are proposed and evaluated in this study for the structural health monitoring and damage detection of mid-to-high rise reinforced concrete buildings. The first method discussed herein, aims to predict the response of the structure at non-instrumented floors. A numerical structural model of the real-life structure is constructed and the modal response quantities are retrieved. The measured mode shapes of the real structure are considered as linear combination of the calculated mode shapes of the numerical model. For each mode shape to be superimposed, a weighting coefficient is obtained through minimizing the error between the actual and superimposed mode shapes and the final response is estimated by using the relation between the physical and modal coordinates. The second method is based on wave propagation in buildings and reverse nonlinear structural analysis. The building floors are first scanned with limited number of sensors and the impulse response function (IRF) for each story is identified by deconvolution. Once the IRFs are determined, the story responses are obtained via convolution of the reference signal and the story IRFs at any given instance; and finally, the interstory drifts are approximated. The internal forces and deformations of the structural members are computed by the reverse inelastic structural analysis utilizing nonlinear fiber models, kinematic, and joint equilibrium. The extent and limits of convolution operation as for inelastic structural response is investigated. The change in the shear wave velocity of the damaged are also evaluated.

ÖZET

ORTA YÜKSEKLİKTEKİ VE YÜKSEK BETONARME BİNALARIN YAPI SAĞLIĞI İZLEMESİ VE HASAR DEĞERLENDİRMESİ İÇİN YAKLAŞIK BİR YÖNTEM

Bu çalışmada, orta yükseklikteki ve yüksek betonarme binaların yapı sağlığı izlemesi ve hasar tespiti için iki farklı yöntem geliştirilmiştir. Bu yöntemlerden ilki yapıda ölçüm cihazlarının bulunmadığı katlardaki yapısal tepki niceliklerini hesaplamayı amaçlamaktadır. Binanın bir nümerik modeli oluşturulur ve modal parametreler bulunur. Gerçek binanın ölçülen mod şekilleri, nümerik modelin mod şekillerinin doğrusal birleşimi olarak kabul edilir. Ölçülen ve nümerik modele ait mod şekilleri arasındaki farkın minimize edilmesi ile nümerik mod şekillerinin ağırlık katsayıları bulunur. Daha sonra mod koordinatları ve fiziksel koordinatlar arasındaki bağıntı kullanılarak ölçüm cihazlarının olmadığı katlardaki yapısal tepkiler hesaplanır. İkinci yöntemde ise binadaki sismik dalgaların yayılımından yararlanılır. İlk aşamada binanın farklı katları sensörler ile taranır ve her katın itki tepki fonksiyonu ters evrişim (dekonvolüsyon) yöntemiyle belirlenir. Herhangi bir yükleme altında katlardaki tepki niceliki, referans sinyal ve kat itki tepki fonksiyonlarının evrişimleriyle (konvolüsyon) hesaplanır ve göreli kat ötelemeleri yaklaşık olarak elde edilir. Doğrusal olmayan lif modeli ve düğüm noktalarındaki denge koşulu gözetilerek, doğrusal olmayan ters yapısal analiz algoritması yapısal elemanlardaki iç kuvvet ve şekil değiştirmeleri hesaplar. Bu çalışmadaki bir diğer önemli husus ise; yapıyı elastik sınırları aşmaya zorlaycak yüklemeler altında evrişim fonksiyonunun kullanılabilirlik sınırlarını araştırmaktır. Herhangi bir malzemenin rijitlik değeri ile doğrudan ilişkili olan kayma dalgası hızı da, hasarlı ve hasarsız nümerik modeller için incelenmiştir.

TABLE OF CONTENTS

LIST OF FIGURES

LIST OF TABLES

LIST OF SYMBOLS

a	The distance between the i-end and PI
$a_m(t)$	Measured accelerations at the measured DOFs
$a_p(t)$	Predicted accelerations at the non-instrumented DOFs
C	Constant
C_{kj}	The weighting coefficient for the mode j and story n
C_{Nj}	The weighting coefficient for the mode j and story N
$D_j(t)$	Modal displacement for the mode j
d	Distance between the roof and the story of interest
$d_j(t)$	Amplitude of the downgoing wave at layer j
E_c	Modulus of elasticity of concrete
f_1	Natural frequency of the fixed-base structure
f'_c	Concrete compressive strength
f_{cr}	Tensile strength of concrete
f_j	Natural vibration frequency of the j^{th} mode
f_{sys}	Natural frequency of the structure-soil system
g	Gravitational acceleration
H	Height of the building or column
h_{beam}	Depth of the beam
h_{col}	Depth of the column in the direction under consideration
h_j	Thickness of the layer
$\hat{h}(\ .)$	Transfer function of (.)
j	Mode number
L	Span length
M^i	Bending moment on the i story column
M^{i+1}	Bending moment on the i+1 story column
M_w	Moment magnitude
N^i	Axial force on the i story column
N^{i+1}	Axial force on the i+1 story column

n	Story number
$q^{(t)}$	Response in modal coordinates
R	Strength reduction factor
$R(\tau)$	Autocorrelation function corresponding to time lag τ
$R_{d,\ j-1}$	Reflection coefficient for the downgoing wave at interface j-1
T	Fundamental period of vibration
$T_{u,\ j-1}$	Reflection coefficient for the upgoing wave at interface j-1
t_1	Assumed zero velocity time at the beginning of the record
t_2	The intermediate time that separates the two baselines
t_{cut}	The intermediate time that separates the two baselines
t_{total}	Total duration of the earthquake
u	Horizontal displacement at the story of interest
$u_j(t)$	Amplitude of the upgoing wave at layer j
$u_n(t)$	Physical displacement of the n^{th} story
$\hat{u}(\ .)$	Fourier transform of (.)
V	Apparent transmission velocity
V_j	Shear wave velocity in the layer j
V_s	Shear wave velocity
y	The distance from j-end of the member
$\ddot{y}_{j,k}(t)$	The estimated modal acceleration of the mode j and story k
z	Elevation of the story of interest
z_{ref}	Elevation of the story to be used as reference
$\ddot{z}_{j,k}(t)$	The calculated modal acceleration of the mode j and story k
α	Column to beam pseudo stiffness ratio
Δ_e	Elastic displacement
Δ_i	Lateral displacement at the joint i
Δ_j	Lateral displacement at the joint j
Δ_{max}	The displacement of the corresponding inelastic system
Δ_N	The lateral displacement of the column end at N^{th} story
Δt	Time step

Δ_{TOP}	Top displacement
Δ_y	Yield displacement
$\hat{\Delta}_{Nj}$	Lateral column displacement for story N, mode j
ε_{cr}	Cracking strain of concrete (average)
$\varepsilon_j(t)$	The error for the mode j
ε_r	Tensile concrete strain
ζ	Damping ratio
θ_i	Rotation at joint i
θ_j	Rotation at joint j
θ_N	Joint rotation of the column end at N^{th} story
θ_p	Plastic rotation
$\hat{\theta}_{Nj}$	Joint rotation of the column end at N^{th} story for the j^{th} mode
μ	Ductility factor
σ_r	Concrete tensile stress
τ	Time lag
τ_j	One-way travel time of the waves in layer j
τ_{tot}	Wave travel time from the base to the top of the structure
$\varphi(y)$	Curvature in the structural member at a distance y
Φ_m	Mode shape matrix at the measured DOF $m\Phi_m^*$
Φ_m^*	Pseudo inverse of the mode shape at the DOF m
Φ_p	Mode shapes obtained through finite element model
$\phi_{i,m}$	i^{th} mode shape at the measured DOF m
$\phi_{nj}(t)$	The measured mode shape for the mode j and story n
$\hat{\phi}_{nj}(t)$	The model mode shape for the mode j and story n
ω	Angular frequency
F	Fourier transform
Y	Location of the PI as a fraction of height of the column

LIST OF ACRONYMS/ABBREVIATIONS

ACF	Autocorrelation Function
ASCE	American Society of Civil Engineers
ARX	Autoregressive Exogenous
EFDD	Enhanced frequency Domain Decomposition
FEMA	Federal Emergency Management Agency
FDD	Frequency Domain Decomposition
GPS	Global Positioning System
IIRF	Instantaneous Impulse Response Function
IRF	Impulse Response Function
LVDT	Linear Variable Differential Transducer
MDOF	Multi Degree of Freedom System
MSBE	Mode Shape Based Estimation
NIF	Number of Instrumented Floors
PGA	Peak Ground Acceleration
PGD	Peak Ground Displacement
PI	Point of Inflection
PSD	Power Spectral Density
RC	Reinforced Concrete
RMS	Root Mean Square
SHM	Structural Health Monitoring
SDOF	Single Degree of Freedom System
SSI	Soil Structure Interaction

1. INTRODUCTION

1.1. General

Structural earthquake engineering has received considerable interest from the researchers in the last couple of decades. Despite the inherent identifiable and unidentifiable uncertainties, the extremely fast-paced technological developments fortunately enabled researchers to widen the perspective and detect crucial parameters in this field. Evidently, a vast portion of the available literature in this field is produced recently due to the developments in hardware and software technology. One of the latest end-product of this process is the system identification and its implementations on the structural engineering, so called structural health monitoring (SHM). The SHM not only facilitates the identification of dynamic properties of a structure, but also alleviates uncertainty problems in modeling issues and hence provides significant information for robust and accurate modeling of the real-life civil engineering structures. Furthermore, it offers non-destructive and automated damage detection techniques along with condition assessment and determination of failure probabilities under particular events. On a mass-scale, the SHM can also be utilized in the derivation of fragility curves and resulting shake maps for a given region. Concisely, for both micro and macro scales, the SHM is a fruitful tool for identification, assessment, and decision making steps for the civil engineering structures. To be more specific for the scope of this document, the SHM applications in tall buildings are investigated. The increase in the tall building construction in metropolitan areas and their economic significance, not to mention the value of the life safeties of the occupants, enforce the investors and the insurance companies to assess those building' safety and risk issues. The condition of the building is needed to be determined under service loads, such as daily or seasonal changes in the temperature or wind speeds. In addition, during or after unusual or severe events (can be earthquake, strong wind loading, blast loadings) the structure must be rapidly assessed and decisions on the operational systems (e.g. the gas or the electric network), as well as decisions on the evacuation of the building must be

made. Considering complicated and unique natures of the tall buildings, the need for an automated system identification based rapid assessment method for tall buildings arises. This thesis proposal is devoted to seeking for possible solutions for the real time structural health monitoring of tall buildings by seismic interferometry and system identification techniques.

1.2. Literature Review

As mentioned earlier the interstory drift ratios are one of the widely accepted damage indicators. The interstory drift ratios can be used to derive fragility functions or assess the current situation of a given building. However, the difficulties and uncertainties constitutes its problematic nature. A study conducted [1] is devoted to identify a building's real-time or near real-time dynamic characteristics and retrieve fragility functions (probabilistic damage state estimations) by means of the interstory drifts ratios. A four-story reinforced concrete building damaged during the 1994 Northridge earthquake is instrumented by tri-axial accelerometers and LVDTs. By the help of two eccentric mass shakers, forced vibration tests are conducted for the two translational (NS and EW) directions and also for the torsional motion. The configuration of the sensors can be seen from the Figure 1.1. Four tri-axial accelerometers are attached to the floor levels and three LVDTs were used at the two uttermost floors. The LVDTs are used along with the diagonal piano wires and the interstory drifts are attained from the lengthening/shortening of the wire. During the tests it is reported that the interstory drifts obtained by double integration can end up with unexpected large drifts due to inherent baseline offsets observed in the acceleration data. On the other hand, for the direct measurement data (LVDTs), several problems such as random piecewise shifts (offsets) and peak capping is observed. The underlying reasons for these two inconveniences are probably arising from the mechanical slips and wire slacks (especially for long spans).

Depending on these full-scale forced-vibration tests they concluded that new methods for directly measuring the interstory drifts are required due to the short-

comings of the current procedures. Moreover, it is declared that several studies involving alternative procedures such as non-contact (laser/2D-photodiodes) techniques are being investigated.

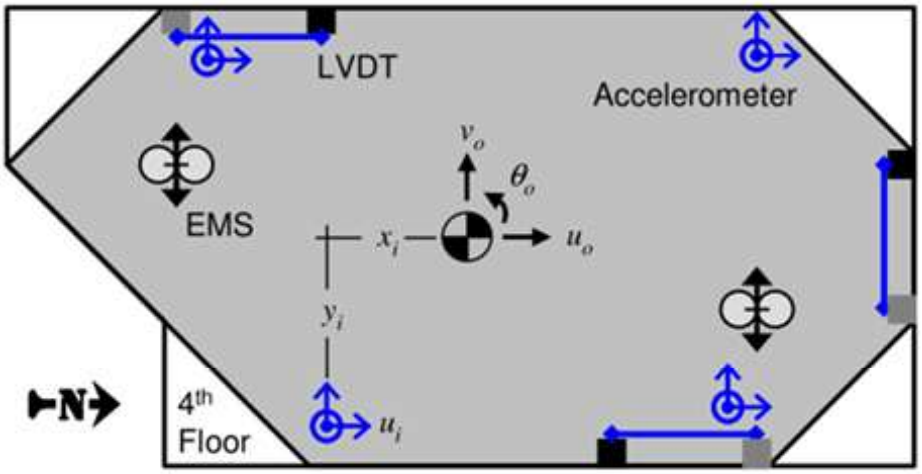

Figure 1.1. The sensor configuration of the 4-story RC building [1].

In a similar vein, another way of reliably estimating the displacement responses is utilizing the known mode shapes of a given building, especially at the sparse (non-instrumented) floors [2]. Suggested a method for constructing drift spectra for buildings exposed to near-fault excitations by assuming a linear shear beam model, for which the shear strain in the equivalent shear beam is considered to be analogous to the interstory drift. Addressing the displacement spectrum, it should be noted that the maximum interstory drift and the maximum global displacement of the system may not occur simultaneously. Furthermore, unlike the broad-band frequency content of other earthquakes, the pulse-like nature of the near-field excitations can cause the structure to reach its maximum response before a resonant-like mode shape is formed. Regarding the aforementioned facts, the SDOF-based displacement spectra may not meet the accuracy expectations for interstory drifts in the case of near-field earthquakes. Thus, instead of modal solution non-dispersive damped wave formulations are adopted for a 1D continuous medium. However, the method used herein will then be cited by other studies which employ the modal solutions. Similar to Iwan's drift spectrum [3],

proposed a generalized drift spectrum by assuming the response of the building as a combination of linear-elastic shear and flexural beams. Besides, in order to solve the residual drift problem is Iwan's drift spectrum they introduced the modal (classical) damping to the system. Assuming uniform mass and stiffness along the height, the shear and the flexural beams are assumed to be connected by infinite number of axially rigid links so that both of the beams experience the same transverse (lateral) deformation at the same heights. The schematic representation of the continuum model can be seen in Figure 1.2. Once the model is constructed modal analysis is performed and total responses for a given earthquake is computed by the mode superposition method for which the interstory drift ratio of a certain story is approximated by the rotation of the model at the mid-height of that story.

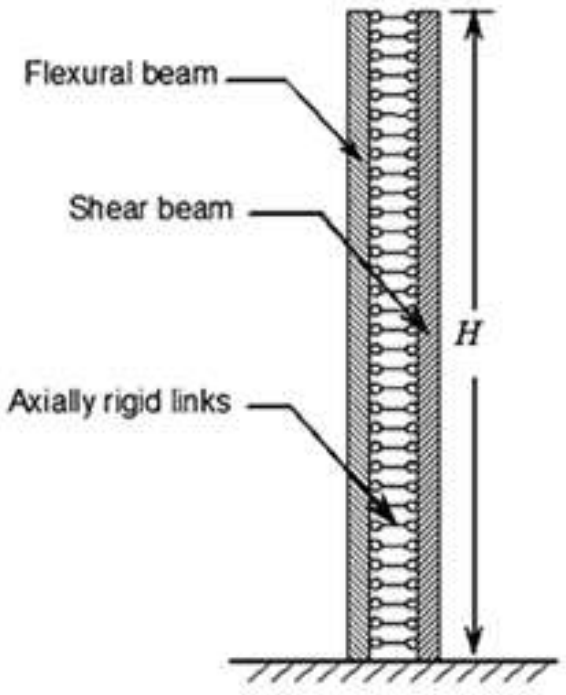

Figure 1.2. The continuum model including both the shear and flexural models [3].

As the ideal case, instrumentation of all the floors in a building is the best option. However, considering the current amounts of the initial and the operational (as well as maintenance) cost, it may not be a feasible practice especially for the tall buildings. Thus, it would be safe to say that almost all of the buildings are sparsely instrumented

along their heights. Referring to this problem in tall buildings [4], proposed a method for estimating the mode shape amplitudes and the associated floor responses for non-instrumented floors. The mode shapes are assumed as a linear combination of the mode shapes of the shear beam and the bending (flexural) beam as shown in the Eq. 1.1. The relative contributions, or namely the weighting factors, of the bending and the shear beams are obtained by minimization of the error function. The error function (Eq. 1.2) is obtained through summation of the squares of the differences between the measured and the calculated modal responses over the instrumented floors. The measured modal responses are obtained by narrow band-pass filtering around the identified modal frequencies

$$\phi_{j,k} = C_{s,j} \cdot \phi_{s,j,k} + C_{b,j} \cdot \phi_{b,j,k} \tag{1.1}$$

$$\varepsilon_j(t) = \sum_{k=1}^{NIF} \left[\ddot{z}_{j,k}(t) - \ddot{y}_{j,k}(t)\right]^2. \tag{1.2}$$

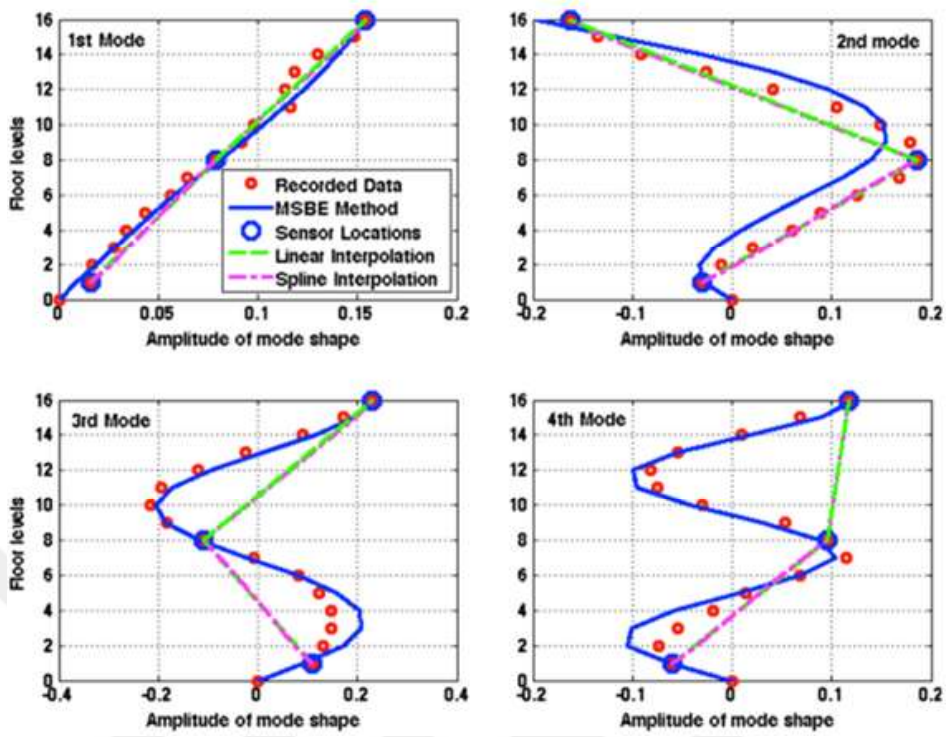

Figure 1.3. Comparison of various mode shape estimation methods for the 17 story UCLA Factor Building [4].

Once the error is minimized, the relative contributions and hence the estimated mode shape of the building is acquired and the floor responses of the non-instrumented floors are computed by mode superposition for a given earthquake excitation. The proposed method is compared to other available mode shape estimation methods, such as linear and cubic interpolation approaches. The drawback of the interpolation approach is their substantial sensitivity to the location of the instrumented floors. In order to capture the higher mode shapes effectively when adopting cubing interpolation method, the building must be instrumented regularly along the height and additional sensors must be placed at the floors where mode shape changes sign (point of contra-flexures). In Figure 1.3, the first four mode shapes yielded by the proposed method and the interpolation methods are shown. The mode shapes of a 17-story steel moment-frame building is estimated by using the acceleration data gathered from three floors only. It can be observed that, the discrepancy between the measured data and the interpolation methods are prominent for higher modes. Nonetheless, the proposed method is more

stable and yields relatively good results for a 17-story building instrumented at only three floors. Eventually, the proposed method can be a useful tool for the response estimation non-instrumented floors.

Iliopoulos developed a multi-band modal expansion technique in an effort to conduct structural health monitoring and fatigue assessment of offshore wind turbines in case of limited number of sensors. The method relies on the utilization of the modal decomposition of a calibrated finite element model and predicts the responses at the points where no sensors exist. The procedure can be followed through Eq. 1.3-Eq. 1.5 as demonstrated below

$$\mathbf{a_m}(t) = \sum_{i=1}^{n} \phi_{i,m} q_i(t) \tag{1.3}$$

In the Eq 1.3, $\mathbf{a_m}(t)$ is the measured accelerations at the time instance (t), n is the number of modes under evaluation, $phi_{i,m}$ is the mode shape amplitudes at the points of measurement, and $q_i(t)$ is the response in the modal coordinates. The mode shapes can be retrieved from the finite element model. In the latter step, the relation between the modal coordinates and the physical coordinates is used. A point which deserves to be emphasized herein is that the number of modes under consideration cannot be greater than the number of instrumented points

$$\mathbf{q}\,(t) = \left(\Phi_m^T \Phi_m\right)^{-1} \Phi_m^T \mathbf{a_t} m\,(t) = \Phi_m^* \mathbf{a_m}\,(t)\,. \tag{1.4}$$

In the Eq 1.4, m stands for the measured points and Φ_m^* is the pseudo inverse of the mode shape matrix of the measured DOFs. Combining the Eq. 1.3 and Eq. 1.4, the acceleration values at the non-instrumented points (p) can be estimated as follows where the Φ_p is the mode shapes obtained through the finite element model:

$$\mathbf{a_p}(t) = \Phi_p \mathbf{q}\,(t) = \Phi_p \Phi_m^* \mathbf{a_m}\,(t)\,. \tag{1.5}$$

The effort for estimating the response quantities at non-instrumented floors actually are not a concern that has appeared recently. In 1963 [6], developed a simple (and yet robust) formula based on the multiple reflection of waves through the elastic medium. The study showed that under a seismic excitation it is possible to estimate

the response at the foundation level (or the response at any desired building level) of a building from the measured top response of the building under consideration. The aforementioned formula (the derivation is not shown here) and the associated parameters can be seen through Eq. 1.6 and Figure 1.4

$$u_{z=0}\left(t - H/V\right) = 0.5u_{z=H}\left(\tau\right) + u_{z=H}\left(\tau - 2H/V\right). \tag{1.6}$$

In the Eq 1.6, H is the total building height, V is the apparent transmission velocity, τ is the time instant, z is the vertical axis whose origin is the base of the structure, and $u_{z=0}$ and $u_{z=H}$ are the amplitudes of motion at the foundation level (base) and the top of the structure, respectively. The advantage of the method is that the only parameter utilized in the Eq. 1.6 is the 2H/V without needing any other geometric properties or the constants in order to obtain the response at the base of the structure.

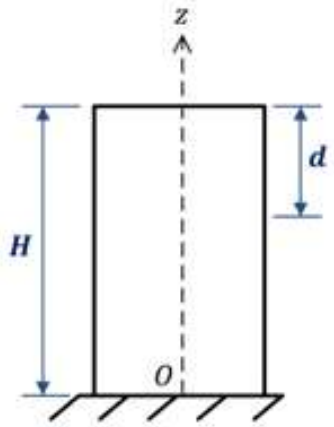

Figure 1.4. The parameters used in [6] formula and its generalized version in [7].

The authors suggest that one of the alternatives to estimate the above parameter is the simple relationship illustrated in Eq. 1.7

$$T = 4H/V, \tag{1.7}$$

In the Eq 1.7, T is the predominant period of vibration of the cantilever shear beam.

Ebrahimian expanded the [6] formula to be able to preict the response of any given story in the building and tested the success of the method on 54 instrumented buildings located in the Los Angeles area. It should be kept in mind that the formula of interest was derived assuming the building behaves in a linear-elastic manner and the deformations caused by only shear. The generalized version of the Kanai and Yoshizawa formula updated [7] is given in Eq. 1.8 where the only additional parameter is d being the vertical distance between the top of the building and the location of the floor under evaluation. Although the concept of the impulse response function

$$u\left(H-d,t\right)=\frac{1}{2}u\left(H,\ t-\frac{d}{V}\right)+u(H,\ t+\frac{d}{V}). \tag{1.8}$$

(IRF) and seismic interferometry will be introduced in the forthcoming pages, it might be a good idea to briefly mention about the IRF approach due to its resemblance with the Kanai and Yoshizawa formula in terms of end products. Assume that a structure is being monitored and instrumented at several floor levels. Select one of the records at any height and consider it as the source (or reference) and call it z_{ref} while another z stands for the height of the other floor response and their Fourier transforms are $\hat{u}\left(z;\omega\right)\&\hat{u}\left(z_{ref};\omega\right)$, respectively. The transfer function of these two responses will be as in Eq. 1.9 and the inverse Fourier transform of the transfer function $\hat{h}$ is the IRF of the floor response at the elevation of z with respect to the reference signal with an elevation of z_{ref} as given in Eq. 1.10

$$\hat{h}\left(z,\ z_{ref};\omega\right)=\frac{\hat{u}\left(z;\omega\right)}{\hat{u}\left(z_{ref};\omega\right)} \tag{1.9}$$

$$IRF=h\left(z,\ z_{ref};t\right)=\mathcal{F}\left(\omega\right)^{-1}\left\{\hat{h}\left(z,\ z_{ref};\omega\right)\right\}. \tag{1.10}$$

Once the IRF is obtained as shown in Equation 1.10, the response of the floor at the level z can be retrieved by convolving the IRF at z with the corresponding record at the z_{ref} under any given excitation as the IRF is the response at z produced by a unit impulse at the level z_{ref}. The convolution operation is explained via Eq. 1.11. In order to help visualizing

$$u\left(z;t\right)=u\left(\ z_{ref},\ t\right)*h\left(z,\ z_{ref};t\right). \tag{1.11}$$

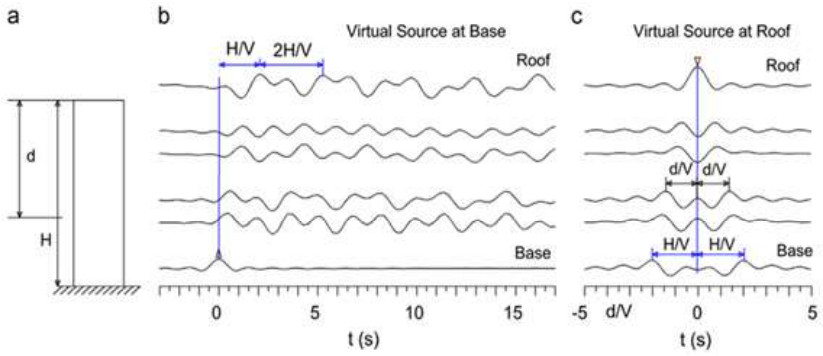

Figure 1.5. The IRFs at various points of a cantilever beam (a) derived with respect to; (b) base and (c) with respect to roof [7].

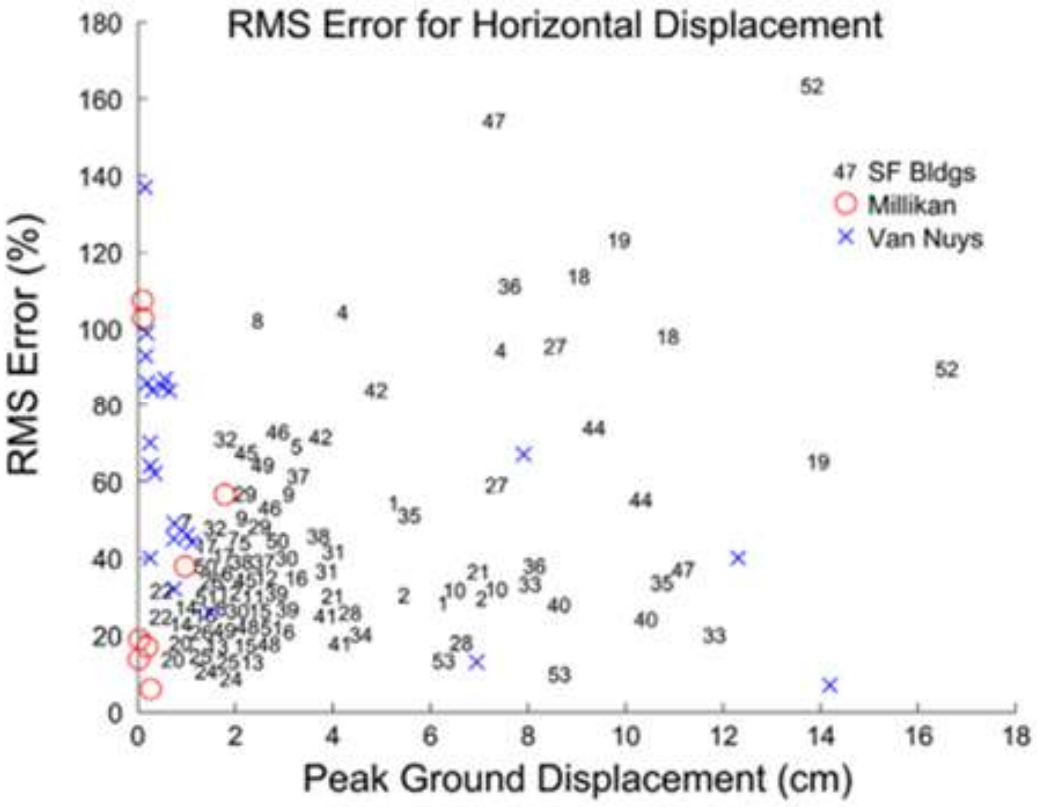

Figure 1.6. PGD and RMS error for the horizontal displacements of 54 buildings [7].

This process, Figure 1.5 can be examined where the IRF of a uniform cantilever beam is illustrated. The comparison between the estimated and recorded story dis-

placements of a 54-story office building located in Los Angeles is depicted in Figure 1.7. Overall, the RMS errors for all of the 54 buildings can be viewed in Figure 1.6 which seem to be less than 60% for most of the buildings. More detailed results for each building in the database can be found in the report prepared by [8].

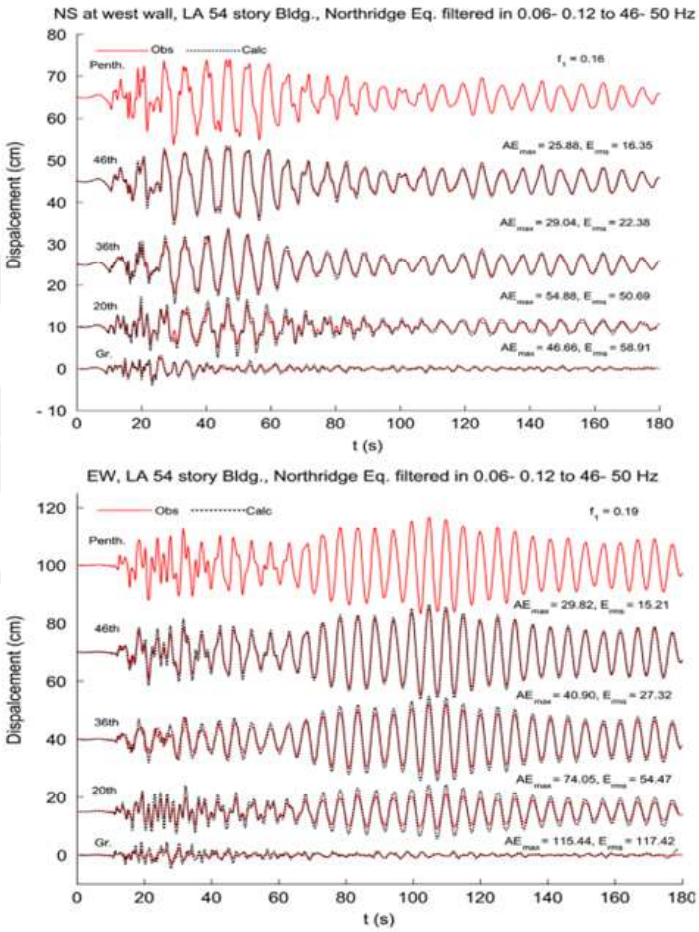

Figure 1.7. The estimated and recorded story displacements at various floor levels of a 54-story office building located in Los Angeles [7].

Another study involving the interstory drifts is conducted [9] and focuses on deriving simple analytical expressions for the interstory drift and velocity profiles, as well as their peak values which can be used in the preliminary design phase of the structures with interstory viscous dampers. The analytically derived first mode shape profiles are used to estimate the peak interstory drifts and the velocity values. Then, by using numerous spectrum-compatible artificial ground motions parametric studies

are conducted by to assess the validity of the method and to understand the crucial parameters. The linear-elastic building models varying between 5-30 stories are exposed to the time history analyses and modification factors are developed for the peak interstory drifts and velocities. It is concluded that the peak interstory velocity values for high-period structures cannot be accurately estimated via the first mode response. These velocities tend to be higher especially at the bottom stories due to contribution of higher modes. Another remark to be stated is that the equivalent lateral force method of the ASCE 7-10 Chapter 17 estimations is non-conservative for the intermediate stories and conservative for the bottom and the top stories in terms of interstory drifts and velocities. A different but related aspect in conjunction with the lateral drift demands can be attributed to the design spectrum estimates. Cracking in reinforced concrete structural members, loosening of the partition walls, interaction between the structural and non-structural members, nonlinearities in the foundation response, and the severity of the excitation can have significant influence on the predominant period of a building. On the other hand, one of the most complicated and somehow elusive parameters is the damping which incorporates various kinds of energy dissipating mechanisms. Therefore, better estimates of the predominant period (T_p) and the equivalent damping ratio (ζ_e) suggest more reliable estimates of earthquake drift demand [10]. Proposed a method for estimations of these parameters by performing full-scale shake table test for a 5-story reinforced concrete building, one with fixed-base and the other with base isolation. Three different system identification methods are utilized to extract the above parameters, which are: The transfer function method, the roof-to ground spectral ratio method, and time-domain optimization method which linearizes the building response obtained from the GPS data and obtain the T_p and the ζ_e. As a result, it is concluded that all of the three identification methods yield almost the same predominant periods. Another point deserves to be emphasized that for the fixed-base structure, the effective stiffness can reduce up to 16% of the initial stiffness during several earthquake excitations and after the events 40% of the effective stiffness is recovered and the final effective stiffness is reported as 56% of the elastic stiffness. As a concluding remark, after a relatively slight earthquake where no yielding is observed, the identified equivalent viscous damping ratio is between 4.3-7.0% whereas it is 1%

for the ambient vibration case.

In addition to interstory drifts, some studies suggest that damping is also a damage indicator. Particularly for large structures, significant changes in the overall stiffness may not necessarily imply visible or discernible shifts in the frequencies [11]. Suggest that 21% drop in the bending stiffness of the I-40 bridge does not lead a substantial decrease in the modal frequencies. Based on that [12], conducted a study in order to be able to detect the structural damage by following the change in the instantaneous damping. First, the recorded accelerations are processed by random decrement method and the decay of motion is obtained. The system is modeled as an oscillator with nonlinear restoring and damping force which is expressed as:

$$\ddot{x} + 2h_o\left(\dot{x}\right)\dot{x} + k\left(x\right)x = 0. \tag{1.12}$$

By using the multiplication property of the Hilbert Transform, the instantaneous undamped frequency and coefficient can be as follows:

$$\omega_o^2 = \omega^2 - \frac{\ddot{A}}{A} + 2\frac{\dot{A}^2}{A^2} + \frac{\dot{A}\dot{\omega}}{A\omega}. \tag{1.13}$$

$$h_o = -\frac{\dot{A}}{A} - \frac{\dot{\omega}}{2\omega}. \tag{1.14}$$

Having specified that, the instantaneous amplitude and the phase is computed from wavelet transforms and plugged into the Eq. 1.12, and then the change in the damping is observed. The validity of the proposed method is tested via a simply supported reinforced concrete beam and an aluminum 3D frame model experiments. Perceivable changes in the damping coefficient is observed during the incremental dynamic tests while slight changes in the frequencies are reported. The test result for the beam is illustrated in Figure 1.8.

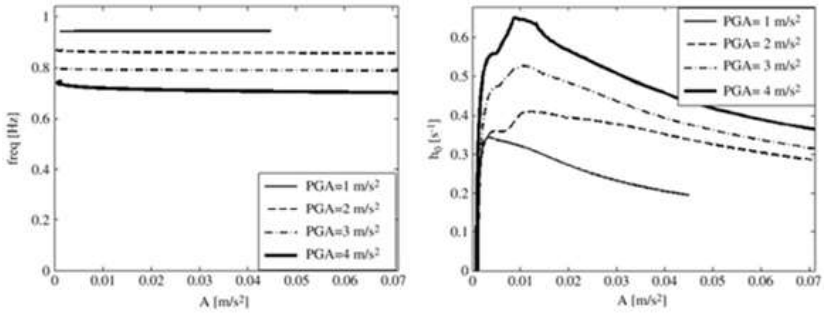

Figure 1.8. The change in the frequency and the instantaneous damping coefficient for the beam experiment [12].

Uebayashi made an endeavor to come up with simple expressions for the stiffness degradation and the peak interstory drift ratios (PIDR) of tall buildings by relating the pre-event and post-event dynamic characteristics gathered from ambient vibration tests. 13 tall buildings experienced the 2011 Tohoku-Oki Earthquake and the 1995 Hyogoken-Nanbu Earthquake are modeled as SDOF system with bilinear stiffness degradation. As the final products, the stiffness degradation rates and the peak interstory drift values are expressed as simple relations (which are functions of pre-event and post-event first mode frequencies) estimated from regression analyses based on the natural frequencies. The natural frequencies are identified by the ARX model under ambient vibrations. The interstory drifts used in the regression analyses are adopted as the gradient of the broken lines for the available displacement measurements shown in the Figure 1.9. The Eq. 1.5-Eq. 1.6 are the final estimations of the proposed method

$$\frac{k_e}{k_o} = (0.91\alpha)^2 \times (\frac{f^{after}}{f^{fore}})^2 \tag{1.15}$$

$$PIDR = \frac{4.0 \times 10^{-4}}{(k_e k_o) - 0.32}. \tag{1.16}$$

It should be kept in mind that the proposed relationships are derived for buildings dominated mainly by the first mode responses and can yield unreliable results for buildings with significant higher mode contributions.

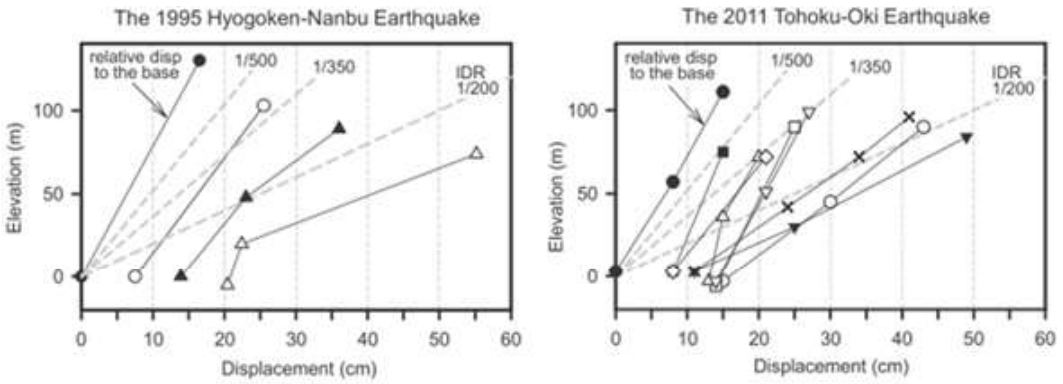

Figure 1.9. Distribution of the maximum displacements along the height [13].

As stated earlier, obtaining the displacement responses based on the double integration of acceleration time histories are somehow problematic. Although it is possible to implement alternative techniques, each of which constitutes various problems. For example, GPS measurement is a widely accepted way of measuring the roof displacement responses there are several factors influencing the efficiency, such as the satellite visibility, availability, and the geometry, signal quality, and the delay of GPS waves [14]. Therefore [14], presents a method to obtain the structural deformations via the real-time strain data of the structural members. The proposed method is applied to the 600 m-tall Canton Tower whose plan view and the strain sensor configurations are depicted in Figure 1.10. Four strain gauges are mounted at 11 various cross sections of the inner tube (wall) along the height of the building. The method of virtual work is used to calculate the rotation and the displacement for a specified point by the help of strain data. The virtual work is formulated for only bending deformations. For non-instrumented floors, the strain data is estimated by interpolation.

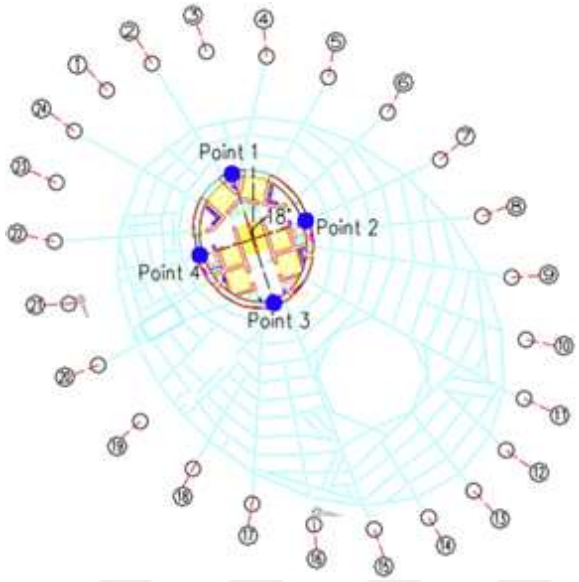

Figure 1.10. The plan view and the configuration of strain sensors attached to the core wall [14].

Afterwards, the results are compared to the those of GPS and inclinometer results which is demonstrated in Figure 1.11 and Figure 1.12.

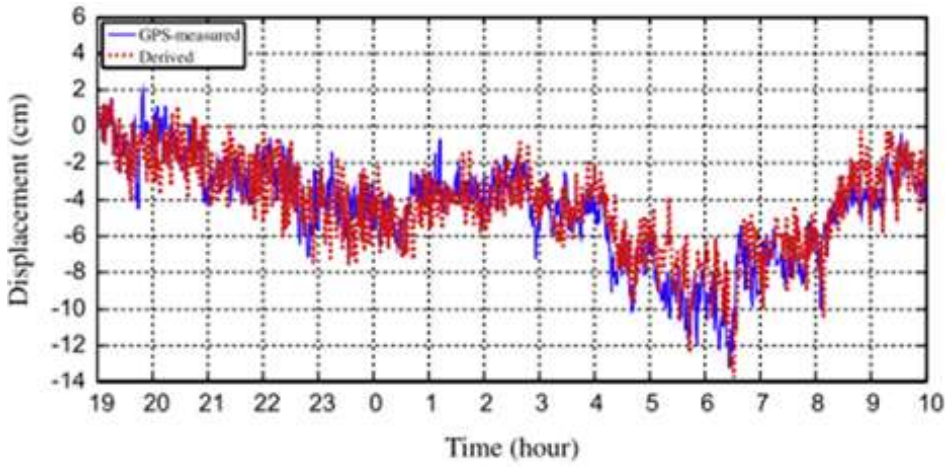

Figure 1.11. The measured and the derived typhoon-induced top displacements [14].

It is worth emphasizing that, the observed typhoon-induced and the temperature-induced maximum daily displacements are almost similar.

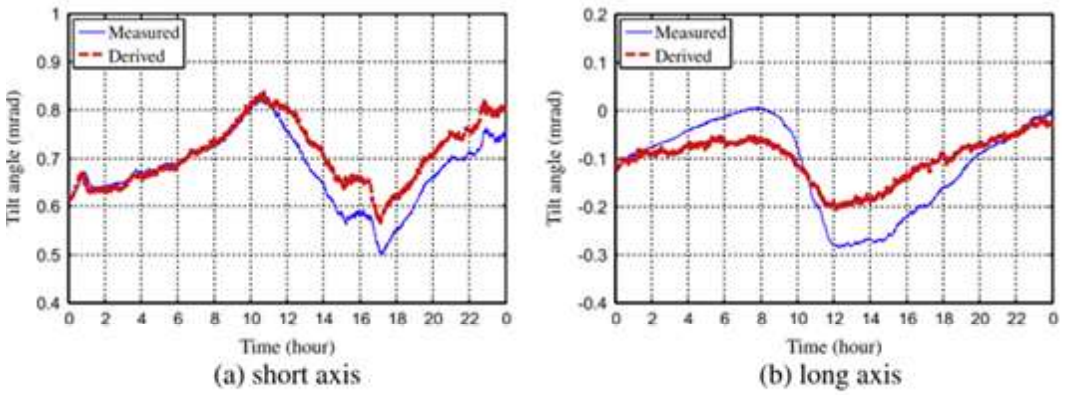

Figure 1.12. The measured and the derived tilts at the height of 443.4 m [14].

As the real-time health monitoring becomes increasingly popular, many recent studies are devoted to this issue [15]. Propose to develop a near-real time system identification method covering a wide range of situations (stationary, weakly non-stationary, or highly non-stationary events) for the Burj Khalifa Tower. For the non-stationary processes (wind storms, earthquakes, or time-varying traffic loadings) the wavelet transform-transformed singular value decomposition (WT-TSVD-Laplace) and for the stationary events (extratropical winds or ambient vibrations) the covariance driven stochastic subspace algorithm (SSI-Cov) is used for system identification purposes. It was reported that the window length is not critical for the WT-TSVD-Laplace as it uses local information of the data whereas very short windows for the SSI-Cov causes substantial uncertainities, particularly on the damping estimations.

In order to develop a benchmark addressing the soil structure interaction (SSI) effect on the health monitoring of tall buildings [16], presented a study on the quantification of rocking motion and its contribution to the building's response. The 83.7 m-tall MIT Green Building is heavily instrumented and used as a test bed. The collected data contains 4 sets of ambient vibrations, 1 earthquake event, 1 unidentified event, and the July 4^{th} fireworks. The slabs and the foundation are assumed to be rigid implying that the rocking is a rigid body motion. The modal characteristics are identified by the second order blind identification (SOBI) method. The translational rocking responses are expressed as $\widetilde{u}_o(h) = \alpha_o h and \widetilde{v}_o(h) = \beta_o h$ (Figure 1.13).

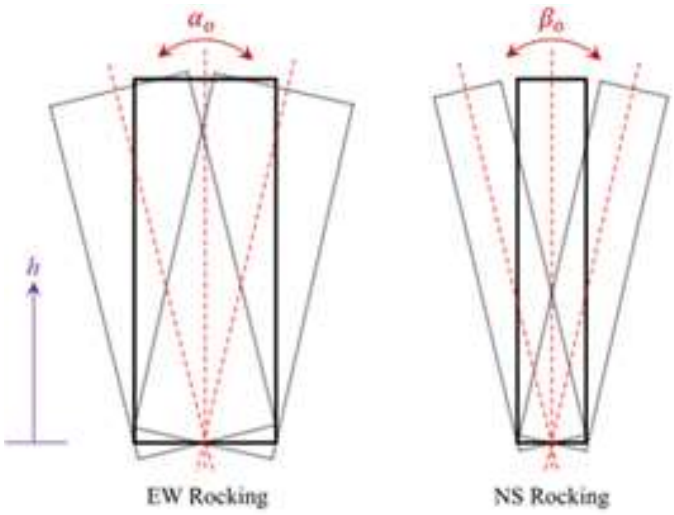

Figure 1.13. The schematic representation of the rocking motion [16].

Then, the story accelerations are condensed at the center of mass. An augmented measurement vector, which constitutes both the condensed translational and rocking responses, is constructed. The coupled deformation-rocking mode shapes are directly identified from these augmented vectors via the blind source separation (BSS) algorithm, whereas the deformation (uncoupled) mode shapes are obtained by the difference between the coupled and the rocking mode shapes. As a result, 11.9% and 30.7% of the modal roof responses are concluded to be of the rocking motion for the EW (strong direction) and the NS (weak direction), respectively.

One of the promising approaches in structural health monitoring is the seismic interferometry which has recently drawn the attention of structural engineers due to its robustness. The application of the seismic interferometry can be deemed somehow "brand new" in structural health monitoring as its main field of application has been other branches of science for long years". The method essentially deals with the determination of the wave propagation behavior through a continuous medium. The most widely used approach among the academics and professionals for determination of the seismic response is the solution of the equation of motion which requires a detailed knowledge of mass, stiffness, and damping properties as well as their correct distribution in the structure, and of course, a profound background in modeling. However,

wave approach is also a good alternative which facilitates the computation of seismic response as it is the seismic waves propagates into the structure which cause the vibration. The wave approach had previously been introduced in the previous studies. In such an endeavor, the study conducted [17] focused on defining the response of buildings with structural walls based on the wave propagation approach and they selected two dimensional continuous models. The study investigates the effect of various structural wall configurations and come up with suggestions regarding the design [18]. Investigated the wave propagation in tall buildings with a similar approach and reached significant findings such as how the seismic waves excite both symmetric and antisymmetric modes even in a perfectly symmetrical structural configuration. Note that both studies neglected the soil structure interaction (SSI).

The study conducted by Safak [19] is devoted to formulation the wave propagation in tall buildings assuming each floor as an individual layer analogous with the layers in a soil medium as shown in Figure 1.14. Once the reflection and transmission coefficient and the wave velocities are known, the wave travel time can be obtained for a given layer thickness (story heights) in every single layer. A schematic representation is introduced in Figure 1.14. Despite the simplicity of the method, it may be a better damage detection tool than the modal methods as the parameters are more sensitive to the changes in structural properties.

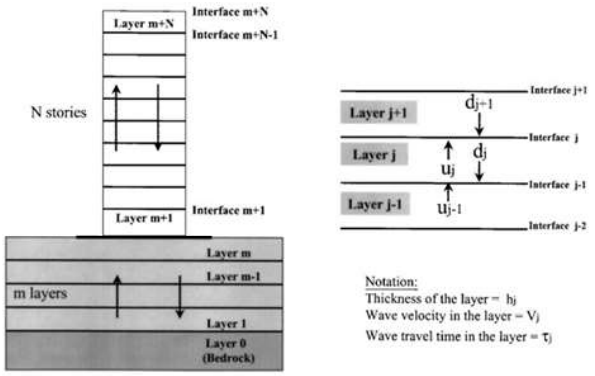

Figure 1.14. The bedrock, soil, and the building layers and the propagating waves [19].

Besides, this method is capable of taking the effect of soil layers into consideration and performs well at high frequencies. In order for the reader to visualize how seismic waves propagates along the height of a building, the seismic analysis results of a 15-story frame structure are shown through Figure 1.15-Figure 1.16. If one keeps track of the peak responses, it will be clear how the peaks shift towards right as the waves travel upwards.

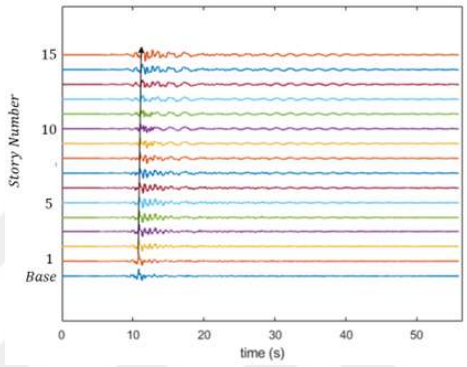

Figure 1.15. Acceleration response of a 15-story frame building subjected to seismic loading.

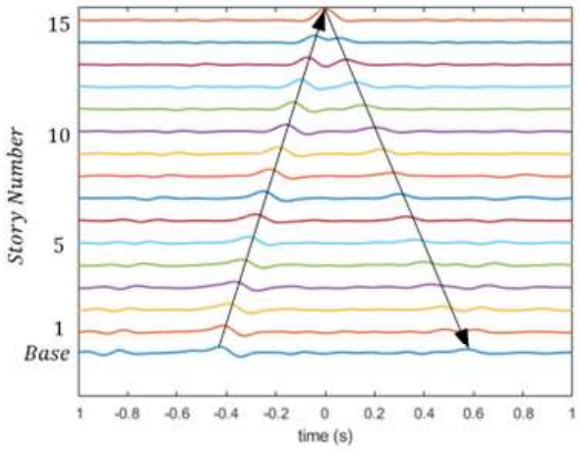

Figure 1.16. IRFs of a 15-story frame building subjected to seismic loading.

Based on Figure 1.14, the components of the seismic waves that propagates in the layered medium (be it the superstructure or the soil layer beneath) are the upgoing and

downgoing waves where $u\,(t)$ and $d(t)$ are the upgoing and downgoing wave amplitudes at the top and bottom of the corresponding layer, respectively. The upgoing wave can be considered as the superposition of the reflected component of the downgoing wave and transmitted component of the upgoing wave as per Eq. 1.16 where $R_{d,j-1}$ and $T_{u,j-1}$ are the reflection and transmission coefficients and τ_j is the one-way travel time

$$u_j(t) = R_{d,j-1}\ .\ d_j(t-\tau_j) + T_{u,j-1}.u_{j-1}(t-\tau_j). \tag{1.17}$$

The robustness of the deconvolution operation has also been demonstrated by the [20] by proving the uncoupling of the intrinsic attenuation and the radiation damping. Moreover, it has been proved that the deconvolution wave field is independent of the excitation and the shear wave reflection parameter at the base. Also, it is an important feature of the deconvolution that both the top and the base records, which are deemed the source signals, gives complementary information such as shear wave velocity and predominant mode of vibration.

Based on the [20], [21] have revealed that the deconvolution interferometry facilitates to estimate the fundamental mode of deconvolved waveforms and the velocities. The deconvolution interferometry is also a useful tool for distinguishing the building's "self" characteristics from that with the soil structure interaction. They also introduced the concept of "cut-off" building which is considered to rise from the reference receiver called as "virtual source". The signals recorded at various floors in the building are deconvolved with the virtual source and since the new cut-off building is independent of the whatever exists below this level (as if the structure is fixed at the virtual source), localization of damage is facilitated. Moreover, they revealed that the deconvolution of the time histories (of the motions) taken from several locations in a structure gives the impulse response of the system at any station. The modal quantities such as natural vibration frequencies of the modes, the mode shapes, and damping factors can be extracted from the deconvolution interferometry [22]. Used the fundamental vibration frequencies obtained from wave travel times (for 11 earthquake records) and developed a damage detection method for early warning systems.

As well as the earthquake excitations, it is desired to retrieve the impulse response functions under ambient vibration [23]. Examined the dynamic behavior of the historical Giotto's bell tower (located in Firenze) via the vibration-based methods (EFDD) and the seismic interferometry. They filtered the impulse response functions for 3 different frequency ranges, each of which contains two or more consecutive mode frequencies. They end up with the conclusion that the seismic wave velocity is frequency dependent and increases with increasing frequency ranges. Another finding is that the significant portion of the dispersion of the seismic wave is due to the bending whereas relatively small contribution comes from the soil structure interaction.

Todorovska and Trifunac worked on a real-life test bed. The structure is a 7-story reinforced concrete building located in Los Angeles area and has experienced 12 earthquakes. Two of these earthquakes inflicted structural damage while the building was still being monitored. These kind of real-life structures undergoing damage is precious in terms of researches in order to understand the real-life nature of a test subject other than that designed in the laboratory. Beside the earthquakes, several ambient vibration tests have also been conducted. The relationship between the structural damage and the changes in the IRFs as well as the frequencies were investigated. In order to eliminate possibly misleading (in terms of structural damage and stiffness changes in the structure) effects of the soil-structure interaction on the frequency changes, two type of frequencies have been defined: f_1 and f_{sys} which stand for the fixed based and structure + soil frequencies, respectively. The comparison between the system frequencies of undamaged and damaged structure after the San Fernando Earthquake revealed a 26% decrease in the first system frequency based on ambient vibration data in EW direction [25]. The f_1 measured for the earthquake records are smaller than f_{sys} measured for the ambient tests. The shear wave velocity, which is another indicator of the damage and stiffness loss, reported to drop by 50% between the base and the fourth floor during the San Fernando Earthquake. Another important conclusion that can be drawn was that the wave travel times and the IRFs are reported to be physically meaningful even for very short time windows. This was observed in another study [26] which focuses on the same matter in a similar method for a building heavily damaged

by 1979 Imperial Valley Earthquake. For the calculation of the fixed-base frequency of the structure (f_1), the layered shear beam model was embraced and the wave arrival times were retrieved from the IRFs obtained by deconvolution of the records. Consequently, the predominant fixed-based frequency is expressed as in Eq. 1.17 where τ_{tot} is the wave travel time from the ground to the top of the structure

$$f_1 = 1/\left(4\tau_{tot}\right). \tag{1.18}$$

As the change in the shear wave velocity corresponds to the change in the stiffness of the structure, the wave travel times and the deconvolution interferometry offer handy tools for detecting and localizing the damage. In this regard, the available studies [27-31] based on various methods such as adopting layered beam models such as Timoshenko beam, layered shear beams and non-uniform Timoshenko beam can be visited.

One of the main concerns as for this thesis is to investigate the usability of the seismic interferometry for the structures undergoing structural damage during an event and hence exhibiting nonlinear response. For such situations where the system is no longer a time-invariant system [32], developed a method which adopts deconvolution interferometry and the [33] and combine them for the case where both structural damage and soil-structure interaction exist. The proposed method was validated with the previous studies for a reinforced concrete building with an underlying soil type of soft clay. Among the time-frequency tools, the Stockwell time-frequency representation (also known as S-Transform) has been selected and adopted due to its advantages such as linearity, invertibility, and higher resolution and had been utilized by other researchers for the SHM purposes. For example [34], embraced Stockwell time-frequency representation for a reinforced concrete framed structure that experienced the 2009 L'Aquila Earthquake. The first step of the method proposed [32] is to extract the local spectra from the S-Transform which is followed by obtaining the instantaneous impulse response functions (IIRF) by deconvolving the local spectra. The method facilitates keeping track of the fixed-base natural frequency and shear wave velocity at any given time instant, and hence their change during an event. It should be noted that the

building was modeled as a shear beam and it was observed that the shear wave velocity between the basement and the 6th floor is different than that of the upper part due to the variations in story heights and concrete compressive strength for these two different layers. Therefore, the shear wave velocity was computed as the weighted average of the instantaneous time lag for the IIRFs. These changes were studies during various events before and after the seismic retrofitting of the structure. During the larger earthquakes, reductions in the shear wave velocity and fixed-based frequency matches with the instants where the amplitude of the ground shaking increases. For example, during the 1995 earthquake with a Moment magnitude of M_w=7.5, the shear wave velocity and the fixed-based frequency drop by 24% at the time instant in the vicinity of the occurrence of PGA. As a result, the proposed method is a useful tool for the determination of the damage-related parameters instantaneously during an event.

Within the context of this thesis, an important intermediate step for the proposed method is obtaining the interstory drift values of a real-life multistory building. This can be achieved by several methods and some of the most widely used ones can be listed as double integration of the acceleration data, direct measurement of the displacements via GPS, and digital image processing. However, each of these methods has certain drawbacks and limitations. Although the aim of this study is not to propose a method for the determination of interstory drifts, it is still an important point for the sake of integrity of the method. The first two options among the listed ones will be discussed herein. In the structural health monitoring if the measured quantity is accelerations, the data processing should be applied very carefully in order to obtain realistic displacement values after the double integration. Even small shifts in the acceleration record can lead quite significant errors in the displacements obtained through double integration. Therefore, the most important aspects of such data processing for earthquake induced response are baseline correction and filtering [35]. Conducted a study to identify the effect of the baseline correction on the displacements. The study used the famous Chi-Chi Earthquake which have numerous amount of available measurements from various sites. As a common application the pre-event mean of the record is subtracted from the entire record to ensure zero velocity values

at the end of the earthquake. For most of the cases, a useful control parameter to check the accuracy of the resulting displacements are the velocity traces at the end of the earthquake. Except the cases of significant afterslip, it is reasonable to expect the zero (or near-zero) velocity values at the end of the earthquake. However, this may not yield accurate values and many records have a linear velocity trace after removing the pre-event mean from the entire data. This suggests that there are different baseline offsets in the different parts of the data. Therefore, for the removal of the basline offsets, [35] embraced the approach by [36] where the earthquake records were split into two main segments implying two different baseline offsets to be removed. Based on the observation, the velocity and displacement traces have two different linear trends, and therefore, the different linear fitting is applied to the different segments and then subtracted individually. The significant parameters are the assumed zero velocity time at the beginning of the record (t_1) and the intermediate time (t_2) that separates the two baselines with different slopes [36]. Selected the t_1 value as the first time when the absolute acceleration is greater than 50 cm/s2 whereas [35] defined it as a free parameter which do not depend on a threshold or limit. For the latter parameter, [36] presents two alternatives which are: (a) t_2 is selected so that the absolute acceleration is never greater than 50 cm/s2 after t_2, (b) selection of t_2 yields the minimum final displacement [35]. However, defines t_2 which gives the zero line fit to velocity. Based on the comparison with the GPS measurements, it was reported for the available records that the horizontal components are more sensitive to the baseline correction than the vertical components and the [35] approach for the t_2 performs well. In terms of response spectra, the baseline correction generally has little or almost no influence for periods less than 20 seconds which encompasses the majority of the civil engineering structures. For a more detailed discussion of the effect of baseline correction on the response spectra [37], can be visited.

Skolnik and Wallace addresses a very common and important issue within the context of their studies. They presented the problems and possible measures regarding the interstory drifts obtained via double integration as well as alternative methods. They utilized data retrieved from the shake table tests and real-life buildings. As well as

the SHM purposes, the interstory drift are also used within the guidelines and codes [39-41] as it is directly correlated with structural and non-structural damage. Therefore, "accurate" determination of the interstory drifts not only facilitates detecting and localization of the damage, but also lets us even calculate the internal forces in the structural members which is one of the objectives of this thesis. Due to the noisy nature of the raw data, baseline correction (removal of the mean) and band-pass filtering are required to improve the signal quality. This is usually the first step of the processing the acceleration data. In order to remove the constant offsets, the pre-event mean is subtracted from the entire data and for the elimination of the high-frequency noise, low-pass filter is used. Although low-pass filter improves the quality, it should be kept in mind that the signal amplitude will decrease.

However, as suggested in the previous studies [35] removal of the pre-event mean (constant de-trending) is not the remedy to be used in every case. Several possible reasons for such baseline offsets can be listed as: (i) hysteresis in the instrument, (ii) misalignment of the sensors, (iii) the effect of analog to digital conversion [42], and (iv) tilting. In such cases where removal of the pre-event mean is not enough, the velocity trace is divided into several segments and polynomials are fit for each segments and the derivatives of these fits are subtracted from the acceleration data. Another effective tool is high-pass filtering for such baseline offsets. However, one must ensure avoiding phase lag (and consequently distortion of the signal) and be aware of the decrement in amplitude when carrying out high-pass filtering. This step requires experience and observation where the resulting displacements would be a plausible lead for the "best" corner frequency. Another issue in high-pass filter is the risk of long period losing data when the structure is exposed to inelastic (residual) displacement demands. Therefore, it is not possible to mention an "ideal" cut-off frequency. The nominal cut-off frequencies were investigated based on the relationship between the cut-off frequency and the signal to noise ratio (SNR) and it was concluded that the nominal cut-off frequency varies between 0.1-0.3 Hz for different sensors. The errors peak displacements obtained via double integration was found to be less than 5% and greater than 12% for the linear and nonlinear cases, respectively. As for alternative

methods, the contact methods are not practical for real-life buildings whereas non-contact methods (GPS and laser) found to be promising for both elastic and inelastic cases.

Lovse attempted to conduct deformation monitorin of a slender tower with an approximate height of 160 m. The GPS technology then allowed them to receive data with a sampling rate of 10 Hz and standard deviations of horizontal coordinates less than 5 mm. The FFT of the signal yielded a predominant frequency of 0.36 Hz with an amplitude of 16 mm. Çelebi and Sanli [44] deployed a permanent GPS deployment of a 34-story building with sensors having 10-20 Hz of sampling rate and 1-2 cm of horizontal and vertical accuracy, respectively. These values are acceptable for flexible structures with long periods and relatively high top displacements such as tall buildings and long-span bridges. For the study, 2 GPS sensors were deployed on the top of the building whereas 1 sensor (the reference station) was located on the top of a single-story structure consisting solely of shear walls, approximately 0.45 km away from the main structure. The building was also instrumented with the acceleration sensors and yet the displacements obtained via GPS and double integration could not be compared due to the low amplitude of motion which is below the error margin of the GPS (1 cm). However, their cross-spectra were compared and both of the acceleration and GPS data revealed a predominant frequency about 0.24-0.25 Hz. However, the current GPS technology is more advanced and can record displacements up to sampling rates of 50-100 Hz with an increased accuracy (10 mm and more depending on the baseline length) depending on the GPS type [45].

Briefly, the deconvolution interferometry can be summarized as follows. For a given excitation (e.g. earthquake), one of the floor responses is selected as the virtual source. Then by using the deconvolution seismic interferometry, the recorded response quantities in every floor are deconvolved with the reference station and the impulse responses to a virtual source are attained. From the IRFs, the propagation of the seismic waves can be observed clearly.

Deconvolution for different earthquake records gives the same impulse response function as long as the system responds linearly. The upgoing and downgoing waves can be seen apparently. Although deconvolution with respect to different virtual sources (e.g. the top or the ground floor) yields different impulse response functions, for a given excitation the floor responses are unique when the floor responses convolved with respect to the same reference point (which has been used in the deconvolution process). The advantages of the deconvolution based seismic interferometry is the ability to retrieve the impulse response function of the building without the soil structure interaction effects. Besides, the response of a building for a given excitation can be found as long as the building behaves in a linear fashion from the products of the deconvolution interferometry. This can be promising for obtaining responses of the sparsely instrumented floors under daily (operational) excitations with relatively small amplitudes, which facilitates estimation of the interstory drifts and the modal characteristics. Moreover, Safak [19] suggests that the wave propagation formulation provides better estimations for the identification of damping and the modal parameters are not sensitive local changes in the multi-story building's structural system. However, the parameters used in the wave propagation are sensitive to local damages and better represent the changes in the multi-story buildings' characteristics. Another point which deserves a remark is that the stiffness change or equivalently (but not necessarily) the damage in a specific story can be localized by the change in the shear wave velocity.

In addition to the needs and the gaps in this field as previously mentioned in the above section, the general problems in the structural health monitoring, as well as more specific ones, can be described as follows:

(i) Optimal and intelligent design of instrumentation phase. Due to economical and maintenance issues, currently it is not feasible to instrument every single floor of a tall building. Therefore, a wise way of instrumentation deployment with minimum number of sensors is needed. Establishing a model-driven sensor deployment strategy and its evaluation for a wide range of structure database might be a desirable solution. In addition, the story responses and mode shape

amplitudes of the non-instrumented floors should be determined accurately.

(ii) Determination of sensor types. In order to be able to extract the structural and dynamic characteristics of the buildings, various types of sensors are needed for different loading and couplings. A common question to be investigated today is which sensor or combination of sensors can perform best for a specified loading conditions, such as earthquake, typhoon, wind, temperature, traffic, or ambient excitations.

(iii) For a given building, the possibility of uniquely relating the number of instrumentations and the identifiable parameters can be investigated in order to formally standardize minimum number of sensors for the future codes and guidelines.

(iv) Specification of reliable damage indicators. The available literature suggests that the changes in the structural frequencies or damping ratios can be used as damage indicators. However, the extent of the damage should be quantified and the localization of the damage should be identified. Moreover, it is difficult to tell whether the changes in the structural frequencies are due to the cracking of non-structural members (e.g. infills) or due to the propagation of damage in structural members, or both. Besides, studies show that the parameters used in the vibration based methods (modal methods) are not sensitive to local or small damages. Therefore, seismic interferometry can be used for this purpose as well.

(v) Obtaining interstory drifts and identify the concomitant uncertainties. As mentioned earlier, the computation of displacements is a troublesome issue. The available methods such as double integration of accelerations, GPS measurements, diagonal wires constitute problems such as transformation of the baseline offsets into large displacement values, satellite-related inconveniences, and the wire slack, respectively. Solutions to the conventional measurement techniques may be brought or alternative novel techniques (laser dot/photodiodes or image processing) can further be implemented to the SHM and the uncertainties in the measurements can be quantified.

(vi) Establishing a quantitative relation between the elastic mode shape inelastic or mode shapes of a building. For example, the error percentage in the response estimations assuming the building behaves in elastic manner, albeit yielding, can

be specified.

(vii) To be more specific within the context of the thesis, a real time system identification-based assessment approach is needed for decision making on the operational or service circumstances of a tall building during or immediately after a severe event. At a given time, formation of damage at a certain region is investigated by the help of parameters retrieved by the system identification methods. Based on this probability, the overall condition of the building can be assessed.

2. VIBRATION-BASED SYSTEM IDENTIFICATION TECHNIQUES

Before applying the Method-1, the dynamic characteristics of the structures are identified via simple techniques proposed [46] and ARX models as a preliminary step. As an example, a 4-story shear frame with the following characteristics is evaluated under two different excitations; Gaussian White Noise, and the Chile earthquake. The actual dynamic characteristics of the shear frame are provided in the Table 2.1.

Table 2.1. Modal frequencies and damping ratios of the 4-story shear frame.

Mode Number	T_n (s)	f_n (Hz)	ω_n (rad/s)	ζ_n
1	0.600	1.666	10.467	0.0500
2	0.208	4.797	30.139	0.0226
3	0.136	7.349	46.175	0.0199
4	0.111	9.015	56.642	0.0200

Below are the mode shapes of the shear frame.

Table 2.2. Mode shape of the 4-story shear frame.

Story	**Mode-1**	**Mode-2**	**Mode-3**	**Mode-4**
4	1.000	1.000	1.000	1.000
3	0.879	-	-1.347	-2.532
2	0.653	-1.000	-0.532	2.879
1	0.347	-1.000	1.532	-1.879

In order to simulate the ambient vibration, a low amplitude, zero-mean Gaussian White Noise is imposed to the shear frame. The modal frequencies are then identified by utilizing the PSD (power spectral density) estimate via Welch's method. The excitation is divided in certain number of windows with a certain overlap percentage. The number

of windows and overlap percentage are selected as 10 and 50, respectively for this case.

Table 2.3. Identified frequency obtained via PSD under white noise excitation.

Mode	**Story-1**	**Story-2**	**Story-3**	**Story-4**
1	1.605	1.645	1.655	*1.66*
2	4.775	4.810	4.340	*4.79*
3	7.325	7.225	*7.330*	7.31
4	*9.025*	8.935	8.890	8.86

As can be from the Figure 2.1, the 1^{st} mode is much more visible in the 4^{th} story whereas the higher modes (3^{rd} and 4^{th} modes) are more distinctive in the first 2 stories. It is inferred that higher modes can be seen better in the lower stories while the first couple of modes can be identified better via the top stories. Because the first story has the maximum modal contribution in total when all the modes are considered. It has considerable contribution to almost all of the modes (even higher modes).

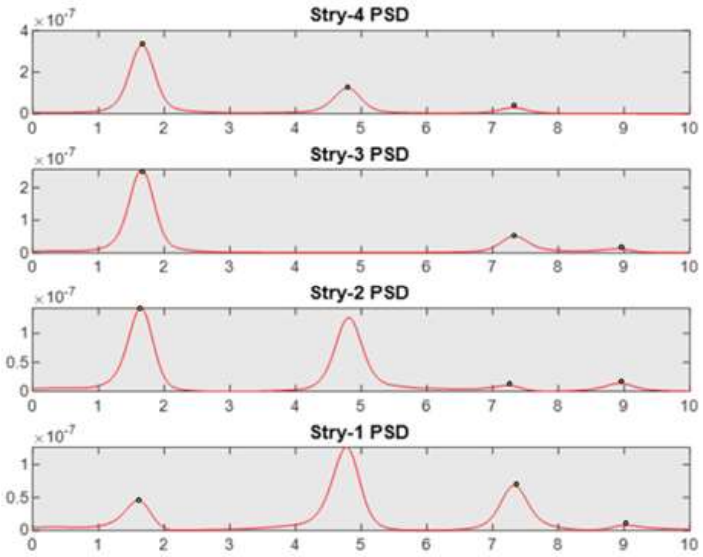

Figure 2.1. The PSD estimate under the white noise excitation.

The mode shapes can be identified via filtering the acceleration time series around each estimated modal frequency and (for each and every mode) dividing the obtained

modal floor accelerations to each other in order to get the mode shapes. However, there are two approaches herein. One can either divide (the modal acceleration values of one floor to another) point by point at every time step and take the average (Ph1), or can only divide the peaks and the valleys and take the average (Ph2). In this example, the mode shapes obtained via the peaks align reasonably well with the actual first three modes. However, the other approach yields better results for the 4th mode. It should be noted that, for this example, the peaks are never synchronized (at the peaks and valleys) for different floors. Another point deserves to be emphasized is that the sensitivity of the accuracy of the mode shapes depend on the bandwidth of the filter.

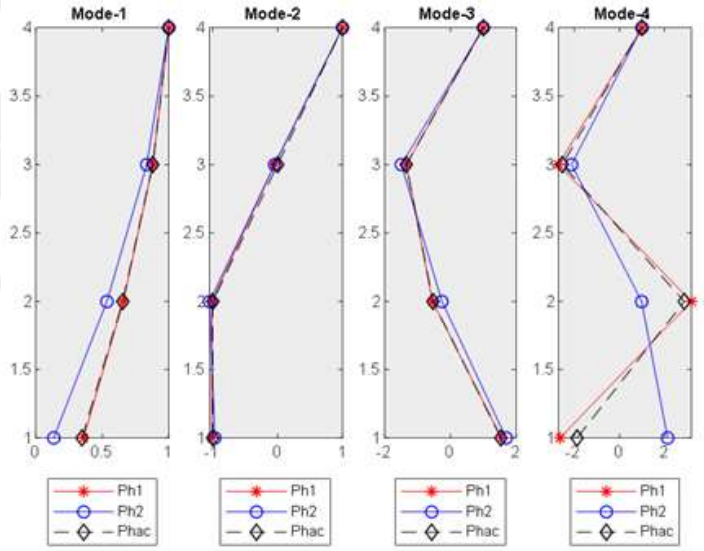

Figure 2.2. The estimated mode shapes obtained via 2 different approaches under the white noise excitation and the actual mode shape (bandwith of the bandpass Filter is 0.05 Hz).

The floor acceleration response histories are filtered (narrow band pass filter) around the identified modal frequencies and the bandwidth of the filter significantly affects the accuracy of the mode shapes. The identified mode shapes with the two aforementioned approaches and various filter bandwidth values are illustrated in Figure 2.2 and Figure 2.3.

While estimating the modal damping ratios, the acceleration time histories for different floors are first narrow filtered around the identified modal frequencies and then the Half-Power Bandwidth approach is applied to their power spectra. It is vital to note that the results are sensitive to the bandwidth of the filter, window length, and the overlap percent of the power spectra. The results presented above are attained by taking the bandwidth as 25% of the corresponding modal frequency, dividing the data into approximately 30 windows with 50% overlap.

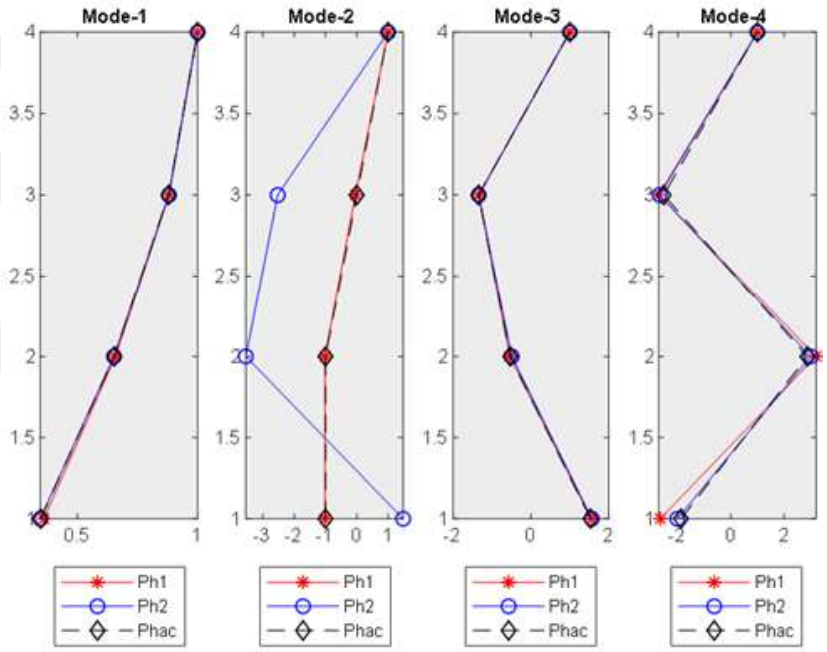

Figure 2.3. The estimated mode shapes obtained via 2 different approaches under the white noise excitation and the actual mode shape (bandwith of the bandpass filter is 0.015 Hz).

The comparison of the damping estimations and the actual damping ratios are as in the Table 2.4.

Table 2.4. Estimated modal damping ratios for each story based on the half-power bandwidth approach under the white noise excitation.

Mode	**Identified Modal Damping Ratios (%)**				**Actual Modal Damping Ratios (%)**
	Story-1	**Story-2**	**Story-3**	**Story-4**	
1	5.06	5.39	5.49	5.52	5.00
2	2.17	2.22	4.22	2.22	2.26
3	1.78	1.57	1.78	1.82	1.99
4	0.87	1.26	2.00	2.64	2.00

The damping estimation can also be performed by the autocorrelation function (logarithmic decrement method) where the decay of the amplitude of the ACF, $R(\tau)$ is kept tracked. The acceleration records are first filtered around the modal frequency and then the $R(\tau)$ is computed for each mode. From the equations below, the damping ratio is calculated utilizing a polynomial fit to the first degree (straight line) to the peaks of the natural logarithm of the autocorrelation function

$$R(\tau) = C.e^{(-\zeta\omega_n\tau)} \quad \Rightarrow \quad \ln R(\tau) = -\zeta\omega_n\tau + \ln C. \tag{2.1}$$

In the Eq 2.1, $R(\tau)$ is the autocorrelation function corresponding to the time lag τ, ω_n is the natural vibration frequency of the mode of interest, and C is a constant.

After several trial-error sequences, the optimal bandwidth of the filter is decided to be 25% of the corresponding modal frequency of interest. Once the records are filtered accordingly, their $R(\tau)$ is computed with a large number of lags (say 40% of the given record length). The period of the peaks of the $R(\tau)$ must be equal to the natural vibration period of the mode of interest. Then the natural logarithm of the $R(\tau)$ is taken for which the results are in imaginary plane and the period of the peaks are equal to the half of the natural vibration period of the mode of interest. Here, only the real parts of the $\ln R(\tau)$ are taken into consideration as long as the periods of the peaks are within 10% error limit regarding the $0.5T_n$. Finally, a straight line is fitted

to the aforementioned peaks. The axes of the peaks are the lags in seconds ($\zeta * \Delta t$) and the real parts of the $\ln R(\tau)$. Alternatively, it could be computed via fitting an exponential curve to the ($\zeta * \Delta t$) and the $R(\tau)$ itself. The results are tabulated below.

Table 2.5. Estimated modal damping ratios for each story based on the logarithmic decrement method under the white noise excitation.

Mode	**Identified Modal Damping Ratios (%)**				**Actual Modal Damping Ratios (%)**
	Story-1	**Story-2**	**Story-3**	**Story-4**	
1	4.87	4.97	5.07	5.09	5.00
2	0.44	2.47	9.75	0.45	2.26
3	0.20	1.57	0.21	0.20	1.99
4	0.58	0.12	1.44	2.19	2.00

As the last method to be discussed herein for damping estimation in the ARX model where the most vital issue is to determine the model orders. As the model orders are increased, the quality of the fit and estimation gets better. However, the trade-off herein is the increased model orders lead artificial modal frequencies and other characteristics since the noise in the system is also modelled. However, as the modal frequencies are estimated beforehand by the Welch's Spectrum, the damping values corresponding to the pre-known modal frequencies are the real modal damping values. Based on the facts above, large system order is assigned to the ARX model and then the irrelevant frequencies are omitted from the calculations. The damping estimations obtained by utilizing the ARX model with model orders of 120 can be found in Table 2.6.

Table 2.6. Estimated modal damping ratios for each story based on the ARX model under the white noise excitation.

Mode	**Identified Modal Damping Ratios (%)**				**Actual Modal Damping Ratios (%)**
	Story-1	**Story-2**	**Story-3**	**Story-4**	
1	5.00	5.00	5.00	5.00	5.00
2	2.25	2.25	-	2.25	2.26
3	1.98	1.98	1.98	1.98	1.99
4	1.97	1.97	1.97	1.98	2.00

Story displacements are obtained by double integrating the story accelerations filtered around the modal frequencies. Again, the success of the estimated modal and total story displacements are sensitive to the bandwidth of the filter. It is desired to evaluate the best filter bandwidth as the certain fraction of the modal frequency of interest via the mean squared error of the floor displacement time histories. The results can be seen in the Table 2.7.

Table 2.7. The best filter bandwidth values for the estimation of the modal displacements under the white noise excitation (j is the mode number).

	Story-1	**Story-2**	**Story-3**	**Story-4**	**% Modal Mass Participation**
Mode-1	$0.38f_1$	$0.54\ f_1$	$0.60\ f_1$	$0.44f_1$	89.3
Mode-2	$0.54f_2$	$0.87f_2$	-	$0.73f_2$	8.3
Mode-3	$0.52f_3$	$0.14f_3$	$0.83f_3$	$0.38f_3$	2.0
Mode-4	$0.17f_4$	$0.38f_4$	$0.25f_4$	$0.21f_4$	0.4
$\sum_{\mathrm{j}}^{\mathrm{n}} \mathrm{D_j}$	$0.35f_j$	$0.57f_j$	$0.59f_j$	$0.63f_j$	100.0

All of the above identification analyses are also performed under the Chile earthquake. However, for the sake of brevity, the modal damping ratios are not depicted. For the frequency identification of the structure under Chile earthquake, the following

values are used. The data is divided into an approximate number of 45 segments and the overlap is 50%.

The modal frequency, mode shape, and displacement estimations of the shear frame subjected to Chile earthquake are shown below.

Table 2.8. Identified frequency obtained via PSD under white Chile excitation.

Mode	**Story-1**	**Story-2**	**Story-3**	**Story-4**
1	1.630	*1.680*	1.700	1.710
2	4.715	*4.830*	5.060	4.765
3	*7.285*	7.020	7.230	7.190
4	*9.080*	8.925	8.655	8.710

The PSD estimate plot of the Table 2.8 can be visually inspected in Figure 2.4 where the peaks are not as distinct as the case for the white noise due to the frequency content of the earthquake.

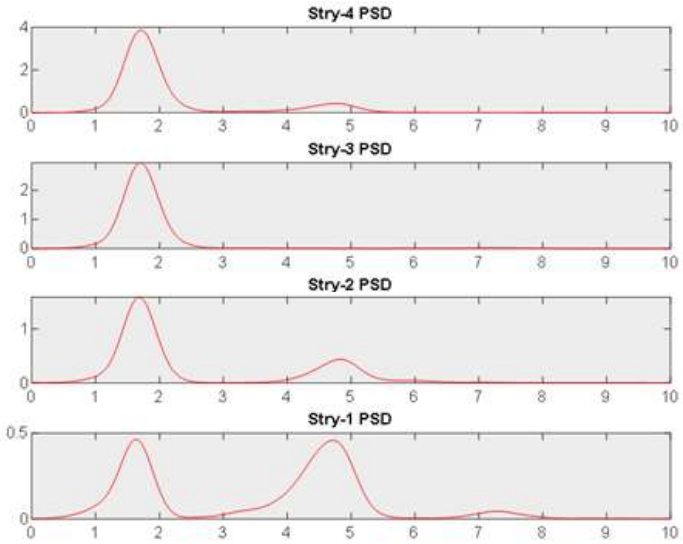

Figure 2.4. The PSD estimate for the Chile earthquake.

As explained previously, the mode shapes can be identified via filtering the acceleration time series around each estimated modal frequency and (for each and every

mode) dividing the obtained modal floor accelerations to each other in order to get the mode shapes. However, for the Chile earthquake case, the mode shape estimations with the second method (Ph2) are seem to perform poorly when compared to Ph1 when the filter width is chosen to be 0.015 Hz.

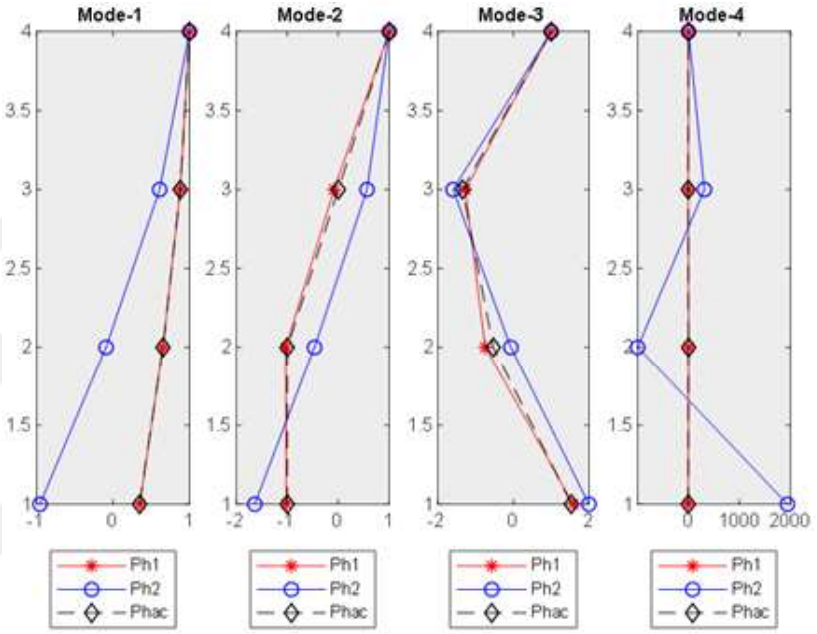

Figure 2.5. The estimated mode shapes under the Chile earthquake obtained via 2 different approaches and the actual mode shape (bandwith of the bandpass Filter is 0.015 Hz).

However, for a filter bandwidth of 0.1 Hz, the Ph2 also performs satisfactorily, even better for the higher modes.

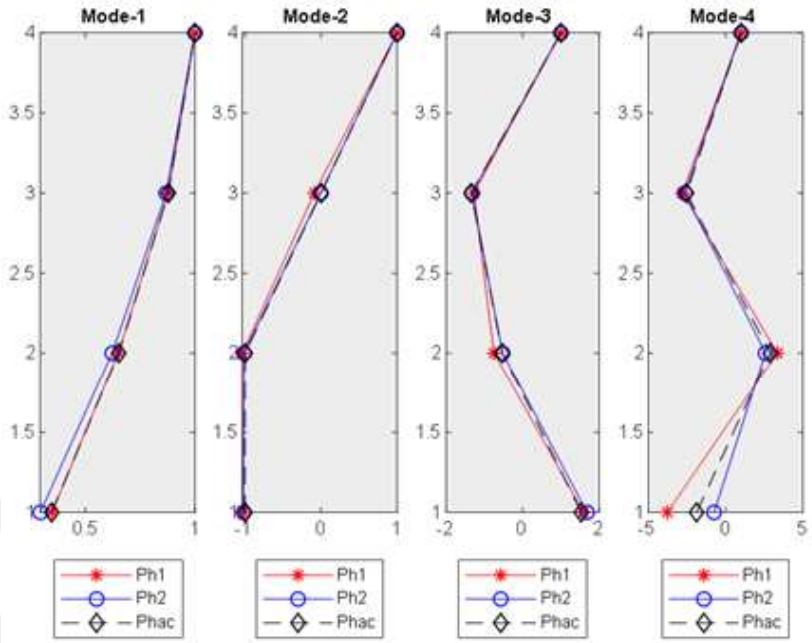

Figure 2.6. The estimated mode shapes under the Chile earthquake obtained via 2 different approaches and the actual mode shape (bandwith of the bandpass Filter is 0.1 Hz).

Story displacements are obtained by double integrating the story accelerations filtered around the modal frequencies. Again, the success of the estimated modal and total story displacements are highly sensitive to the bandwidth of the filter.

Table 2.9. The best filter bandwidth values for the estimation of the total displacements based on the MSE approach under Chile earthquake (j is the mode number).

	Story-1	**Story-2**	**Story-3**	**Story-4**
$\sum_{\mathrm{j}}^{\mathrm{n}} \mathrm{D_j}$	$0.40 f_j$	$0.55 f_j$	$0.80 f_j$	$0.80 f_j$

3. PROPOSED METHODOLOGIES

3.1. Proposed Method-1

Identification and the response of a structure with sparse instrumentation has been a significant topic as discussed earlier. Such studies do not focus only on building type structures [5]. Developed a virtual sensing method in order for wind turbines which utilizes similar tools for estimating the response quantities. The method which was previously discussed in the literature review part and one of the proposed methods (Method-1) are compared herein. Both methods focus on estimating the mode shape amplitudes of non-instrumented (sparsely instrumented) floors are compared herein. The previous one is based on the assumption of shear and bending beams. Note that the notations will slightly be changed in order to make it easier to follow the derivation of both methods, and to make sure the notation is consistent. The building is considered as a linear combination of a bending and a shear beam. Since, the method is based on the mode shapes of a shear and a bending beam, hereinafter referred to as MSBE (mode shape based estimation) method. For an MDOF building, the total physical response of nth floor can be obtained by the superposition of j modes as described in the Eq. 3.1, where $u_{nj}(t)$ is the physical displacement response of the nth floor, ϕ_{nj} is the jth mode shape of the nth floor, and the $D_j(t)$ is the response in modal coordinates

$$u_n(t) = \sum_j \phi_{nj} D_j(t). \tag{3.1}$$

The mode shape is assumed as linear combination of a shear and a bending beam as follows:

$$\phi_{nj} = C_{j,s} \cdot \phi_{nj,s} + C_{j,b} \cdot \phi_{nj,b}, \tag{3.2}$$

$$\varepsilon_j(t) = \sum_{n=1}^{NIF} \left[y_{nj}(t) - u_{nj}(t) \right]^2. \tag{3.3}$$

In the Eq 3.2, $C_{j,s}$ and the $C_{j,b}$ are the weighting factors of the shear and the bending beam, respectively. The error function can be expressed as sum of the square

of the errors of the modal response quantities over the instrumented floors as can be seen in the Eq. 3.3, where *NIF* is the number of instrumented floors.

In order to minimize the error, the partial derivative of the error function with respect to the weighting coefficients result in the following:

$$\begin{bmatrix} \sum_{n=1}^{NIF} \phi_{nj,s}^2 & \sum_{n=1}^{NIF} \phi_{nj,s} * \phi_{nj,b} \\ \sum_{n=1}^{NIF} \phi_{nj,s} * \phi_{nj,b} & \sum_{n=1}^{NIF} \phi_{nj,b}^2 \end{bmatrix} \begin{Bmatrix} C_{j,s} * D_j(t) \\ C_{j,b} * D_j(t) \end{Bmatrix} = \begin{Bmatrix} \sum_{n=1}^{NIF} \phi_{nj,s} * y_{nj}(t) \\ \sum_{n=1}^{NIF} \phi_{nj,b} * y_{nj}(t) \end{Bmatrix}. \tag{3.4}$$

Thus, the weighting coefficients multiplied by the modal coordinates can be calculated by taking the inverse of the left-hand side of the matrix once pre-multiply by the right-hand side of the equality.

The latter one (Method-1) is derived within the context of this thesis and can be deemed model driven. It is aimed to find the mode shape amplitudes (and physical response quantities) at the non-instrumented floors by assuming the actual mode shapes of a building can be approximated as linear combination of the mode shapes calculated from the mathematical (or computer) model of the real-life building. Let's denote the model mode shapes as $\hat{\phi}$ and the actual or measured mode shapes as ϕ. The estimated mode shapes are calculated as per Eq. 3.5 or Eq. 3.6 (in matrix form)

$$\phi_{nj} = \sum_{k=m} \hat{\phi}_{nk} * C_{kj}, \tag{3.5}$$

$$[\mathbf{\Phi}]_{n \times j} = \left[\hat{\mathbf{\Phi}}\right]_{n \times k} [C]_{k \times j}. \tag{3.6}$$

In the Eq 3.6, m is the vector which includes the desired model modes (mode shapes of the numerical model) to be superimposed. For example, $m = \{2,\ 3,\ 5,\ 8\}$ if the 2^{nd}, 3^{rd}, 5^{th}, and 8^{th} mode shapes of the numerical model which are desired to be superimposed in order to approximate the "real" mode shape of the structure under consideration. In order to find a suitable weighting coefficient for each model mode, the error minimization approach is used by taking the difference between measured and simulated (response of the numerical model) responses in modal coordinates as

reference. Establishing the error function and taking the partial derivatives for the weighting coefficients C yields:

$$\begin{bmatrix} \sum_{NIF} \hat{\phi}_{n1}\hat{\phi}_{n1} & \cdots & \sum_{NIF} \hat{\phi}_{n1}\hat{\phi}_{nm} \\ \vdots & \ddots & \vdots \\ \sum_{NIF} \hat{\phi}_{nm}\hat{\phi}_{n1} & \cdots & \sum_{NIF} \hat{\phi}_{nm}\hat{\phi}_{nm} \end{bmatrix}_{m\times m} \begin{Bmatrix} C_{1j}D_j(t) \\ \vdots \\ C_{mj}D_j(t) \end{Bmatrix}_{m\times 1} = \begin{Bmatrix} \sum_{NIF} y_{nj}(t)\hat{\phi}_{n1} \\ \vdots \\ \sum_{NIF} y_{nj}(t)\hat{\phi}_{nm} \end{Bmatrix}_{m\times 1}. \quad (3.7)$$

In the Eq 3.7, the left hand side matrix will be called as the H matrix hereinafter. Once the weighting coefficients for the superimposed model mode shapes are obtained, the total responses can be computed by Eq. 3.5, Eq. 3.7 and Eq. 3.8

$$u_{nj}(t) = \phi_{nj} * D_j(t) = D_j(t) \sum_{k=m} \hat{\phi}_{nk} * C_{kj} \quad (3.8)$$

$$u_n(t) = \sum_j u_{nj}(t). \quad (3.9)$$

Note that, in order to have an invertible (non-singular) matrix H, the number of superposed model modes must be less than or equal to the number of instrumented floors, $m \leq NIF$.

3.2. Proposed Method-2

The Method-2 aims to monitor and assess the structures with least possible number of sensors. Two sensors (one at the top and another at the base of the structure) are kept permanently. The other sensors (temporary ones) are moved among the stories so that the IRF of each and every story can be obtained for once. This is called the scanning phase. After the scanning phase, the IRFs are convolved with the top and/or base real-time acceleration records and the response of the non-instrumented stories are predicted at any given time. A significant point that deserves to be emphasized is whether the convolution process can be used if the response migrates to nonlinear region. If yes, what are the limits and extent of such an application? The answer for

this question is investigated further in the following sections.

Following the convolution process, the story response quantities are estimated. Once the story displacements are estimated via appropriate processing of the acceleration data or GPS measurements, the internal forces and deformations in structural members are computed via nonlinear fiber models and joint operations. Two various programs were coded to extract force & deformations in the members. The first one is for the columns & beams and the second for the structural walls.

The first program called the "Inelastic Reverse Drift" relates the interstory drift with the nonlinear flexural deformations by adopting fiber model. The structural member is divided into desired number of fibers and the contribution of each fiber to the lateral deflection is integrated along the height of the member. There are no limits on fiber size or fiber numbers both in terms of height and cross-section. The user is free to define as much fiber as desired as well as number of reinforcing bar layers. In a design/assessment process or collapse analysis, plasticity models might be more time-effective. However, since the aim herein is to capture the behavior and response under very low-high displacement and force demands, complete fiber model is preferred. A representative fiber element is shown in Figure 3.1. The interstory drift values obtained by double integration of the accelerations or direct measurements via GPS, are implemented in an iterative algorithm in an effort to compute the approximate internal forces.

The algorithm operates as a "reverse" nonlinear structural analysis software. The internal forces are calculated for a given chord rotation or tip displacement or the relative displacement at any given point. In this case, the input parameter for the displacement is the interstory drift. However, the contribution of the joint rotations should be eliminated from the previously obtained interstory drifts as can be seen in the Figure 3.2 since the deflection of the columns calculated as per Figure 3.1 are due to "pure" flexure. Therefore, the interstory drift values should be tailored to ensure the relative displacements of the column ends are due to only flexural deformations.

This entire relationship can be expressed as per Eq. 3.10. Once the effect of the joint rotations is eliminated, the internal forces at member ends are estimated via the joint equilibrium by adopting the Point of Inflection (PI) assumption which is depicted in Figure 3.3.

$$\int_0^H \varphi(y)\, y dy = (\Delta_j - \Delta_i)_{measured} - H\theta_i. \tag{3.10}$$

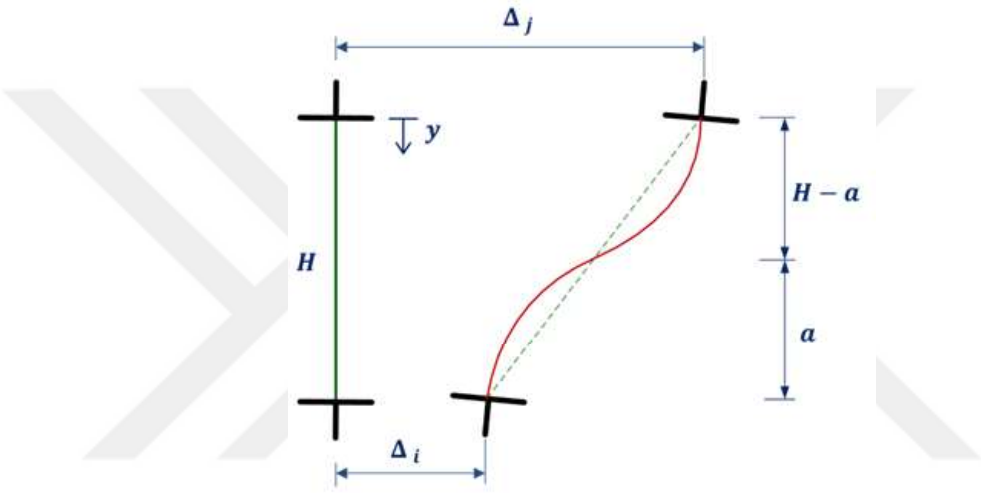

Figure 3.1. The nonlinear flexural fiber model used in both programs in order to find the displacements of members at any given point.

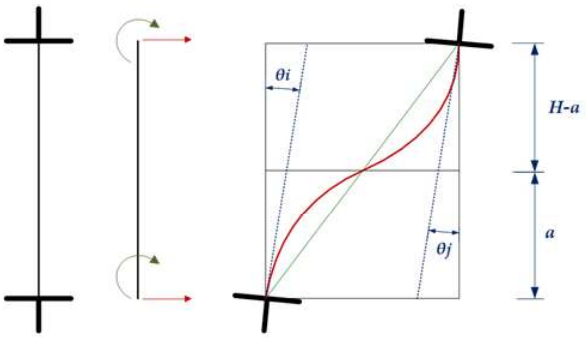

Figure 3.2. Contribution of the joint rotations to the interstory drift.

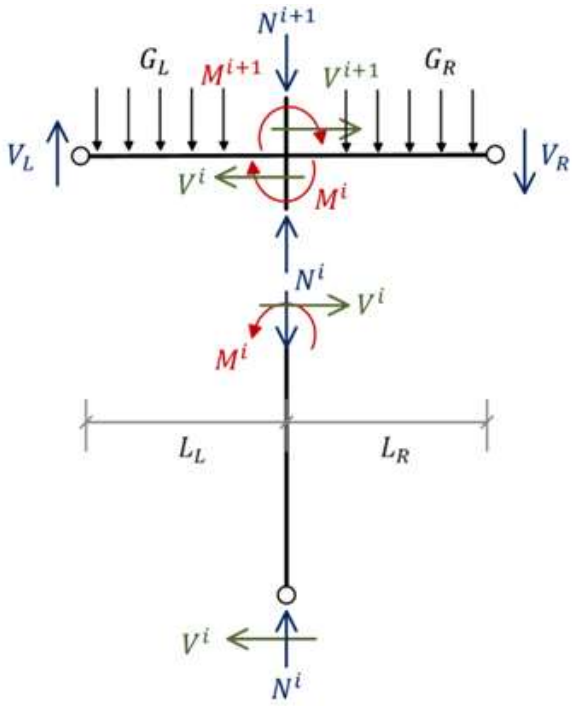

Figure 3.3. Joint equilibrium for a beam-column joint.

3.2.1. Determination of the Point of Inflection and Joint Rotationsn

The reverse inelastic structural analysis of statically indeterminate systems requires certain simplifications and assumptions. For this study, proper estimation of joint rotations and location of the zero moment points are vital.

The PI for the beams are taken as 1/2 of the member length whereas for the column members, more refined analyses need to be conducted as the joint rotations and corresponding internal forces are sensitive to this parameter. In order to refine the estimation of the location of the PI, a 3-bay - 3-story 2D frame system is analyzed for 3136 scenarios. The variable in the scenarios is the column/beam stiffness ratio. The frame system has assumed to have rigid diaphragm and the lateral forces are acted through the center of the diaphragm.

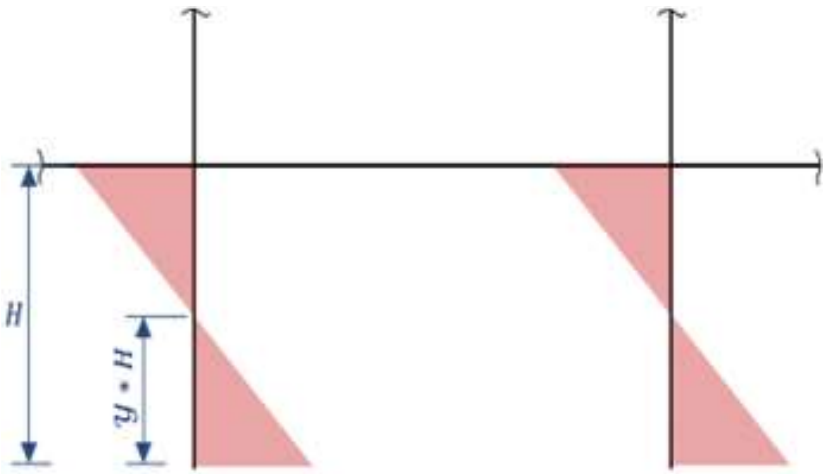

Figure 3.4. Location of the point of inflection of column as a fraction of height.

From the aforementioned 3136 structural analyses, an expression for the location of the point of contra-flexure (for columns) is obtained via curve fitting as demonstrated in Figure 3.4. A simple expression as an indicator of relative column/beam stiffness is derived as shown in the figure below. The relative column/beam stiffness are defined with the α coefficient as in the Eq. 3.10. However, both linear and nonlinear structural analyses results show that it is not possible to approximate the location of the PI no matter the number of analyzed buildings and scenarios. Especially under dynamic loading, it is almost impossible to capture the location of the column PI as there are several parameters that affects the PI location such as joint rotations at both ends (which is directly related to the lateral displacement profile of the structure)

$$\alpha = \frac{(h_{col}/H)}{(h_{beam}/L)}. \tag{3.11}$$

For this reason, a robust approach for the PI location is needed for the internal force estimation as it affects the entire reverse structural analysis procedure to a considerable extent and is not a parameter to be sacrificed for the sake of simplicity. Therefore, a computer model of the structure is established for only modal analysis. At a given time, the known displacement profile of the structure is approximated via several mode shapes of the computer model and consequently the joint rotations are approximated. Although this may seem to be a somewhat difficult process, the only

analysis to be performed on the computer model is the modal analysis. It is desirable for the computer model to be a calibrated model as proposed in the Method 1, but necessarily. Any error minimization algorithm can be used to approximate the lateral displacement profile of the structure as a linear combination of the numerical mode shapes. The coefficients obtained for each mode shapes are also used for the joint rotations of the column ends as shown in the Eq. 3.12 and Eq. 3.13

$$\Delta_N = \sum_j \hat{\Delta}_{Nj} C_{Nj}, \tag{3.12}$$

$$\theta_N = \sum_j \hat{\theta}_{Nj} C_{Nj}. \tag{3.13}$$

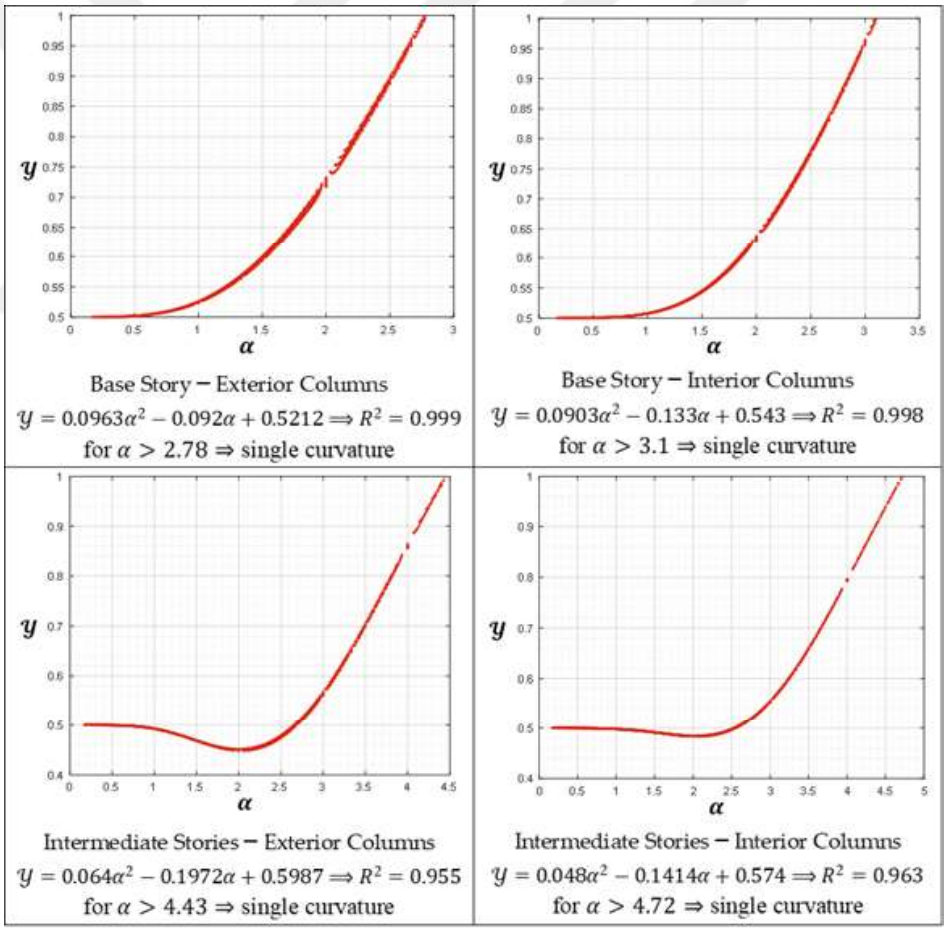

Figure 3.5. The relation between the PI and the α established from curve fitting of 3136 analyses.

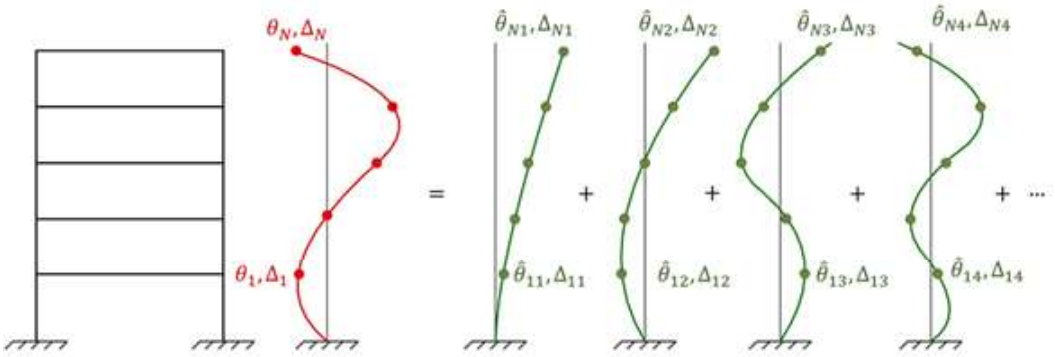

Figure 3.6. The approximation for the joint rotations at any given displacement profile.

In the Eq 3.12 - Eq 3.13, Δ_N and $\hat{\Delta}_{Nj}$ are the lateral displacements of the column end located at the floor N (at any given time t under an excitation) for the real-life building and mode j of the numerical model, respectively. Similarly, θ_N and $\hat{\theta}_{Nj}$ are the joint rotations of the column ends located at the floor N (at any given time t under an excitation) for the real-life building and mode j of the numerical model, respectively. The C_{Nj} is the coefficient for each mode. It should be noted that these approximation is carried out for each vertical axis so that the joint rotations for each column can be estimated individually.

Another approximation for the estimation of the joint rotations does not require any numerical model. The joint rotations are approximated via taking the numerical derivative of the displacement profile of the real-life structure by using [47, 48]. However, the drawback of this approximation is to assume that all of the joint rotations at the column ends are equal for each floor level, and yet, the results are still satisfactory.

Determination of the joint rotations at column ends properly is a considerably difficult task unless there is a well-correlated available computer model of the structure. Within the context of this method, the point of contra-flexure assumption is also based on the joint rotations and expressed in the Eq. 3.14. In order to have bare minimum variables and uncertainties and one global assumption for the method, the estimation

of the PI also depend on the joint rotations where $\Delta_i, \Delta_j, \theta_i, \theta_j$, a, and H are the displacement at joint i, displacement at joint j, rotation at joint i, displacement at joint j, the distance between the i end and the PI, and story height, respectively. All of the parameters are known in the equation below except the θ_i and θ_j. Assuming the rotation at the top and bottom nodes of any columns can be approximated as the above methods, the Eq. 3.14 facilitates estimating a PI for each column

$$\frac{a}{H} = \frac{(\delta_j - \delta_i)/H - (2\theta_i + \theta_j)/3}{2(\delta_j - \delta_i)/H - \theta_i - \theta_j}. \tag{3.14}$$

The reverse structural analysis starts from the uppermost top corner of the building and proceed very similar to the approximate structural analysis methods as in the Figure 3.7 with minor differences. In Figure 3.8, the method is tried to be summarized in a clear way.

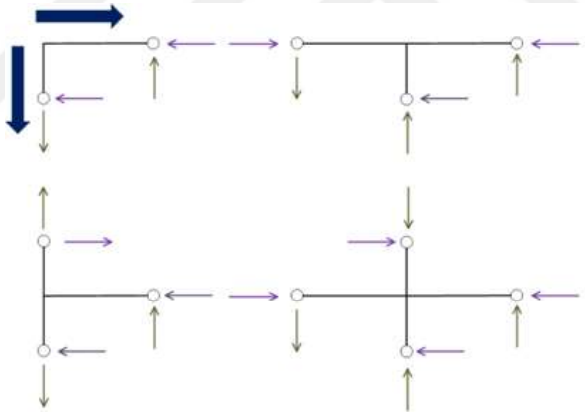

Figure 3.7. The reverse structural analysis where the solid blue lines show the direction of the analysis.

INELASTIC REVERSE DRIFT ALGORITHM for FRAMED STRUCTURES

1. Estimate the interstory drifts via convolution and proper processing for non-instrumented floors

2. Estimate the joint rotations at the column ends by one of the suggested approximations; i.e. either by using a numerical model or taking the derivative of the lateral displacement profile of the building at any given time t.

3. Subtract the contribution of the joint rotations from the "raw" interstory drift values obtained in Step 1.

4. Estimate the point of inflection for each column as per Equation 3.12.

5. Estimate the gravity loads on the beam and point of inflections for the beams (for example, can be taken as 0.5L or 0.3L)

6. From starting top-right (or top-left) corner of the structure (where there is only one beam and column at the node of interest) establish the equilibrium equations and solve for the unknowns. **There are 3 equations and 3 unknowns! Find the unknowns by solving 3 nested iterations.** (visit Figure 3.1-3.3)

$$\sum M = 0 \Rightarrow \quad M^i + M^{i+1} + V_L L_L + V_R L_R - \frac{G_L L_L^2}{2} + \frac{G_R L_R^2}{2} = 0$$

$$\sum N = 0 \Rightarrow \quad N^i - N^{i+1} - V_L + V_R - G_L L_L - G_R L_R = 0$$

$$\underbrace{M^i}_{UNKNOWN} = -\underbrace{M^{i+1}}_{known} - \underbrace{V_L}_{UNKNOWN} L_L - \underbrace{V_R L_R}_{known} + \underbrace{\frac{G_L L_L^2}{2}}_{known} - \underbrace{\frac{G_R L_R^2}{2}}_{known}$$

$$\underbrace{N^i}_{UNKNOWN} = -\underbrace{N^{i+1}}_{known} - \underbrace{V_L}_{UNKNOWN} - \underbrace{V_R}_{known}$$

$$\int_0^H \varphi(y) y \, dy = \underbrace{\underbrace{(\Delta_j - \Delta_i)_{measured}}_{known} - \underbrace{H\theta_i}_{known}}$$ ⇒ Iterate the curvature values at each vertical fiber (slice)

and corresponding moment value based on the PI assumption (which imposes a certain moment profile),

and finally obtain the column end moments M^i and M^j.

7. Proceed to the left (or right) and downwards to find the internal forces of the member in the fashion described in Step 5.

Figure 3.8. The Inelastic Reverse Drift algorithm developed for the framed structures.

The inputs of the program (Inelastic Reverse Drift) are the interstory drift values (obtained via convolution), cross-sectional properties, reinforcement detailing, confinement parameters, number of longitudinal and cross-sectional fibers, height of the column, and other parameters for the iteration control. The outputs are the internal forces and deflections for column members in the structural system.

Another program is coded for the structural walls which operates in a very similar manner with some minor differences. Instead of joint equilibrium, the wall is considered to be a single element and the variation of response quantities can be chosen as follows. There are 3 options for the axial force and moment profile along the height; parabolic, linear, and constant with an option of the location of the PI for the moment distribution along the height of the wall (Figure 3.9).

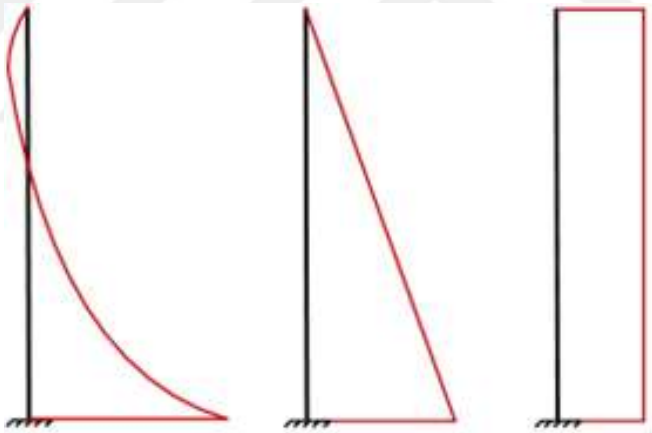

Figure 3.9. Axial load and moment profile options for the program which is coded for the structural walls.

Besides, in case the upper part of the wall might remain uncracked (which is quite likely under low-amplitude excitations of the tall structural walls), the tension strength of concrete is (optionally) taken into account in an effort to properly estimate the internal forces and capture yielding at the base of the wall. For the tension strength of concrete [49], model is embraced. The stress-strain curve and model details can be investigated in Figure 3.8, where ε_r tensile concrete strain, is ε_{cr} cracking strain of

concrete (average), f_{cr} tensile strength of concrete (MPa), f'_c concrete compressive strength (MPa), σ_r concrete tensile stress (MPa), E_c modulus of elasticity of concrete (MPa).

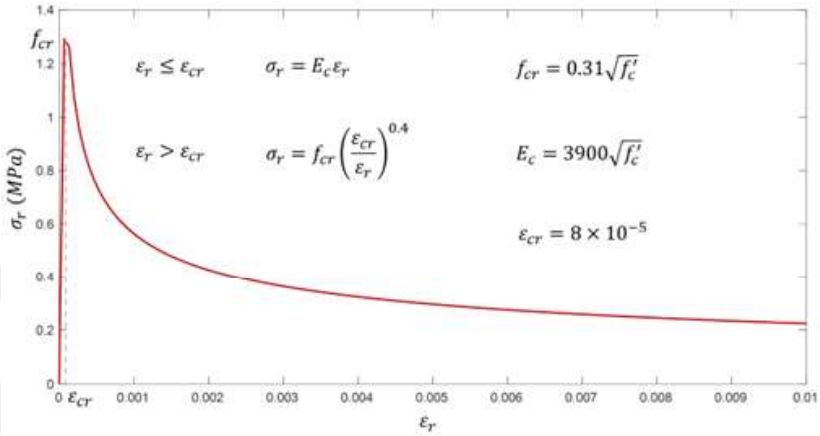

Figure 3.10. Belarbi and Hsu model for concrete in tension.

A lightly reinforced structural wall is examined and demonstrated in Figure 3.10 in order to show the significance of the tensile strength of concrete in prediction of the wall top drift. The displacement profiles of the structural wall at the onset of yielding of the base are illustrated below. For a 45 m long slender wall, the difference is around 20% at the top which is expected to increase as increasing wall height (Figure 3.11). Therefore, especially for low-to-moderate amplitude motions, the effect of concrete tensile strength is tall building walls might be a prominent parameter for the response estimation and damage detection.

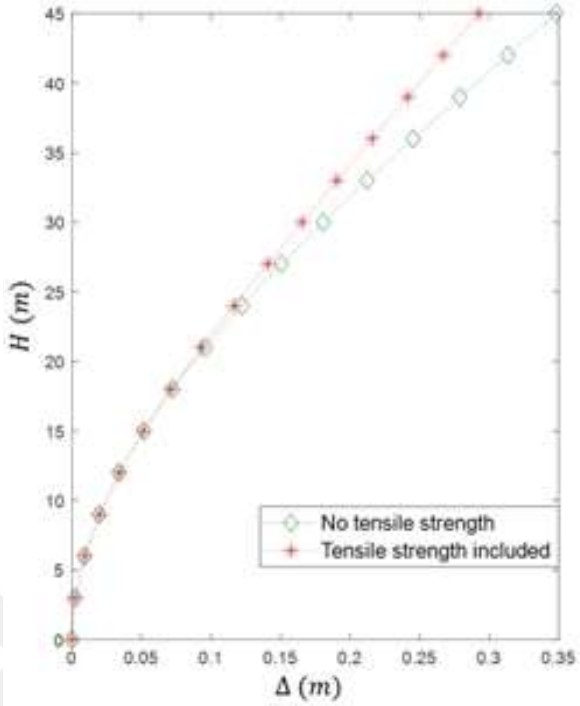

Figure 3.11. Lateral displacement profile of the structural wall with and without concrete tensile strength.

To sum up, the inputs for the program coded for the reinforced concrete structural walls are; the material properties, cross sectional dimensions, reinforcement and detailing, confinement parameters, wall height, the variation of axial load and bending moment along the wall height, top displacement of the wall, number of cross-sectional and longitudinal fibers, number of output stations for displacement, and error parameters for the iterations. The outputs are the internal forces and deflections at any given height or the wall "mode shape" for the given displacement values. Also, it is possible to define the wall web regions and boundary regions separately with no limits on the longitudinal reinforcement and number of fibers along the height and within the cross section.

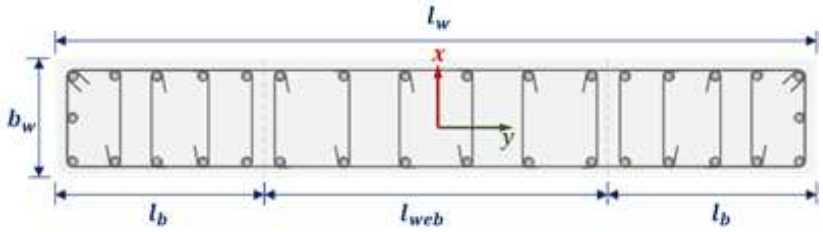

Figure 3.12. Wall web and boundary regions and a generic wall configuration for the program.

It should be noted that shear deformations, tension shift, and strain penetration are ignored in the program as the objective of this method is not a detailed collapse analysis or design. Instead, the main concern is to capture the low-to-moderate damage under an extreme loading in order to activate the early warning system. Having said that, the further damage estimations parameters could be added for the future studies if needed.

4. INVESTIGATION ON THE SEISMIC INTERFEROMETRY AND BUILDINGS WITH INELASTIC RESPONSE

4.1. General Information on the Structure and Earthquake Characteristics

The seismic interferometry and deconvolution & convolution processes are discussed in the first chapter and its efficacy were stated in numerous studies [6-8, 17-34]. Although convolution is a linear process, the limits of seismic interferometry approach needs to be investigated. Besides, it is also a significant point whether the damage correlated parameters can be extracted via the by-products of the wave propagation approach.

Therefore, five 2D structures are modelled in PERFORM 3D [50] and subjected to several excitations. The first three structures are frame structures; each of which represents a certain behavior type. The fourth structure is a dual (frame + wall) building and the last one is a cantilever wall. The FR15A and FR15B have a similar geometry, but the column cross sections are different.

The columns in FR15A are 400 mm x 4000 mm with 3.1% longitudinal reinforcement whereas the column dimension for the latter one is 600 mm x 600 mm with 2% longitudinal reinforcement in order to make sure the strong column – weak beam effect is reflected.

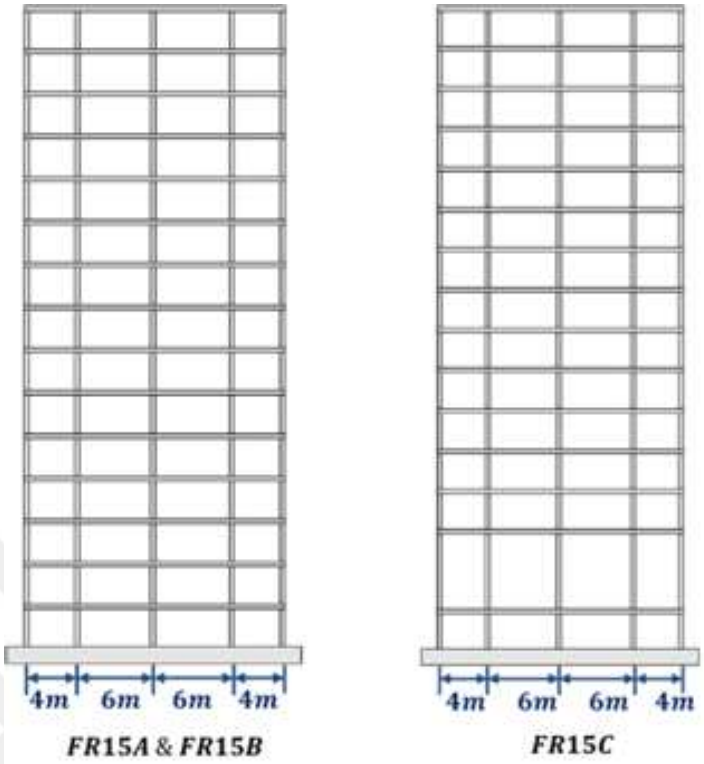

Figure 4.1. The evaluated frame buildings.

The story height in all of the buildings is 3 m, except the second story of the FR15C. The FR15C is a representative building for prominent soft-story effect. The height of the second story is 6 m with the same columns as in the FR15A and in the other stories, the story height is 3 m and the columns have 500 mm x 500 mm cross sectional dimensions with 2.5% longitudinal reinforcement. The beams in the frame-type buildings as well as the following dual structure D15 are 300 mm x 600 mm with 0.6% top and bottom flexural reinforcement. All of the members are heavily confined so that the response can be kept track during all of the excitations. The wall dimensions in the D15 are 6000 mm by 300 mm with 2.05% boundary reinforcement and 0.4% web reinforcement whereas the cantilever W15 wall is 10000 mm by 400 mm with 2.04% boundary reinforcement and 0.5% web reinforcement. The exterior and interior columns for the D15 buildings have 400 mm x 400 mm and 500 mm x 500 mm, respectively with the same amount of longitudinal and transverse reinforcement in the frame structures. The building characteristics such as natural vibration periods for the first 5 modes are given in Table 4.1.

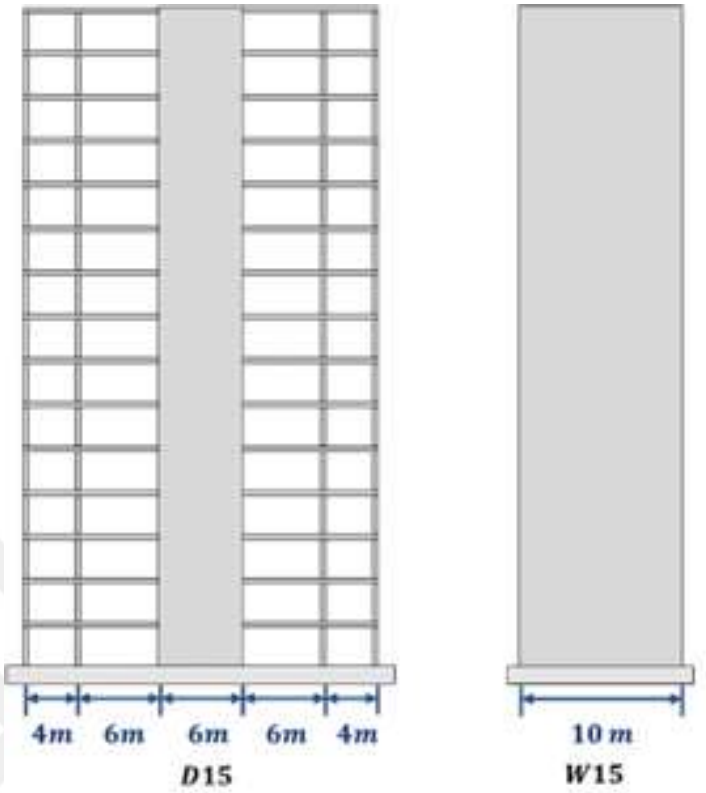

Figure 4.2. D15 and W15 structures.

For the nonlinear time history analysis, 7 earthquake excitations are imposed to the structures. During the selection of the earthquakes, various parameters were taken into account so that the limited number of selected earthquakes would represent various characteristics as much as possible. The earthquakes are downloaded from the PEER Ground Motion Database. The characteristics of the earthquakes as well as abbreviations that will be used hereinafter can be seen in Table 4.2.

Table 4.1. Natural vibration periods for the buildings.

Name	**T_1 (s)**	**T_2 (s)**	**T_3 (s)**	**T_4 (s)**	**T_5 (s)**
FR15A	13.190	0.4311	0.2466	0.1734	0.1330
FR15B	0.9711	0.3126	0.1751	0.1193	0.0880
FR15C	15.030	0.4460	0.2241	0.1477	0.1076
D15	0.849	0.2282	0.1101	0.704	0.0516
W15B	0.6755	0.215	0.0481	0.03176	0.02383

Table 4.2. Earthquake characteristics.

Name	**PGA (g)**	**Pulse-Like**	**Dur (s)**	**Arias Int.**	**CAV (cm/s)**	**Abbrevation**
ChiChi	0.064	NO	260.00	0.20	1096.6	CC
Darfield	0.632	NO	138.65	4.12	2211.2	DE
Duzce	0.806	YES	55.89	2.43	1166.9	D90
Duzce	1.031	NO	30.00	13.37	2876.5	DN
Landers	0.417	NO	28.00	2.18	1123.3	LD
Kocaeli	0.364	NO	27.18	1.33	806.7	D27
Chile	0.707	NO	116.35	15.23	5979.3	CL

4.2. Modeling

The reinforced concrete beam, column, and structural wall members are modelled as fiber element without lumped plasticity model in PERFORM 3D [50]. Although lumped plasticity models for the columns and beams are widely preferred and in most cases more practical, the reason to choose fiber elements is as follows: The aim of this investigation is to capture building response as “accurate” as possible under both low-amplitude and high-amplitude loadings. Therefore, the member and building stiffness changes might be important. For this reason, the beams and columns are modelled as several fiber components along the length in an effort to capture the cracked section stiffness as realistic as possible instead of using elastic elements along the length and assigning effective (cracked section) modifiers. Although the cracked section modulus approach includes the effect of bar slipping and corresponding effects, the order of the

structural deformations and damage for the nonlinear analyses implemented herein is not as high as design/assessment or collapse analyses. The point that is focused herein is to capture the onset of the damage and localize it for early warning purposes. The second reason is to reflect the nonlinear response of the reinforced concrete under low-to-moderate loadings due to the cracking of concrete, even if the deformations are not inelastic which is the case in real-life.

The backbone curve for the inelastic concrete material is adjusted for each confined cross section according to the [52] as shown in Figure 4.3. The adjustment in Figure 4.3 is repeated for each confined member and for the unconfined concrete as well.

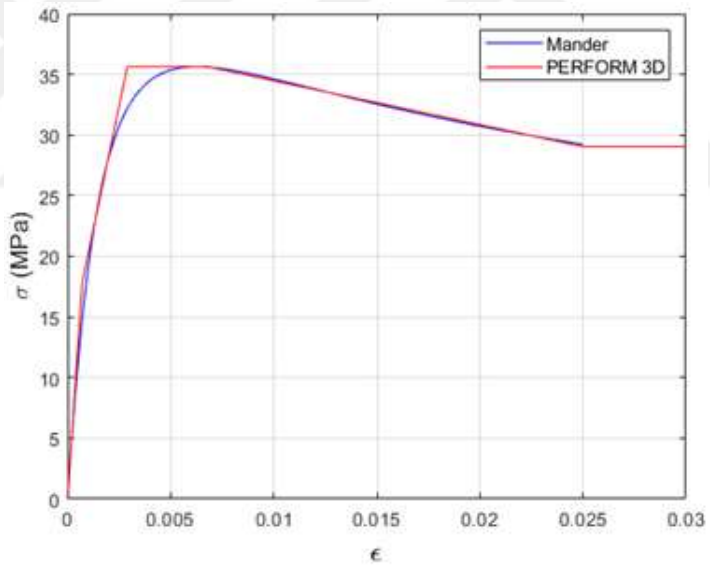

Figure 4.3. Confined concrete stress-strain curve and adjustment to the PERFORM 3D.

The backbone curve in PERFORM 3D is defined via 5 points with optional tri-linear, strength loss, and cyclic degradation parameters. Another modeling parameter is the cyclic degradation. For the cyclic degradation, the energy factors are defined to represent the dissipation of energy as a ratio. The energy degradation factor is defined as the ratio of the area of a loop with stiffness degradation to the area of the loop with

no stiffness degradation. A representative degraded loop is shown in Figure 4.4(b) with bilinear stress-strain relationships. On the right hand side of the figure (a), the shape of the curve used in this study and 5 specified points of the YULRX model are shown. In addition to the energy degradation factors and YULRX points, there is one more parameter for the steel which defines the shape of the curve and called unloading stiffness factor. This parameter take values between -1 and 1 and make adjustments between the stiffness of the unloading curve and the elastic range. The cyclic parameters used in this study are calibrated for the [25] for the reinforcing steel and [54] for the concrete along with the suggestions made for the modelling in PERFORM 3D [55].

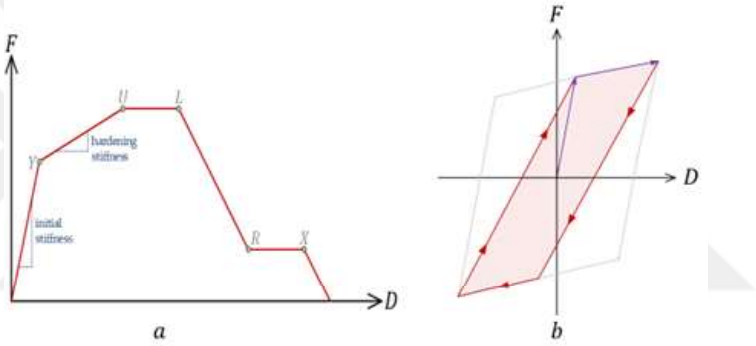

Figure 4.4. The backbone curve and YULRX model (a) and the cyclic energy dissipation.

4.3. Method of Analysis

One of the main objectives of the analyses are to check the applicability of convolution process for an excitation which causes inelastic response in the building. Therefore, all of the buildings are first exposed to Gaussian White Noise to simulate the ambient vibration response, followed by the earthquake excitation to simulate an extreme event leading inelastic activity in the members. At last, Gaussian White Noise is exerted on the building again in order to follow the change in the shear wave velocity of a potentially damaged building after an extreme event. As an example, the

pre-event (white noise), the earthquake excitation, and the post-event response of the top story of the Fr15A is shown in Figure 4.5. All of these excitations are imposed on the building as a sequence to imitate the real-life case as much as possible. That is, a plastic deformation in the building during the earthquake remains plastic during the post-event white noise excitation. However, as might be expected, the post-earthquake response of the 15-story building is dominated by the free vibration response which is damped out quite late. Among the buildings and earthquakes, this free vibration is very prominent for the Fr15A building under D27 earthquake as the predominant period of the earthquake is almost the same as that of the building and a damped resonance response is observed. At first glance, the free vibration response seems to vanish after 40 seconds and seemingly ambient vibration response starts in Figure 4.6. However, this is not the case. When zoomed in the last seconds of the records (160 s), the jagged time trace suggests that the free vibration is still continuing with a smaller amplitude. The impulse response functions are one of the essential tools of the seismic interferometry approach.

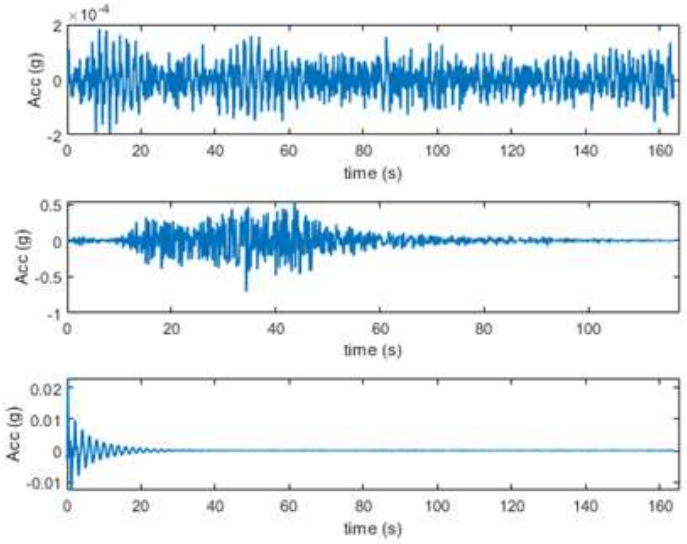

Figure 4.5. The pre-event, Chile (CL) earthquake, and post-earthquake top-story response of the Fr15A building.

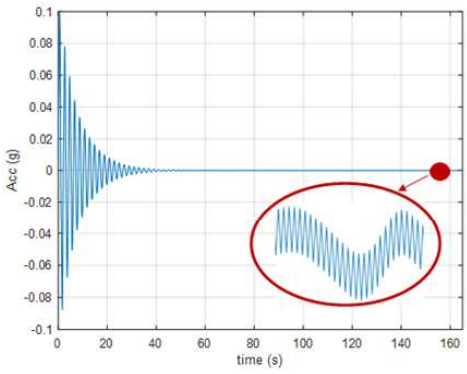

Figure 4.6. The damped free vibration response of the Fr15A under D27 earthquake.

Any of the 2 measured (in this case nonlinear time history analysis output) response quantities can be deconvolved via each other by assuming one of them is the virtual source. The impulse response functions obtained via the base of and the top of the Fr15A building under CC earthquake can be seen in the Figure 4.7. The propagation of the waves can clearly be seen via the peaks of the waves. There are two peaks on the right hand side sub-figure which represent the upgoing and downgoing waves, from left to right. In a real-life building the IRFs are used to estimate the response of the relevant floors without instrumentation by convolving the response of the source signal with the IRF. This is a great advantage for the tall buildings as it is not feasible to deploy sensors at each floor level. However, the applicability convolution comes along with some question marks when nonlinear response is of concern. Therefore, the following analyses are focused on these uncertainties. In order to make the convolution process clear, a comparison between the convolved and the actual (recorded) waves are shown via Figure 4.8 for different floors. At first, the white noise excitation is exerted on the building and then all of the story responses are deconvolved with respect to top floor and the IRF signals for each floor is determined. Then, the building is analyzed under the DE earthquake and the "actual" story responses are retrieved. These recorded (actual) responses are compared with the convolution of the previously found IRFs and the actual response of the top floor (source). The convolved and actual waves of the top floor, mid-floor, and the first floor show agrees well with the actual response quantities.

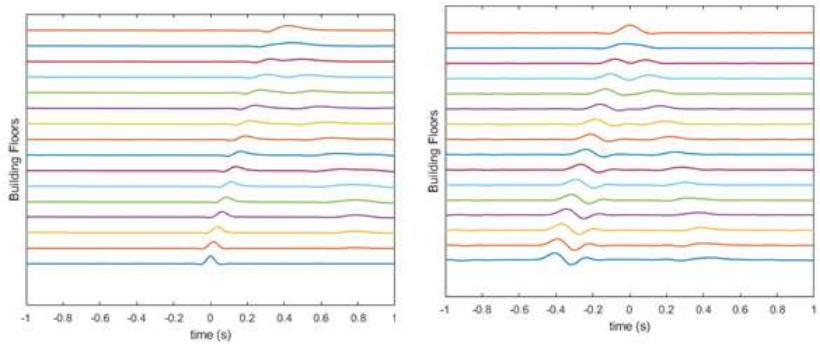

Figure 4.7. The impulse response functions with respect to base (left) and the top (right) at the floor levels for the Fr15A building subjected to CC earthquake.

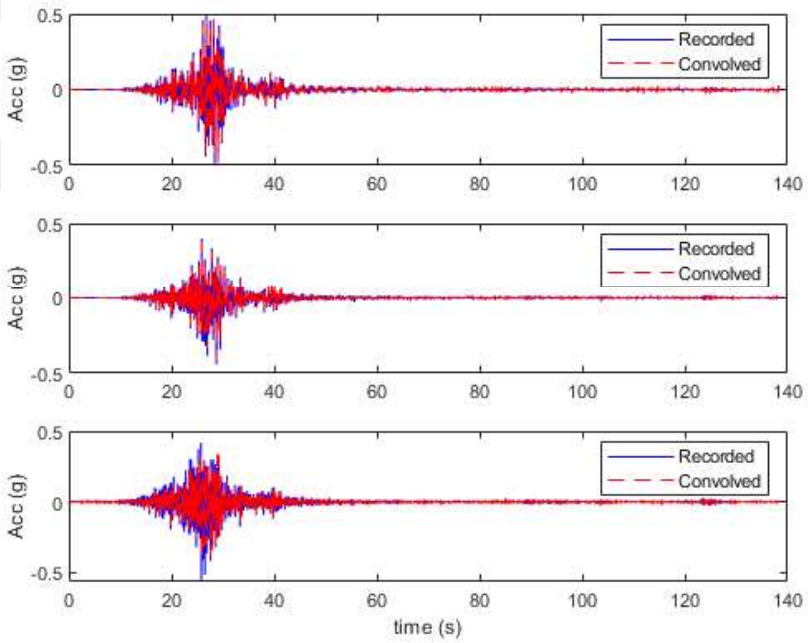

Figure 4.8. Comparison between the convolved and actual responses of the top, seventh, and the first floors for the Fr15A under DE earthquake.

In real life, such an approach helps us not only determine the responses at the non-instrumented floors but also identify the dynamic characteristics of the structure under evaluation.

4.4. Analysis Results

The figures for all of the analysis results for every structure is given in Appendix A in order to prevent congestion.

4.4.1. Interstory Drift Ratios and Ductility Demands

In order to understand the success of the convolution interferometry within the inelastic range, the previously obtained story IRFs are convolved with the earthquake excitations and the results are compared to the actual nonlinear time history analyses. However, a need for defining a parameter arises at this point so that a meaningful relation between the degree of inelastic deformation and the success of the convolution interferometry is possible to establish. The ductility demand seems to be a good candidate for such a need. For each story, the ductility demand is defined in terms of interstory drift ratio since which is one of the clearest and well-correlated damage indicator. The maximum interstory drift ratio among the buildings is around 2.7% in the second story of the Fr15C as expected due to the soft story effect. Although the W15 is a 45 m cantilever wall with 10 m cross section width, the interstory drift ratios are shown in Figure A.5 - Figure A.6 in order to give an idea about the displacement profile of the wall. It should be noted that the earthquake records are scaled with a scale factor of 2.5 for the W15 structure in order to be able to observe the behavior of the convolution and shear wave velocity profile under somehow moderate ductility demand. The ductility demand for each story is defined as the ratio of the maximum interstory drift ratio to the interstory drift ratio at the time step where any of the structural member start yielding as shown in the Eq. 4.1. The i in the below equation represents the story number

$$\mu_i = \frac{(\Delta/H)_i^{onset\ of\ yielding}}{(\Delta/H)_i^{max}}. \tag{4.1}$$

The ductility demand values for each story is demonstrated in the Figure A.6 - Figure A.11. Since the W15 is a cantilever wall structure, the ductility demand is also calculated in terms of roof drift. The only difference of the roof ductility in the Eq.

4.1 is the taking the roof drift ratio as a reference instead of interstory drift ratios. It can be observed that the ductility demands are significantly high especially in the vicinity of the critical wall height. For the frame structures and the dual building, however, the ductility demands ranges between 1-4 for the majority of the earthquakes and the distribution of the ductility demand among the stories for the D90 earthquake prominently differs from the rest due to its pulse-like nature.

4.4.2. Correlation between the Convolved Waves and Actual Responses

The success of the match of the convolution might be measured via the correlation coefficient. The story-wise correlation coefficients relating the actual response with convolved waves with respect to the top and bottom stories of the buildings for each earthquake are illustrated via Figure A.12 - Figure A.21. For the frame structures (except the soft story of the Fr15C), the coefficients mainly vary between 0.9-1.0 except for the LD earthquake whereas this range is between 0.8-1.0 for the D15 building. As can be expected, the degree of the agreement of the convolved and actual responses tend to decrease as getting farther away from the source which is the top of the building. In W15, however, due to the significant yielding and ductility demands, the correlation coefficients are considerably lower than those obtained from the frames and dual systems. This is something expected due to the high nonlinearity in the wall response with the scaled earthquakes. For the case of convolution with respect to base, however, only the first two story responses match very well with the actual response for the majority of the earthquakes. It should be noted that, no signal processing has been performed in order to improve the success of the results since the aim herein is to compare the top and bottom convolved waves and their accuracy keeping all the parameters as fixed as possible.

4.4.3. Ductility Demands and Correlation Coefficients

This is the most important task for this section since one of the main objectives are to measure the quality of the estimation with varying degree of inelastic activity.

The results are significantly satisfactory for the range of ductility demand between 2 and 4 except for the D27 earthquake as can be seen in Figure A.22 - Figure A.27. However, the correlation between the convolved and actual waves are relatively poor (Figure A.27) when compared to the previous case. The potential reason for such an estimation might be the behaviour of the slender cantilever wall and the somewhat high scale factor used for the earthquakes. In a similar way, the correlation coefficients between the actual story responses and the base-convolved waves of the structure are also investigated in the Figure A.28 - Figure A.33 where the agreement seems to be poor as expected. The main difference between success of the top and base convolved waves might be the causality as the waves travel from the base of the structure to top and then goes down towards the base of the structure.

4.4.4. Shear Wave Velocities

As a medium gets stiffer, the shear wave velocity of the waves traveling in that medium increases as well. Therefore, by pick peaking method, the shear wave velocities for the buildings are estimated based on the arrival times of the peaks in the IRFs divided by the story height of the building. The shear wave velocities are calculated for three situations for each earthquake and building. The first one is the pre-event (white noise), the second one is the earthquake excitation, and the last one is the post-event (white noise) situation. The reduction and recover rates of the shear wave velocities are examined in this section.

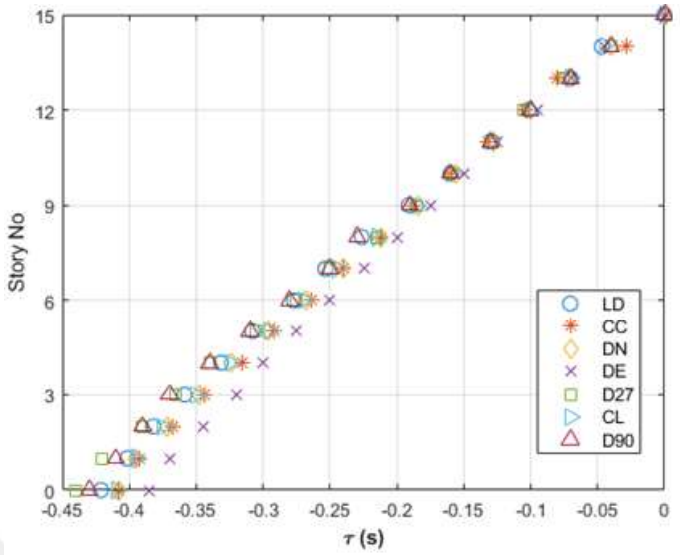

Figure 4.9. The shear wave velocity profiles of the Fr15A during the earthquakes.

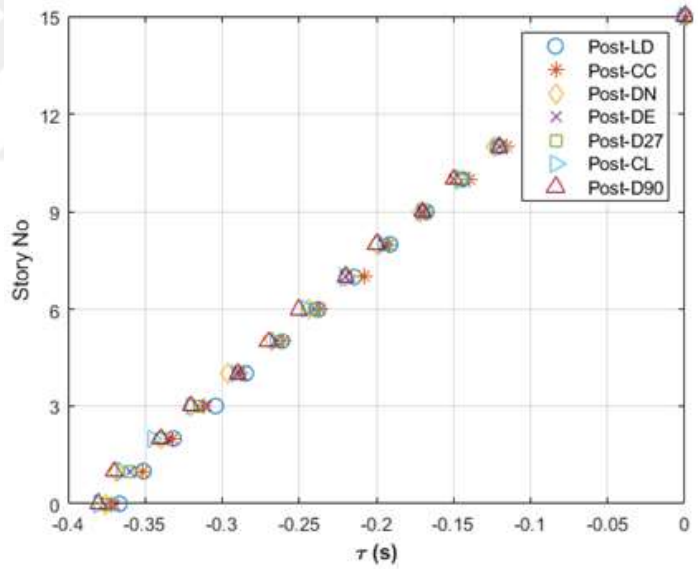

Figure 4.10. The post-earthquake shear wave velocity profiles of the Fr15A.

A representative shear wave profile for the Fr15A building based on the upgoing waves obtained by the deconvolution with respect to top is depicted in Figure 4.9-Figure 4.10.

Table 4.3. Shear wave velocities for the pre-event, earthquake excitations, and post-earthquake.

Excitation	**Fr15A**	**Fr15B**	**Fr15C**	**D15**	**W15**
Pre-Event Vs (m/s)	125	160	165	389	726
LD Vs (m/s)	106.2	135.9	109.7	137.9	128.8
CC Vs (m/s)	110.4	150.0	119.8	289.2	558.5
DN Vs (m/s)	109.1	138.0	137.1	106.6	272.0
DE Vs (m/s)	118.6	152.0	148.4	158.6	225.0
D27 Vs (m/s)	102.7	120.9	106.6	200.4	96.6
CL Vs (m/s)	109.1	148.0	133.3	147.9	215.7
D90 Vs (m/s)	103.1	133.5	114.7	189.4	563.5
PosLD Vs (m/s)	125.2	151.8	149.4	400.1	803.0
PosCC Vs (m/s)	121.6	-	141.8	398.2	781.4
PosDN Vs (m/s)	120.6	156.6	150.7	399.2	744.6
PosDE Vs (m/s)	123.2	157.9	132.4	365.2	726.3
PosD27 Vs (m/s)	121.8	151.2	126.9	388.5	729.0
PosCL Vs (m/s)	120.0	147.3	126.7	359.1	719.7
PosD90 Vs (m/s)	119.7	154.8	155.4	332.9	576.7

As can be seen from the Table 4.3, Fr15A 3and Fr15B the post-event shear wave velocities close to the initial one which is most likely due to the relatively low ductility values. Fr15C (the building with a soft story) suffers stiffness and strength degradation during the DE, D27, and CL earthquakes and the % drop in the V_s reaches up to 23. Although D15 and W15 exhibit significantly prominent decrease in the V_s during the earthquakes, after most of the events the V_s is recovered. However, the pulse like earthquake D90 caused approximately 15% and 21% permanent drop in the V_s. It might be deducted that, the drop in the V_s tends to be more distinct when the inelastic activity is concentrated at a certain location such as the base of a wall or the columns of a soft story. In the structures where the energy absorption is somehow distributed equally among the structural members, the total V_s tend to be recovered following the earthquake.

5. CASE STUDIES FOR VALIDATION

5.1. Case Study for the Method-1

This chapter focuses on the numerical validation of the methods for various scenarios. The first method mentioned in the Chapter 3 will be evaluated via a numerical model and the characteristics of the method will be evaluated. In order to remind the method, Figure 5.1 can be inspected. The "actual" or measured mode shapes of the structure is approximated by the linear superposition of the structural model of the building under consideration.

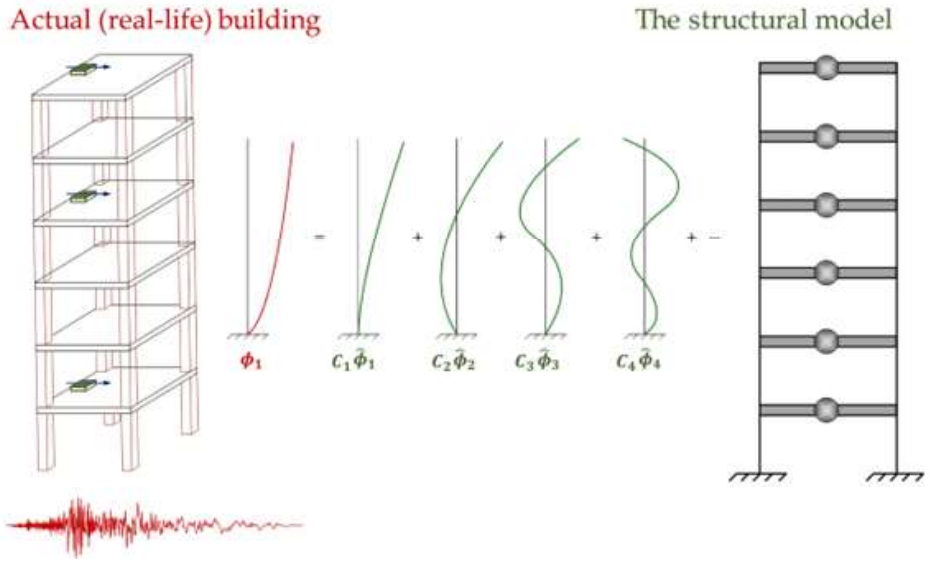

Figure 5.1. Visualization of the Method-1.

Having said that, a case study comparing the proposed Method-1 and one of the methods available in the literature review part [4] is presented below. Finite element model of a 15-story reinforced concrete building is modeled to represent a "mathematical model". Stiffness and mass properties of several stories are changed to imitate the discrepancies between real-life and modeled buildings. The latter (distorted building) is treated as the "actual" or "real life" building. For a given earthquake excitation,

the modal displacements of “the real-life” in one horizontal directions are calculated and these calculated modal responses are adopted as the “measured” displacements. Model mode shapes are taken from the first model and mode shapes are estimated via both methods. The typical floor plan and the mode shapes of the “model” and “real-life” buildings are demonstrated in Figure 5.2. The building is a dual structure with symmetric structural perimeter walls.

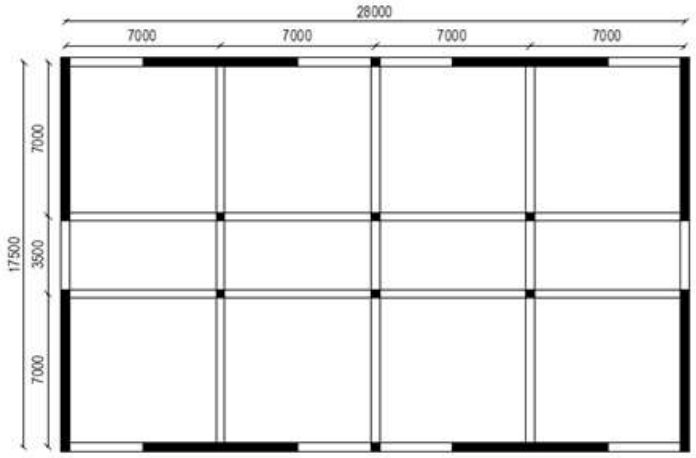

Figure 5.2. Typical floor plan of the sample building (dimensions are in mm).

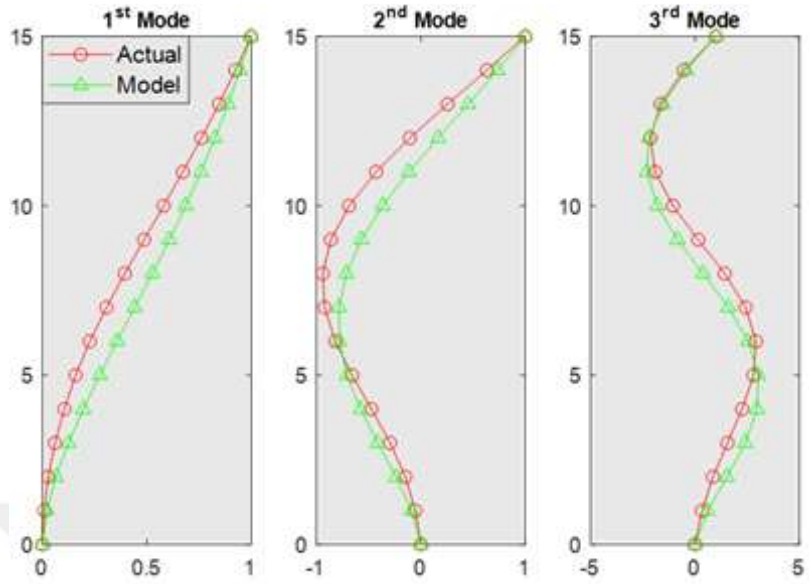

Figure 5.3. The first three x-direction mode shapes of the real-life and model buildings.

Since the participation of the higher mode shapes were negligibly small and does not seem to be pure translational modes, only the first three modes will be evaluated. The success of the estimated mode shapes is measured with the total error. The total error is calculated for each mode by summing the square of the differences between the normalized mode shape amplitudes over the floors. For NIF=3, the optimal sensor locations and the superimposed model modes (for the second method) are obtained by trying all possible combinations of the first six superimposed modes (for the second method) and number of instrumented floors.

Table 5.1. The minimum estimation errors for the method proposed by [4].

Mode	**min error**	**Instrumented Floors**
1	4.02×10-3	1.08.2015
2	2.97×10-1	1.08.2015
3	1.80×10	1.07.2015

The optimal combinations for the locations of the sensors which yield the smallest errors for both methods are depicted in Table 5.1-Table 5.2.

Table 5.2. The minimum estimation errors for the Method-1 (the proposed method).

Mode	**min error**	**Superimposed Modes**	**Instrumented Floors**
1	8.53×10-5	1-2-3	1 - 12 - 15
2	2.33×10-3	1-2-4	1 - 9 - 15
3	3.81×10-1	2-4-5	1 - 7 - 15

As can be seen from the above tables, the errors in the proposed method is considerably less than the available method. However, the accuracy of the proposed method significantly depends on the selected model modes. The trials performed for all possible combinations suggest that successive model modes around the target mode can be selected as a rule of thumb. For a fixed instrumented floor configuration and successive superimposed modes, the proposed method (Method-1) achieves better results for the first two modes with satisfactory error orders as can be seen in the Table 5.3.

Table 5.3. The estimation errors of the methods for fixed parameters.

Method	**Mode**	**Error**	**Superimposed Modes**	**Instrumented Floors**
I	1	4.02×10-3	-	1 - 8 - 15
II	1	9.08×10-5	1-2-3	1 - 8 - 15
I	2	2.97×10-1	-	1 - 8 - 15
II	2	6.17×10-2	1-2-3	1 - 8 - 15
I	3	1.86×10	-	1 - 8 - 15
II	3	2.02×10	1-2-3	1 - 8 - 15

5.2. Case Study for the Method-2

For the validation of the Method-2, Fr15A and its 10-story variant have been selected as the beam sections (300 mm x 600 mm) are stiffer than the columns (400

mm x 400 mm) and thus the behavior is relatively closer to a shear frame. Among the earthquakes, DN is selected and scaled with 2 so that the damage is more prominent. The reason for the selection of the DN earthquake is to understand the behavior of the method for the earthquakes under which the convolution yields relatively low correlation coefficients for the inelastic case.

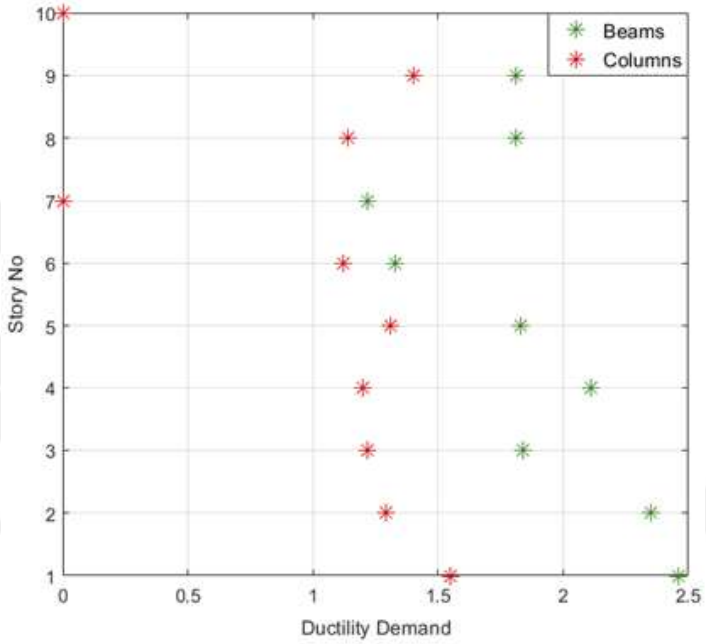

Figure 5.4. Ductility demand for Fr10A subjected to DN scaled by a factor of 2.

Almost all of the structural members in the Fr10A (which is similar to Fr15A, but has 10 stories) undergo inelastic deformations with a maximum μ value of approximately 2.5 as can be seen in Figure 5.4. It is a significant example as the columns also behaves inelastic manner except the 7^{th} and 10^{th} stories. As has been explained in the Chapter 3, the structural analysis of such a high-degree indeterminate system requires some assumptions which will facilitate analyzing the system. Therefore, the PI assumption for the beams and columns are utilized at this point. The PI values are calculated via Eq. 3.11 while for the beams it is taken constant as 0.5L. In order to approximate the joint rotations at the ends of each column, two methods are used. The first one (model-based) relies on a numerical model (preferably calibrated with the Method-1) while there are no numerical models for the second one (derivative-based),

but only taking numerical derivative of the lateral displacement profile of the structure at any given time t for an excitation. The displacement profile for the buildings can be seen in Figure 5.5 and Figure 5.6 for the time instant for which all the analyses have been carried out.

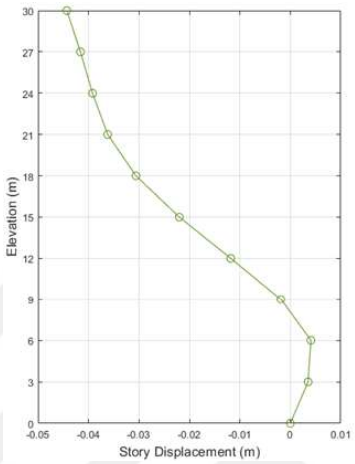

Figure 5.5. The lateral story displacements for the Fr10A subjected to the DN earthquake scaled by a factor of 2.

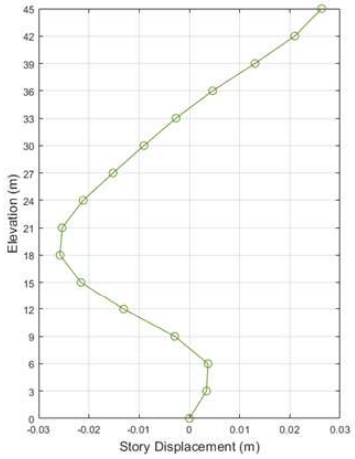

Figure 5.6. The lateral story displacements for the Fr15A subjected to the DN earthquake scaled by a factor of 2.

The higher mode effects due to dynamic nature of earthquake and the resulting cross-overs in the displacement profile makes the estimation of joint rotations much more difficult. While it is possible to find the "exact" joint rotations by the approach

that relies on the numerical model and superposition of mode shapes for a first mode dominant static excitation, such as pushover. The Figure 5.7-Figure 5.8 show the estimated and actual joint rotations for each column. Based on Figure 4.1, the Axis-1 in the Figure 5.7-Figure 5.8 are the vertical column axis on the leftmost hand-side while the Axis-5 is the axis on the rightmost side. The axes have been enumerated from left to right.

The disadvantage of the derivative-based method is there is only one displacement profile to take the derivative which suggests a single joint rotation values for all the columns located at a given floor. However, the trade-off herein is to be able to estimate the internal forces without needing a detailed numerical model of the structure. On the other hand, the model-based method does not perfectly match for some axes especially for the Fr10A building.

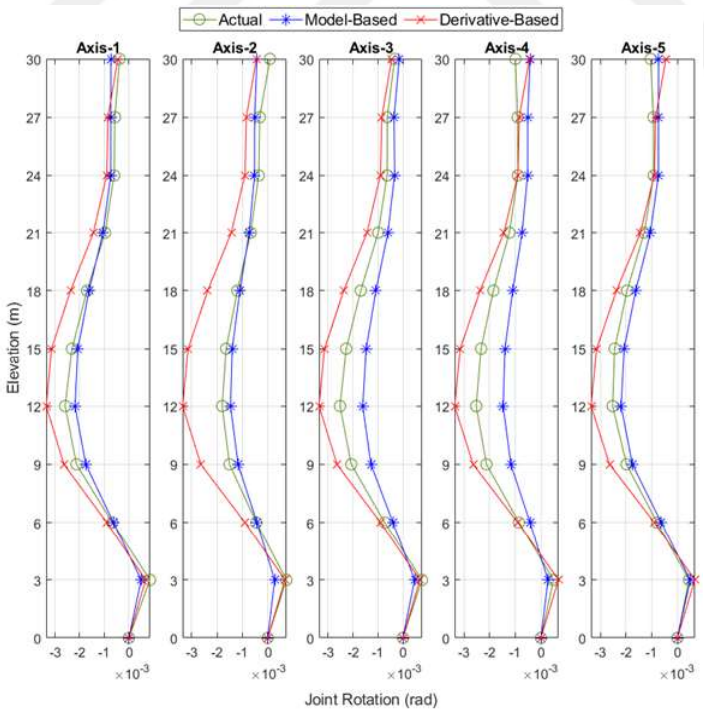

Figure 5.7. The approximate joint rotations for each column estimated by model-based and derivative-based methods and the actual joint rotations for Fr10A.

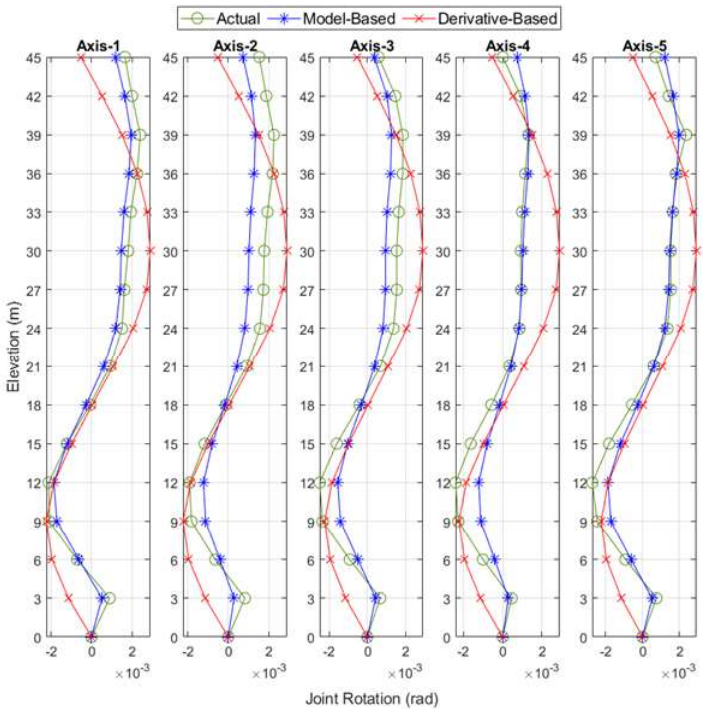

Figure 5.8. The approximate joint rotations for each column estimated by model-based and derivative-based methods and the actual joint rotations for Fr15A.

Once the joint rotations are obtained, the algorithm finds the "pure flexural" displacements by eliminating the effects of joint rotations and also calculates the location of the point of inflection for the columns based on the Eq. 3.11. The method is able to find the PI values above 1 or below 0, i.e., it still works for the case of single curvature. Starting from the uppermost corners, the algorithm obtains internal forces by iterating the unknown variables in a nested loop. The internal forces for the members are given in the Appendix B for both buildings.

The axial forces, bending moments for both i and j ends, and shear forces for the columns are illustrated in Appendix B. Figure B.1-Figure B.3 and Figure B.7-Figure B.9 shows the ratio of the estimated / actual internal forces for the columns per each story regarding the Fr10A and Fr15A, respectively. The normalized actual and estimated internal forces for all of the columns in a building without separating them according to the stories are given via Figure B.4-Figure B.6 and Figure B.11-

Figure B.12 for Fr10A and Fr15A, respectively so that it would be easier to understand the general success of the approximations. For both of the buildings, the least successful estimations are the column end moments, especially at the intermediate stories where the displacement profile changes direction and the best estimates in total are the axial forces on the columns. As expected, the model-based method performs better than the derivative-based method. However, both of the approximations perform very well at the first story which is usually the most critical story. The reason for that is probably the restraints at the base which ensures zero rotation at the i end of the columns, and hence, reduces one of the uncertainties. In the upper stories, however, the location of the PI is sensitive to the joint rotations at both hands. Therefore, a small error in the estimation of the joint rotations may lead larger errors in the resulting PI values and finally internal forces. Having said that, the error in the majority of the moment estimations for both buildings are still acceptable given that moment estimations are the least successful ones.

When applying the Method-2 (Inelastic Reverse Drift Algorithm), to the structural walls, there is no need for the joint operations and the structural wall is considered as a single cantilever. Therefore, Eq. 3.9 can be directly used for estimating the internal forces for the reinforced concrete structural walls. Each story (actually story herein means the section of the wall between two measurement points) is considered to consist of only one vertical fiber and the moments at the middle of each fiber is computed as per Eq. 3.9. Figure 5.9 and Figure 5.10 shows the estimated and actual moment profiles during an instant of the excitation. The shear deformations in the wall are ignored and the it is assumed that the wall deforms only in flexure. Of course, this is not a realistic assumption even for slender walls whose responses are mainly dominated by flexure. However, in case of such little number of sensors as used in this study, it is not possible to determine the shear deformations of the wall, and yet, practical methods such as proposed [56] might be implemented to the algorithm in the future updates.

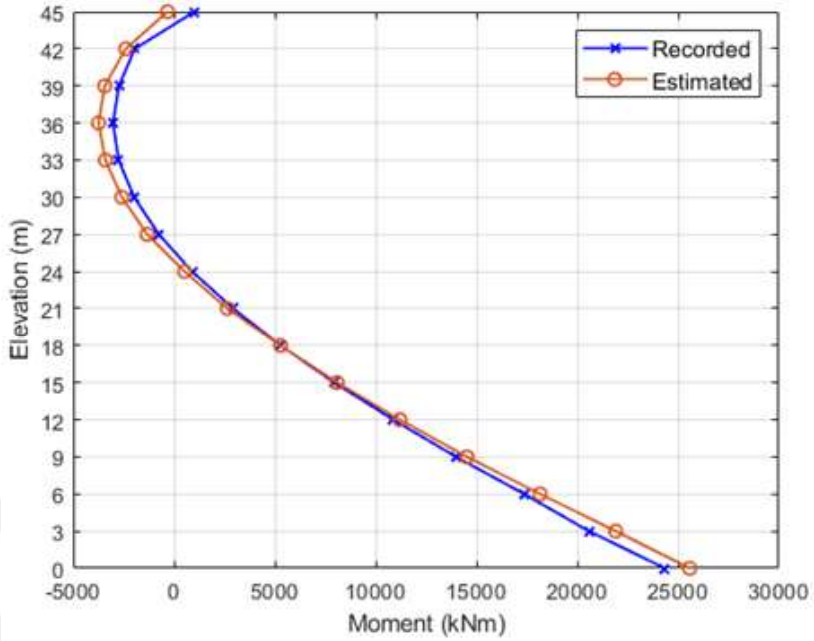

Figure 5.9. Recorded and estimated bending moments for the structural wall in D15.

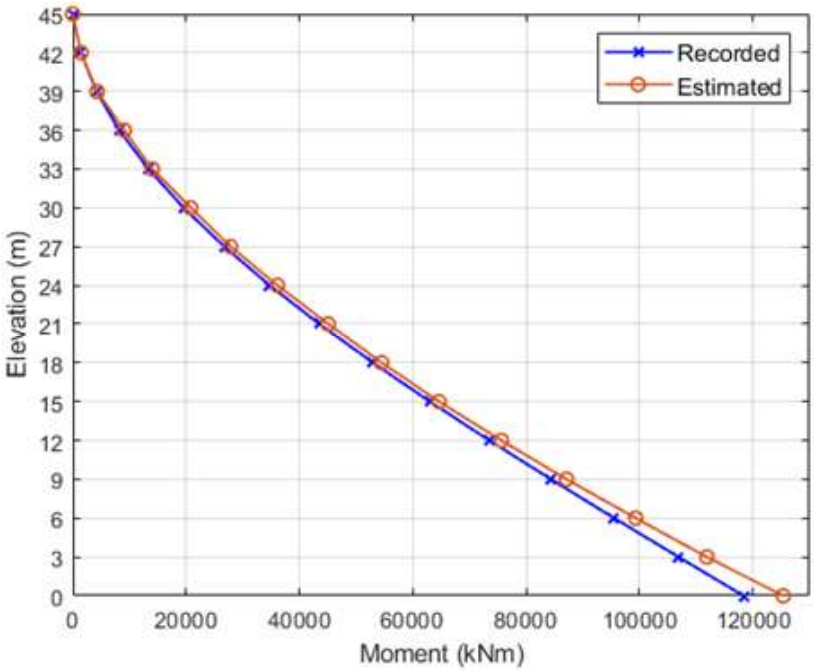

Figure 5.10. Recorded and estimated bending moments for the structural wall W15.

5.3. Case Study on the Effect of Noise

In real-life structures, noise is always present from various sources as discussed in the Literature Review section as well as other issues that deteriorates the displacements obtained by double integration of the acceleration data. Since this study is validated by numerical models and there will never be a noise-free data in real, 10% RMS of the actual acceleration data retrieved from the nonlinear structural analysis is added to the original record to imitate the effect of the noise. For this, Gaussian White Noise is generated randomly and scaled. The original and the noisy acceleration data is depicted in Figure 5.11.

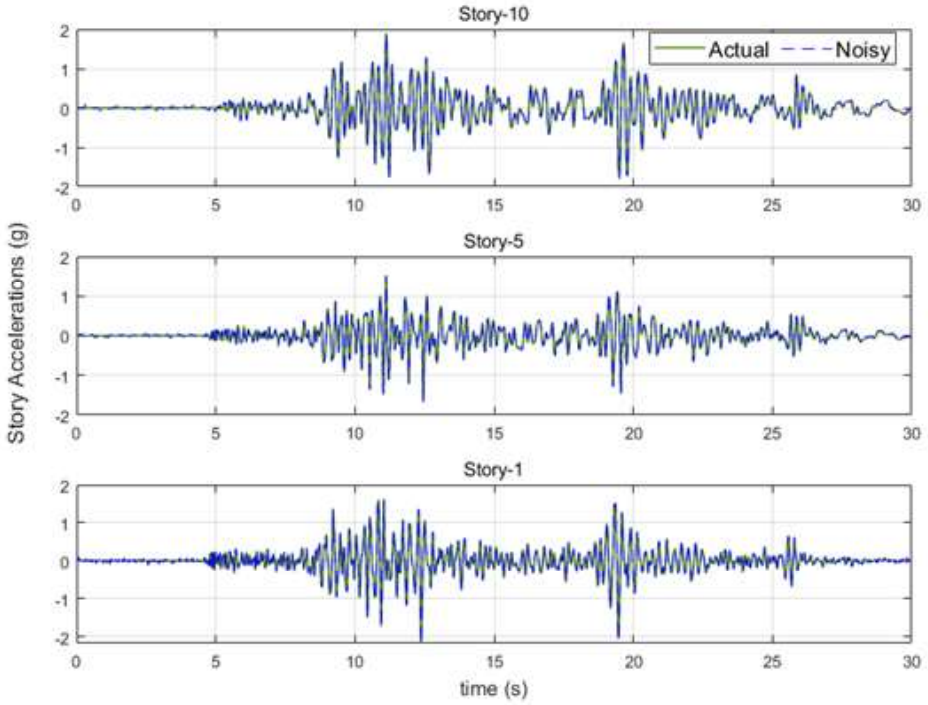

Figure 5.11. The original and the noisy acceleration data for the 1st, 5th, and 10th stories of Fr10A.

For the analysis, Fr10A is used and the excitation is chosen as the DN earthquake with a linear scale factor of 2. If this raw data is integrated, the resulting displacements are unrealistic with huge errors. Therefore, the data has been processed so that it is

as much ready as it is for double integration. However, there is no unique way or order of processing earthquake data. Besides, the simulated noise does not have a specific frequency range which relatively easier to remove. Instead, it is Gaussian white noise which has a constant power spectral density.

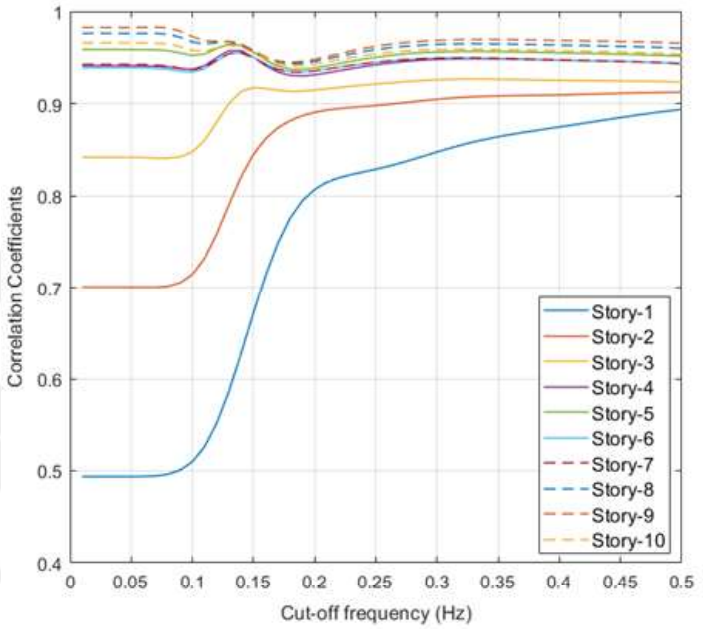

Figure 5.12. Correlation coefficients between the actual and noisy story displacements obtained by double integration vs the cut-off frequencies of the high pass filter applied to the noisy acceleration responses.

High-pass filter is usually the best solution for the elimination of the long-period noise which causes large errors in double integration. Therefore, in order to eliminate the long-period noise, a fourth order high-pass Butterworth filter is applied to data acceleration data with a cut-off frequency of 0.2 Hz. Although it is a widely used number, it is still subjective. Therefore, a sensitivity study has been carried out to analyze the effect of the cut-off frequency on the quality of the estimation of the story displacements obtained by numerical double integration. Figure 5.12-Figure 5.14 shows the sensitivity of the correlation coefficients between the actual and estimated displacements, ratio of the peak displacements, and signal to noise ratio to the selected cut-off frequency for the high-pass filter. The signal to noise ratio of the filtered displacements

are calculated as in the Eq. 5.1.

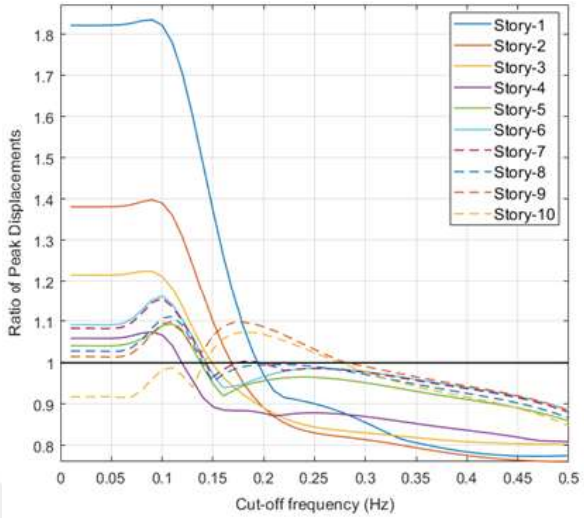

Figure 5.13. Noisy / actual ratio of peak story displacements vs the cut-off frequencies of the high pass filter applied to the noisy acceleration responses.

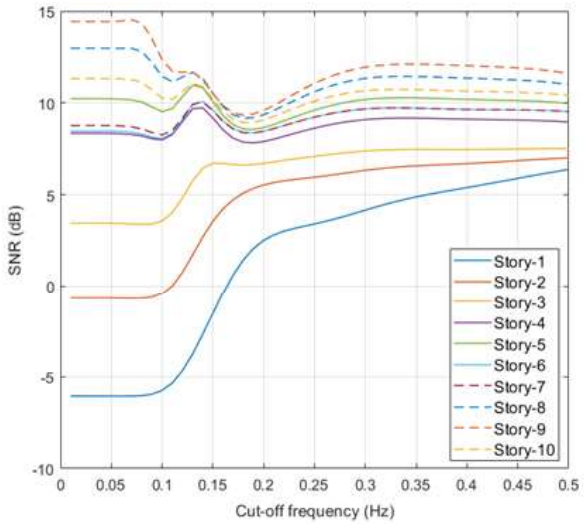

Figure 5.14. SNR of the story displacements vs the cut-off frequencies of the high pass filter applied to the noisy acceleration responses.

In the Eq 5.1, RMS_{error} is the RMS of the error which is obtained by subtracting the actual displacements from the displacement obtained by double integration of

the filtered accelerations. In terms of correlation coefficients and SNR, the best cut-off frequency seems to be less than 0.1 Hz while for the lower stories, the correlation improves as the cut-off frequency increases. For the ratio of peak displacements, the cut-off frequencies between 0.15-0.2 Hz gives the closest ratio to unity for the lower stories. However, there is no "best" cut-off frequency for the upper stories that ensures a peak displacement value around 1. However, the cut-off frequencies smaller than 0.6 Hz and between 0.15-0.3 Hz seem reasonable. As the higher story responses inherently contain low-frequency components, increasing the high-pass corner period causes decrement in the amplitude and filtering the "actual" components whereas the low-frequency components in the bottom stories are much likely to be non-structural, the signal quality of the lower stories improves with the increasing high-pass filter corner frequency.

$$SNR\ (dB) = 20 \log \left(\frac{RMS_{actual}}{RMS_{error}} \right) \tag{5.1}$$

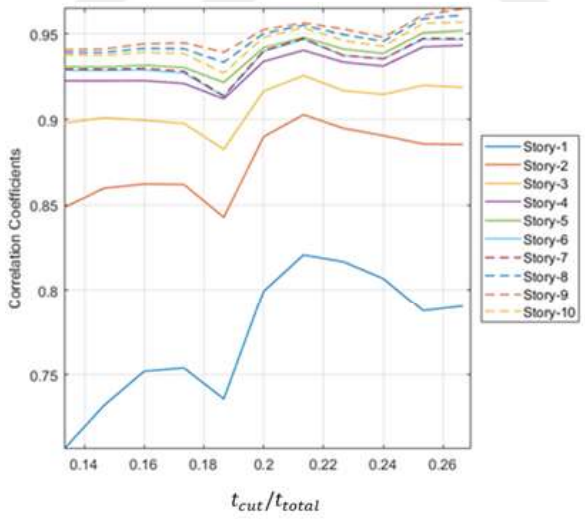

Figure 5.15. Change of the correlation coefficient with varying separation point of the data for which a different polynomial is fit.

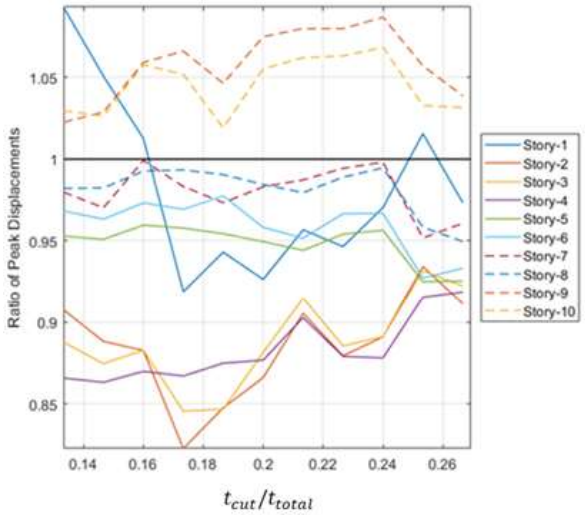

Figure 5.16. Change of the peak story displacements with varying separation point of the data for which a different polynomial is fit.

One of the most common methods as the first step in the processing earthquake data is to remove the constant pre-event mean. However, it is usually not enough because the different segments of the data have different baselines [35, 38] which can be realized by visual inspection of the velocity traces. Therefore, polynomials are fitted to the velocity traces and then subtracted because the constant (zeroth order) and linear (1^{st} order) detrending (removal of the baselines) apparently did not work well based on the visual inspection of the trends in the velocity traces. The velocity data are separated into two segments and a different polynomial fit to each segment. The key parameter is where to cut the data. Therefore, sensitivity analyses were conducted in the same manner with the cut-off frequency, but this time the variable is the ratio of the time instant where the data is separated (t_{cut}) to the total duration of the earthquake. Except the ground story, the floor displacements do not seem to be very sensitive to the selection of t_{cut} in terms of correlation coefficients and signal to noise ratio according to the Figure 5.15 and Figure 5.17, respectively. As for the ratio of peak displacements, none of the stories appear to be sensitive to the t_{cut} (Figure 5.16).

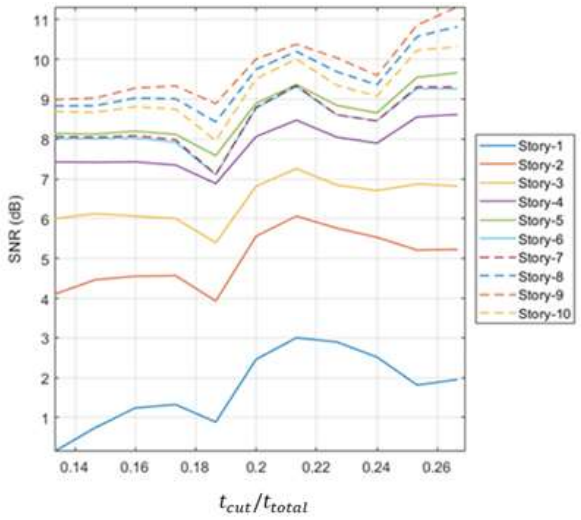

Figure 5.17. Change of the SNR with varying separation point of the data for which a different polynomial is fit.

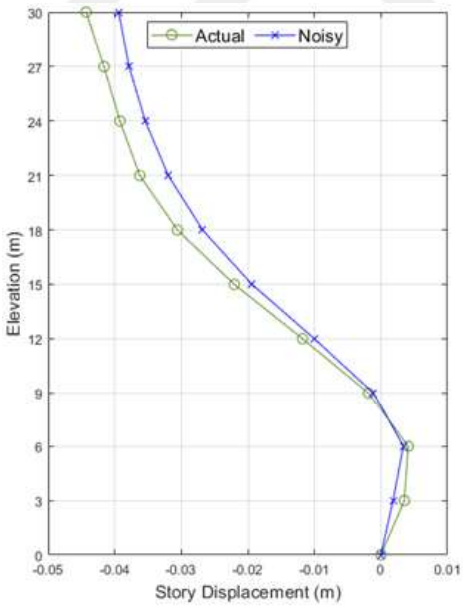

Figure 5.18. Actual and noisy story displacements after processing the noisy data.

Consequently, the corner frequency of the high-pass filter and the t_{cut}/t_{total} have been selected as 0.2 Hz and 0.24 for the determination of the interstory drifts and internal forces. The corresponding story drifts and the estimated joint rotations can

be inspected via Figure 5.18-Figure 5.19.

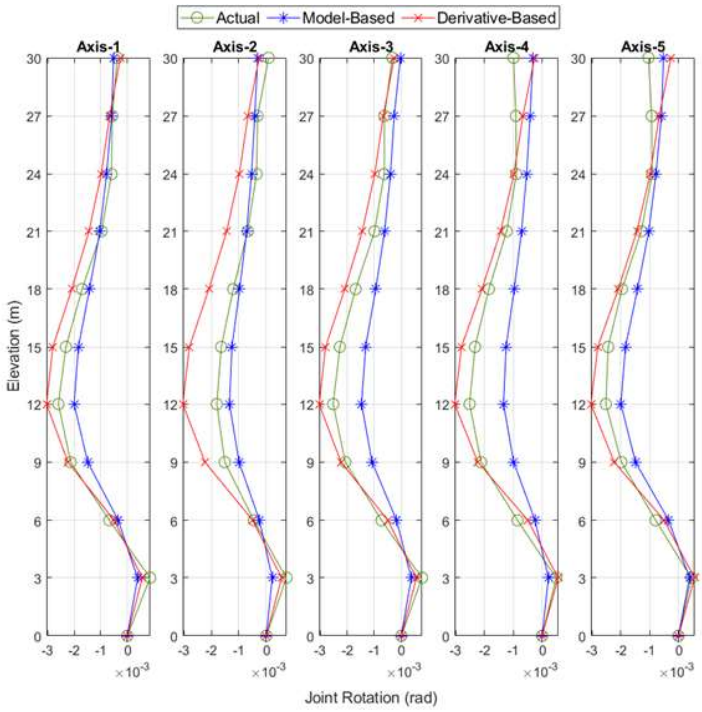

Figure 5.19. The approximate joint rotations for each column estimated by model-based and derivative-based methods and the actual joint rotations for Fr10A in the case of noise with 10% RMS.

The internal forces at the end of analyses are illustrated in Appendix C. Although estimation of the internal forces might suffer in some intermediate stories, the results are satisfactory in general. Especially, the shear and bending moments in the base columns performs very well despite the Gaussian white noise with 10% RMS. However, it should be noted that the steps to follow and choices made are subjective in the processing of earthquake data and therefore different choices might lead better or worse results. However, the 0.2 Hz high-pass filter frequency is believed to be a "general" and plausible value.

6. SUMMARY AND CONCLUSIONS

Two separate methods are proposed and evaluated in this study for structural health monitoring and damage detection of tall buildings. The first method discussed herein, aims to predict the response of the structure at non-instrumented floors. This is achieved by approximating the actual mode shape of the structure as linear combinations of the mode shapes of the mathematical model of the structure under investigation. A weighting coefficient is obtained for each model mode shape by the minimization of the error between the estimated and actual response quantities. In the last step of the method, the physical response quantities are obtained via the relationship between the modal and the physical coordinates. The second method focus on the predicting the damage and response quantities in the structure under severe loadings such as earthquake or wind. The method aims to conduct the health monitoring by using minimum possible of sensors. The method relies on the seismic interferometry and wave propagation. Scanning phase is the common step of the both methods where the building is scanned with several accelerometers. Two of the accelerometers are kept fixed at the base and the top of the structure so that the virtual sources (reference signals) do not change. The limited number of other sensors are then moved among the stories and the impulse response functions for each story is obtained via deconvolution with respect to top and base of the structure. Once this step is completed, the story responses can easily be predicted via the convolution of the impulse response functions of the stories with the reference signal; the base or the top of the building. The estimated story drifts are used as one of the inputs and then the internal force and deformation quantities at any desired point of the structure is computed. There are two types of the programs coded herein; the first one for evaluating the frame part of the structure and the second one which is dedicated to the reinforced concrete structural walls. As a result, the proposed method is devoted to monitor the building with only 2 sensors and predict the internal force and deformations in the members with 2 options. The first option requires a 3D computer model of the actual building whereas in the second method no numerical model is needed.

The scope of the proposed Method 2 encompasses reinforced concrete buildings with relatively regular framing systems, rigid diaphragms, and structures whose responses are mainly governed by flexure. Also, this method does not encompass structures that have been subjected to severe damage and significant cyclic degradation. This method aims to capture onset of the inelastic activity or the nonlinear behavior in relatively low ductility demands.

In this study, the extend of the deconvolution interferometry and convolution is also tested and the analysis results reveal that up to ductility levels of 2.5-3.5, the convolution of the IRFs with the reference signals still generates acceptable and usable responses.

It might be deducted that, the drop in the V_s tends to be more distinct when the inelastic activity is concentrated at a certain location such as the base of a wall or the columns of a soft story. This deduction may also be valid for the success convolution. As the energy absorption is concentrated at a single location, the correlation coefficients drop with increasing ductility demand. In the structures where the energy absorption is somehow distributed equally among the structural members, the total V_s tend to be recovered following the earthquake.

The convolution with respect to the top of the buildings satisfactorily captures the nonlinear response whereas convolving the IRFs with respect to the base of the structure do not appear to capture the nonlinear response. There might be several candidate reasons for this: (i) causality, (ii) concentration of the inelastic deformations at the base, (iii) short duration of some of the earthquakes. Also, the precision of the convolved waves with respect to top naturally decreases in the downward direction for high ductility demands, especially for the structural walls. However, this drop is believed to be insignificant for the majority of the structures and earthquakes unless the ductility demand is high. It would be plausible to estimate the response of the closest stories to the base via convolving the IRFs obtained with respect to the base.

The analysis results suggest that this method estimates the internal forces of the columns reasonably well in the intermediate stories and very well in the base story. Even with a noisy data, the bending moments and shear forces in the base columns and the bending moment profiles of the structural walls (along the height) matches very well with the nonlinear history analysis results. The reason for the estimation success regarding the base columns might be the fixed-base column ends where the rotation is zero. Overall, the proposed method can be used to estimate the total base shear and overturning moments without needing a numerical model.

The drawbacks of this method is the sensitivity of the location of the PIs to the joint rotations. Although two approximations have been proposed to estimate the joint rotations, the PI locations are quite sensitive to the joint rotations at the column ends. However, the algorithm is capable of capturing the PI values which are greater than 1 or smaller than zero which means single curvature in the columns.

In the future, some of these issues can be resolved by: (i) using rotation sensors at certain locations, (ii) obtaining the displacements directly via GPS or image processing, (iii) improving the reverse nonlinear analysis algorithm so that the shear deformations in the structural walls are also accounted for.

REFERENCES

1. Skolnik, D. A., W. J. Kaiser, and J. W. Wallace, "Instrumentation for Structural Health Monitoring: Measuring Interstory Drift", *Proceedings of the 14th World Conference of Earthquake*, Bejing, China, 2008.

2. W.D. Iwan, "Drift Spectrum: Measure of Demand for Earthquake Ground Motions", *Journal of Structural Engineering*, Vol. 123, pp. 397–404, 1997.

3. Miranda, E. and S. D. Akkar, "Generalized Interstory Drift Spectrum", *Journal of Structural Engineering*, Vol. 132, No. 6, pp. 840–852, 2006.

4. Kaya, Y., S. Kocakaplan, and E. Şafak, "System Identification and Model Calibration of Multi-Story Buildings Through Estimation of Vibration Time Histories at Non-Instrumented Floors", *Bulletin of Earthquake Engineering*, Vol. 13, No. 11, pp. 3301-3323, 2015.

5. Iliopoulos, A., W. Weijtjens, D. Van Hemelrijck, and C. Devriendt, "Fatigue Assessment of Offshore Wind Turbines on Monopile Foundations Using Multi-Band Modal Expansion", *Wind Energy*, Vol. 20, No. 8, 1463-1479, 2017.

6. Kanai, K. and S. Yoshizawa, "Some New Problems of Seismic Vibrations of a Structure Part 1", *Bulletin of Earthquake Resarch Instute*, Vol.41, pp. 825–833, 1963.

7. Ebrahimian, M., M. D. Trifunac, and M. I. Todorovska, "Prediction of Building Response at any Level from Recorded Roof Response: The Kanai–Yoshizawa Formula Revisited", *Soil Dynamics and Earthquake Engineering*, Vol. 80, pp. 241-250, 2016.

8. Ebrahimian, M. and M. D. Trifunac, "Calculating a Building Response at Different Levels from a Single Roof Accelerogram", *Department of Civil Engineering*, Report

CE 15-01, University of Southern California, Los Angeles, California, United States of America, 2015.

9. Palermo, M., S. Silvestri, and T. Trombetti, "On the Peak Inter-Storey Drift and Peak Inter-Storey Velocity Profiles for Frame Structures", *Soil Dynamics and Earthquake Engineering*, Vol. 94, pp. 18–34, 2017.

10. Chen, M. C., R. Astroza, J. I. Restrepo, J. P. Conte, T. Hutchinson, and Y. Bock, "Predominant Period and Equivalent Viscous Damping Ratio Identification for a Full-Scale Building Shake Table Test", *Earthquake Engineering & Structural Dynamics*, Vol. 46, No. 14, pp. 2459–2477, 2017.

11. Farrar, C. R. and D. A. Jauregui, "Comparative Study of Damage Identification Algorithms Applied to a Bridge: I. Experiment", *Smart Materials and Structures*, Vol. 7, pp. 720, 1998.

12. Curadelli, R. O., J. D. Riera, D. Ambrosini, and M. G. Amani, "Damage Detection by Means of Structural Damping Identification", *Engineering Structures*, Vol. 30, No. 12, pp. 3497–3504, 2008.

13. Uebayashi, H., M. Nagano, T. Hida, T. Tanuma, M. Yasui and S. Sakai, "Evaluation of the Structural Damage of High-Rise Reinforced Concrete Buildings Using Ambient Vibrations Recorded Before and After Damage", *Earthquake Engineering & Structural Dynamics*, Vol. 45, No. 2, pp. 213-228, 2016.

14. Xia, Y., P. Zhang, Y. Qing Ni, and H. Ping Zhu, "Deformation Monitoring of a Super-Tall Structure Using Real-Time Strain Data", *Engineering Structures*, Vol. 67, pp. 29–38, 2014.

15. Guo, Y., D. K. Kwon, and A. Kareem, "Near-Real-Time Hybrid System Identification Framework for Civil Structures with Application to Burj Khalifa", *Journal of Structural Engineering*, Vol. 142, No. 2, pp. 04015132-1-15, 2016.

16. Sun, H. and O. Büyüköztürk, "The MIT Green Building Benchmark Problem for Structural Health Monitoring of Tall Buildings", *Structural Control and Health Monitoring*, Vol. 25, pp. e2215, 2017.

17. Todorovska, M. I. and V. W. Lee, "Seismic Waves in Buildings with Shear Walls or Central Core", *Journal of Engineering Mechanics*, Vol.115, No. 12, pp. 2669-2686, 1989.

18. Todorovska, M. I., and M. D. Trifunac, "Antiplane Earthquake Waves in Long Structures", *Journal of Engineering Mechanics*, Vol. 115, No.12, pp. 2687-2708, 1989.

19. Şafak, E., "Propagation of Seismic Waves in Tall Buildings", *The Structural Design of Tall Buildings*, Vol. 7, No. 4, pp. 295-306, 1998.

20. Snieder, R. and E. Şafak, "Extracting the Building Response Using Seismic Interferometry: Theory and Application to the Millikan Library in Pasadena, California", *Bulletin of the Seismological Society of America*, Vol. 96, No. 2, pp. 586-598, 2006.

21. Nakata, N., R. Snieder, S. Kuroda, S. Ito, T. Aizawa, and T. Kunimi, "Monitoring a Building Using Deconvolution Interferometry. I: Earthquake-Data Analysis", *Bulletin of the Seismological Society of America*, Vol. 103, No. 3, pp. 1662-1678, 2013.

22. Todorovska, M. I. and M. D. Trifunac, "Earthquake Damage Detection in Structures and Early Warning", *In the 14th World Conference on Earthquake Engineering*, Bejing, China, 2008.

23. Lacanna, G., M. Ripepe, M. Coli, R. Genco, and E. Marchetti, "Full Structural Dynamic Response from Ambient Vibration of Giotto's Bell Tower in Firenze (Italy), Using Modal Analysis and Seismic Interferometry", *NDT & E International*, Vol.

102, pp. 9-15, 2019.

24. Todorovska, Maria I. and M. D. Trifunac, "Impulse Response Analysis of The Van Nuys 7-Storey Hotel During 11 Earthquakes and Earthquake Damage Detection", *Structural Control and Health Monitoring: The Official Journal of the International Association for Structural Control and Monitoring and of the European Association for the Control of Structures*, Vol. 15, No.1, pp. 90-116, 2008.

25. Mulhern, M. R. and R. P. Maley, "Building Period Measurements Before, During and After the San Fernando Earthquake", *San Fernando, California, Earthquake of February*, Vol. 9, 1971.

26. Todorovska, M. I., and M. D. Trifunac, "Earthquake Damage Detection in The Imperial County Services Building III: Analysis of Wave Travel Times via Impulse Response Functions", *Soil Dynamics and Earthquake Engineering*, Vol. 28, No. 5, pp. 387-404, 2008.

27. Todorovska, M. I. and M. T. Rahmani, "System Identification of Buildings by Wave Travel Time Analysis and Layered Shear Beam Models—Spatial Resolution and Accuracy", *Structural Control and Health Monitoring*, Vol. 20, No. 5, pp. 686-702, 2013.

28. Rahmani, M. and M. I. Todorovska, "1D System Identification of Buildings During Earthquakes by Seismic Interferometry with Waveform Inversion of Impulse Responses—Method and Application to Millikan Library", *Soil Dynamics and Earthquake Engineering*, Vol. 47, pp. 157-174, 2013.

29. Ebrahimian, M. and M. I. Todorovska, "Wave Propagation in a Timoshenko Beam Building Model", *Journal of Engineering Mechanics*, Vol. 140, No. 5, pp. 04014018-1-11, 2014.

30. Rahmani, M. and M. I. Todorovska, "Structural Health Monitoring of a 32-Storey

Steel-Frame Building Using 50 Years of Seismic Monitoring Data", *Earthquake Engineering and Structural Dynamics*, Vol. 50, No. 6, pp. 1777-1800, 2021.

31. Ebrahimian, M. and M. I. Todorovska, "Structural System Identification of Buildings by a Wave Method Based on a Nonuniform Timoshenko Beam Model", *Journal of Engineering Mechanics*, Vol. 10, pp. 1061-1070, 2015.

32. Pianese, G., B. Petrovic, S. Parolai, and R. Paolucci, "Identification of the Nonlinear Seismic Response of Buildings by a Combined Stockwell Transform and Deconvolution Interferometry Approach", *Bulletin of Earthquake Engineering*, Vol. 16, No. 7, pp. 3103-3126, 2018.

33. Stockwell, R. G., L. Mansinha, and R. P. Lowe, "Localization of the Complex Spectrum: the S Transform", *IEEE transactions on signal processing*, Vol. 44, No. 4, pp. 998-1001, 1996.

34. Picozzi, M., S. Parolai, M. Mucciarelli, C. Milkereit, D. Bindi, R. Ditommaso, and J. Zschau, "Interferometric Analysis of Strong Ground Motion for Structural Health Monitoring: The Example of The L'Aquila, Italy, Seismic Sequence of 2009", *Bulletin of the Seismological Society of America*, Vol. 101, No. 2, pp. 635-651, 2011.

35. Boore, David M., "Effect of Baseline Corrections on Displacements and Response Spectra for Several Recordings of the 1999 Chi-Chi, Taiwan, Earthquake", *Bulletin of the Seismological Society of America*, Vol. 91, No. 5, pp. 1199-1211, 2001.

36. Iwan, Wilfred D., M. A. Moser, and C. Peng. "Some Observations On Strong-Motion Earthquake Measurement Using a Digital Accelerograph", *Bulletin of the Seismological Society of America*, Vol. 75, No. 5, pp.1225-1246, 1985.

37. Boore, David M. "Effect of Baseline Corrections on Displacements and Response Spectra for Several Recordings of the 1999 Chi-Chi, Taiwan, Earthquake", *Bulletin*

of the Seismological Society of America, 99-545, 37 pp, 1999.

38. Skolnik, D. A. and J. W. Wallace, "Critical Assessment of Interstory Drift Measurements", *Journal of Structural Engineering*, Vol. 136, No. 12, pp. 1574-1584, 2010.

39. American Society of Civil Engineers(ASCE), *7–16, Minimum Design Loads for Buildings and Other Structures, American Society of Civil Engineers*, Reston, Virginia, United States of America, 2017.

40. American Society of Civil Engineers(ASCE), *41-17, Seismic Evaluation and Retrofit of Existing Buildings, American Society of Civil Engineers Institute*, Structural Engineering, Reston, Virginia, United States of America, 2017.

41. Foreign Exchange Management Act (FEMA)-*450, Recommended Provisions for Seismic Regulations for New Buildings and Other Structures*, Federal Emergency Management Agency, Washington, DC, United States of America, 2003.

42. Boore, D. M., "Analog-To-Digital Conversion as a Source of Drifts in Displacements Derived from Digital Recordings of Ground Acceleration", *Bulletin of the Seismological Society of America*, Vol. 93, No. 5, pp. 2017-2024, 2003.

43. Lovse, J. W., W. F. Teskey, G. Lachapelle, and M. E. Cannon, "Dynamic Deformation Monitoring of Tall Structure Using GPS Technology", *Journal of Surveying Engineering*, Vol. 121, No. 1, pp. 35-40, 1995.

44. Celebi, M. and, A. Sanli, "GPS in Pioneering Dynamic Monitoring of Long-Period Structures", *Earthquake Spectra*, Vol. 18, No. 1, pp. 47-61, 2002.

45. Im, S. B., S. Hurlebaus, and Y. J. Kang, "Summary Review of GPS Technology for Structural Health Monitoring", *Journal of Structural Engineering*, Vol. 139, No. 10, pp. 1653-1664, 2013.

46. Şafak, E. and E. Çaktı, "Simple Techniques to Analyze Vibration Records from Buildings", *In Proceedings of the Seventh European Workshop on Structural Health Monitoring*, Nantes, France, 2014.

47. Savitzky, A. and Marcel JE Golay, "Smoothing and Differentiation of Data by Simplified Least Squares Procedures", *Analytical Chemistry*, Vol. 36, No. 8, pp. 1627-1639, 1964.

48. MATLAB, "Version R2022a", Natick, Massachusetts: MathWorks Inc., 2022.

49. Belarbi, A. and T. C. Hsu, "Constitutive Laws of Concrete in Tension and Reinforcing Bars Stiffened by Concrete", *Structural Journal*, Vol. 91, No. 4, pp. 465-474, 1994.

50. Computers and Structures, Inc (CSI), PERFORM-3D, Software, Berkeley, CA.

51. Database, P.S.M., "Pacific Earthquake Engineering Research Center", 2022, https:// ngawest2. berkeley. edu/, accessed on May 21, 2022.

52. Mander, J. B., M. J. Priestley, and R. Park, "Theoretical Stress-Strain Model for Confined Concrete", *Journal of Structural Engineering*, Vol. 114, No. 8, pp. 1804-1826, 1988.

53. Menegotto, M., "Method of Analysis for Cyclically Loaded Rc Frames Including Changes in Geometry and Non-Elastic Behaviour of Elements Under Conbined Normal Force and Bending", *In IABSE Congress Reports of the Working Commission*, Lisboa, 1973.

54. Mander, John B., F.D. Panthaki, and A. Kasalanati, "Low-Cycle Fatigue Behavior of Reinforcing Steel", *Journal of Materials in Civil Engineering*, No. 4, pp. 453-468, 1994.

55. Lowes, Laura N., Dawn E. Lehman, C. Baker, and C. P. Lundeen, "Recommenda-

tions for Modeling the Nonlinear Response of Slender Reinforced Concrete Walls Using PERFORM-3D", *In 2016 SEAOC Convention*, Maui, USA. 2016.

56. Beyer, Katrin, A. Dazio, and N. Priestley, "Shear Deformations of Slender Reinforced Concrete Walls Under Seismic Loading", *ACI Structural Journal 108. Article*, Vol. 1, pp. 167-177, 2011.

APPENDIX A: ANALYSIS RESULTS FOR THE BUILDINGS

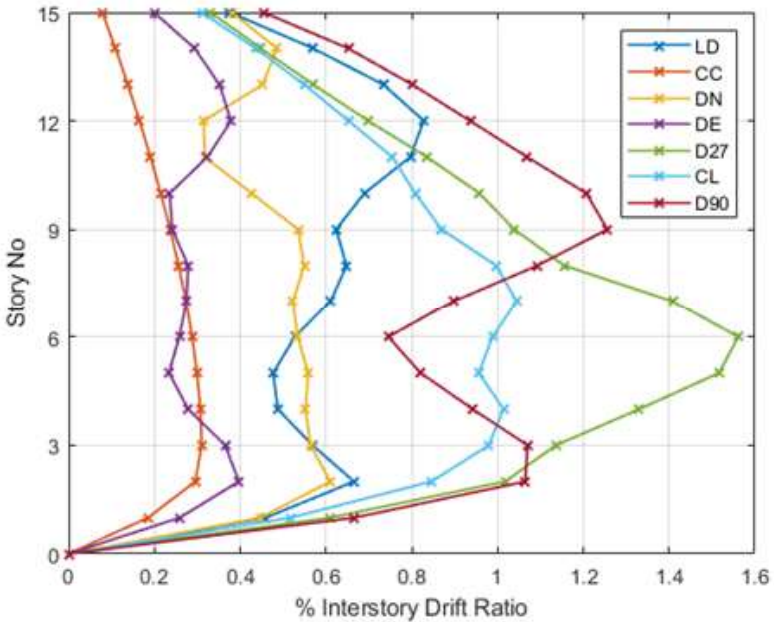

Figure A.1. The interstory drift ratios for Fr15A under all earthquake excitations.

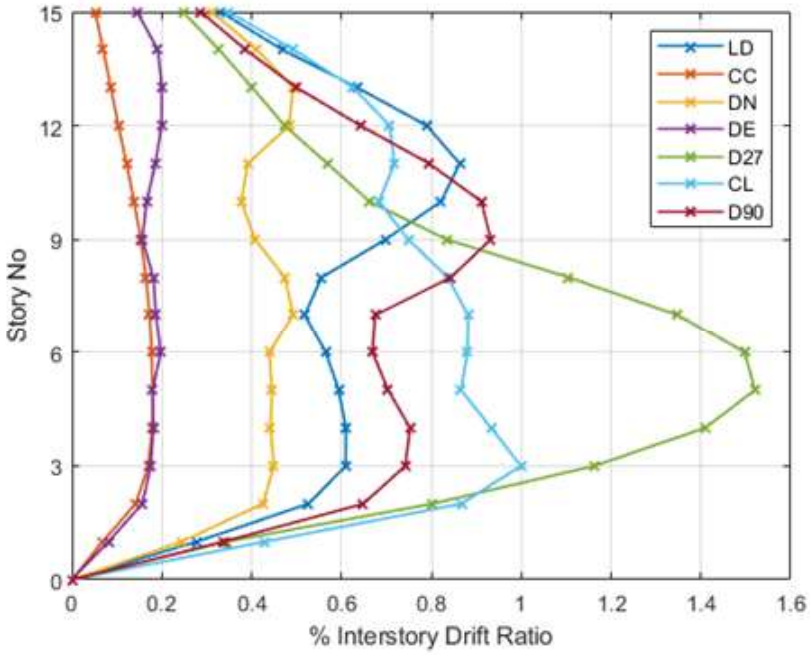

Figure A.2. The interstory drift ratios for Fr15B under all earthquake excitations.

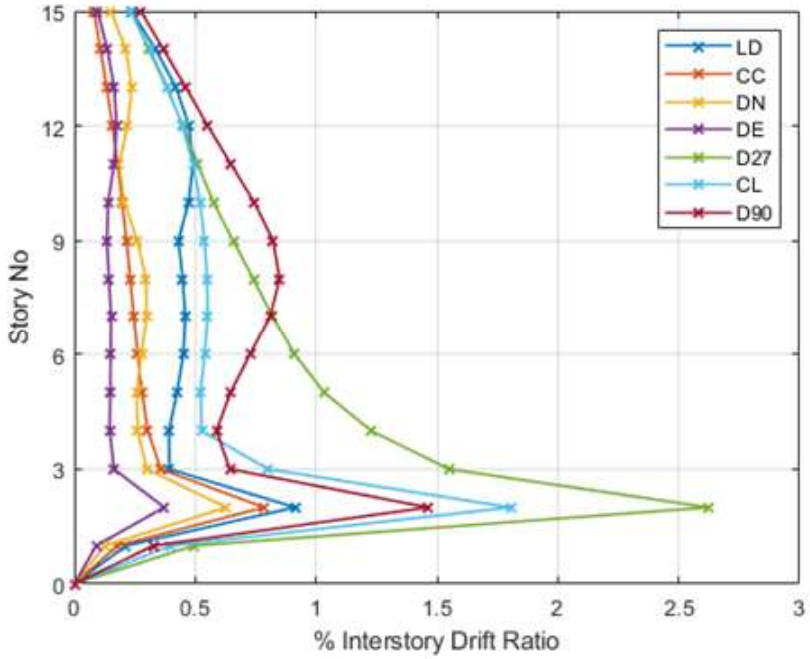

Figure A.3. The interstory drift ratios for Fr15C under all earthquake excitations.

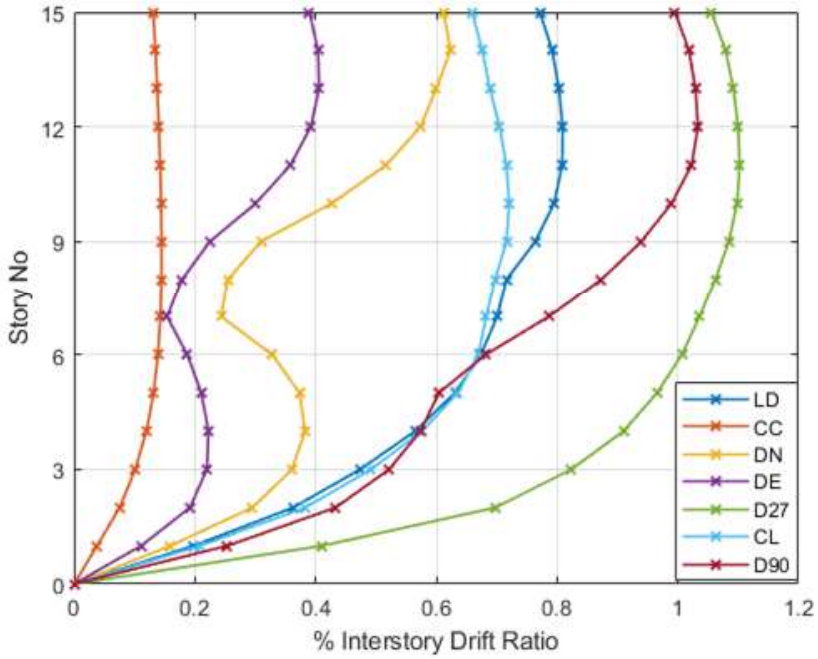

Figure A.4. The interstory drift ratios for D15 under all earthquake excitations.

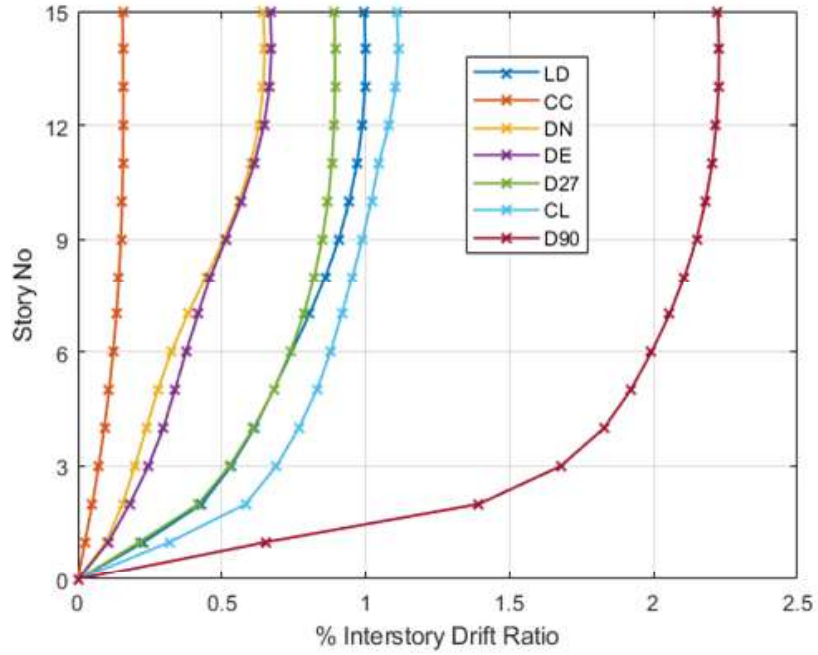

Figure A.5. The interstory drift ratios for W15 under all earthquake excitations (the earthquakes are scaled with 2.5).

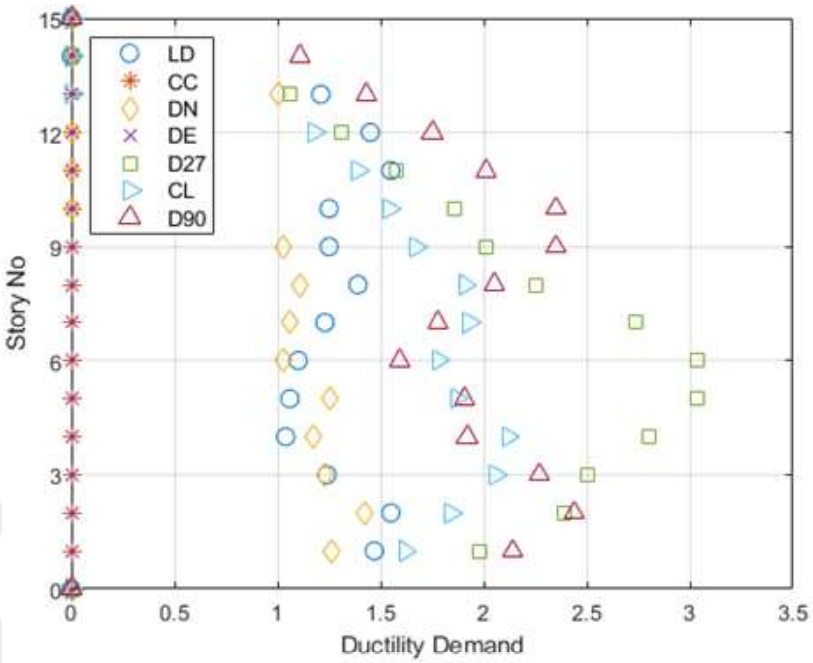

Figure A.6. The ductility demand values for Fr15A under all earthquake excitations.

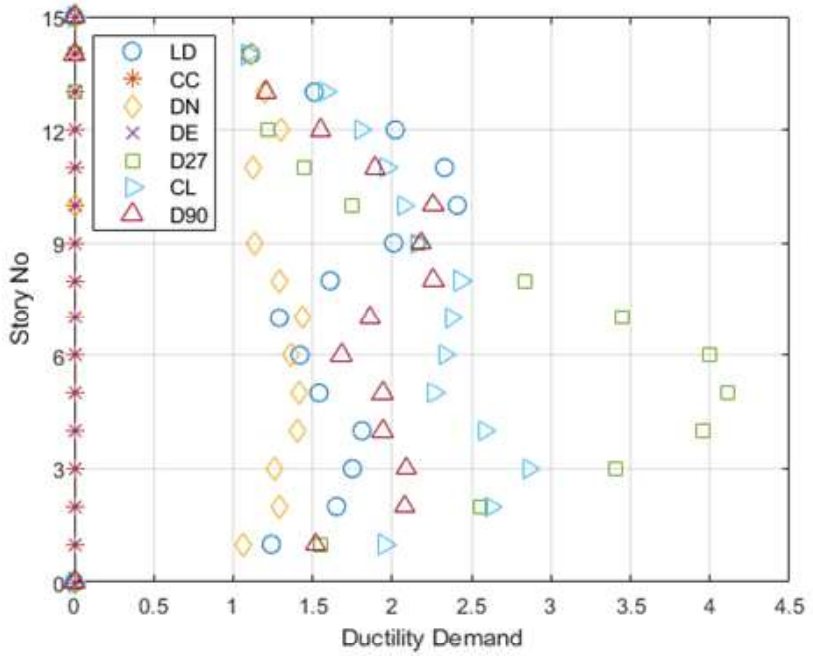

Figure A.7. The ductility demand values for Fr15B under all earthquake excitations.

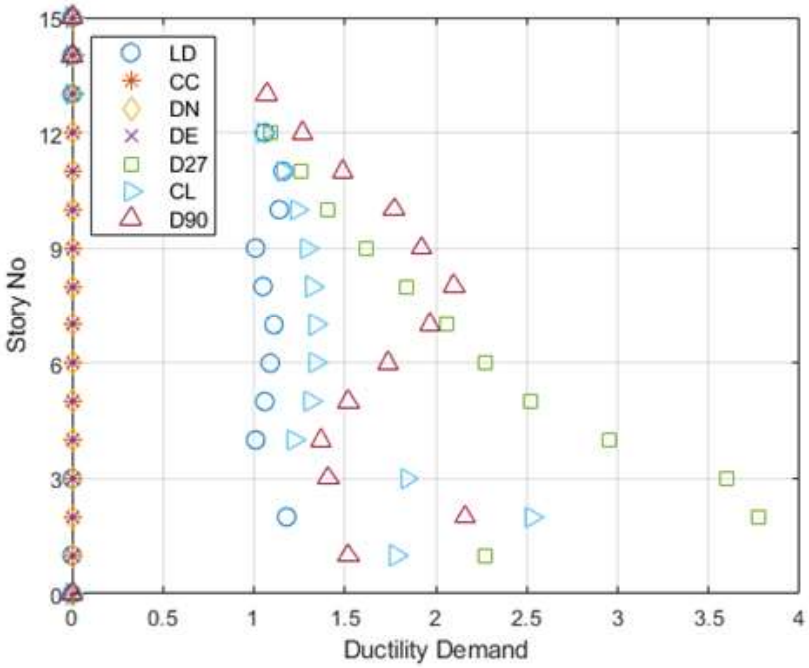

Figure A.8. The ductility demand values for Fr15C under all earthquake excitations.

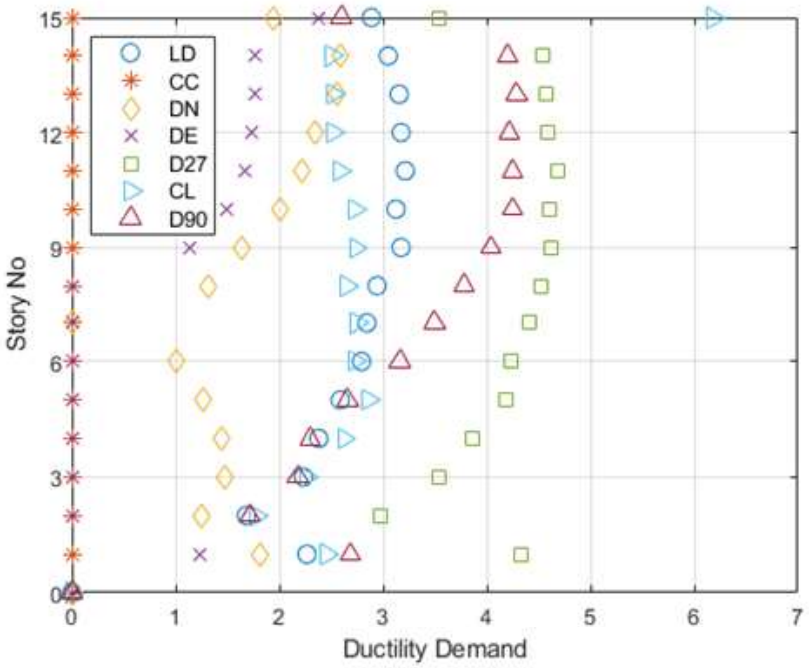

Figure A.9. The ductility demand values for D15 under all earthquake excitations.

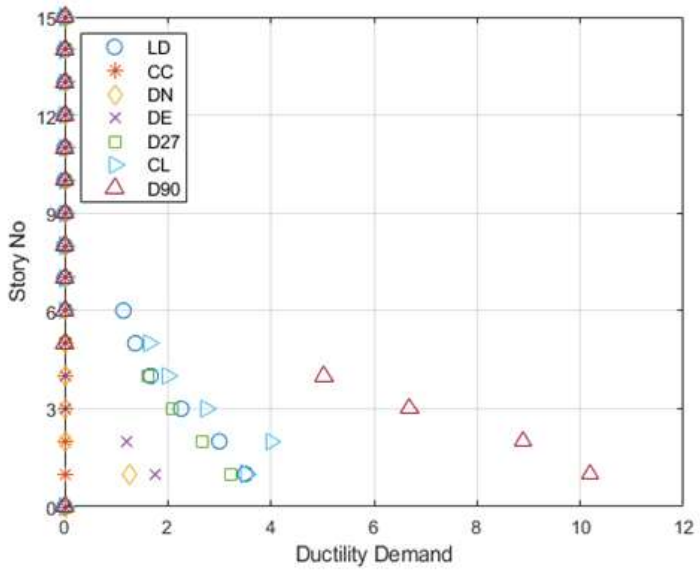

Figure A.10. The story ductility demand values for W15 under all earthquake excitations (the earthquakes are scaled with 2.5)..

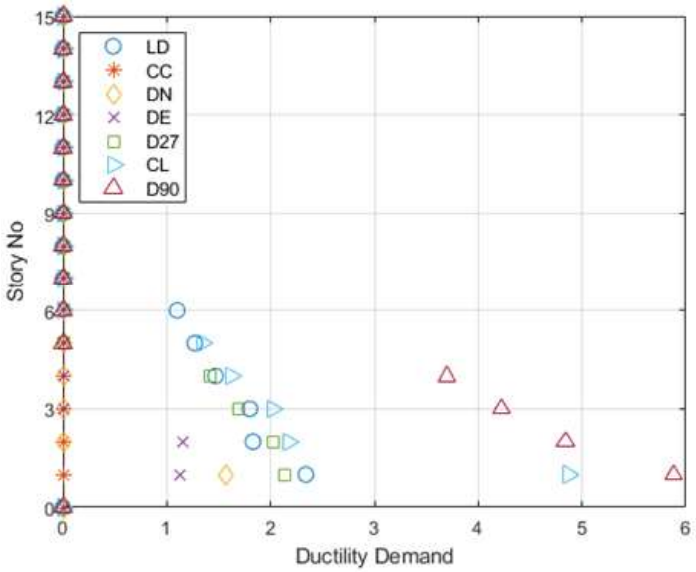

Figure A.11. The roof ductility demand values for W15 under all earthquake excitations (the earthquakes are scaled with 2.5).

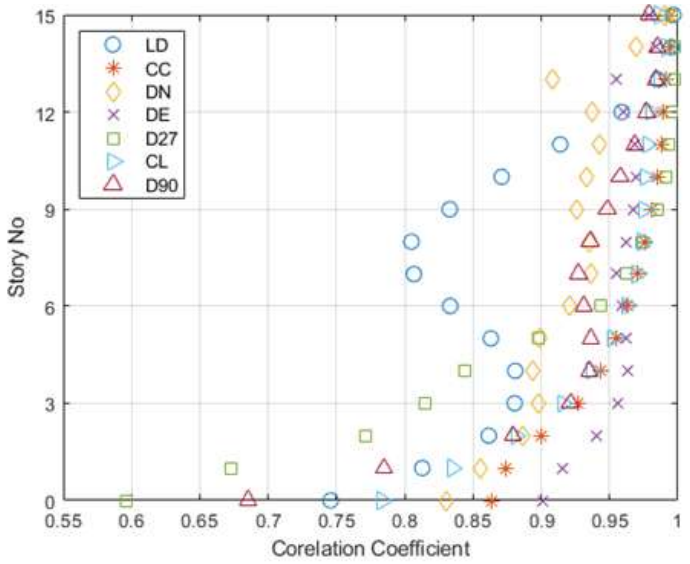

Figure A.12. Story-wise correlation coefficients between the actual and convolved waves with respect to top of the Fr15A.

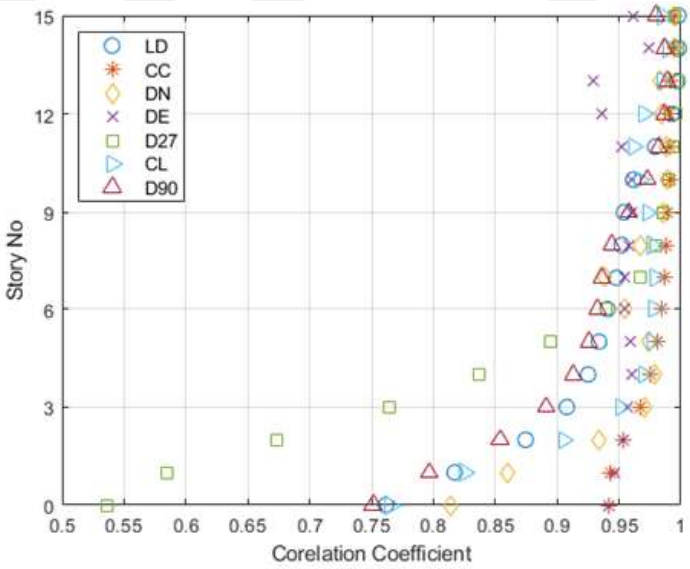

Figure A.13. Story-wise correlation coefficients between the actual and convolved waves with respect to top of the Fr15B.

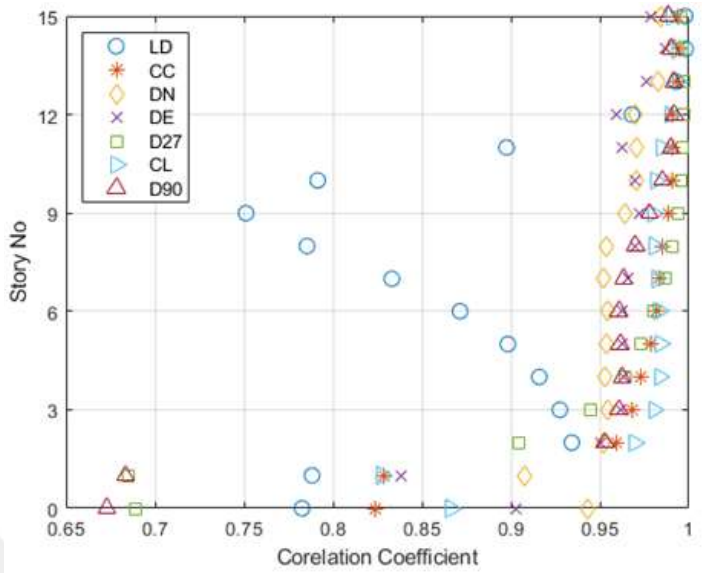

Figure A.14. Story-wise correlation coefficients between the actual and convolved waves with respect to top of the Fr15C.

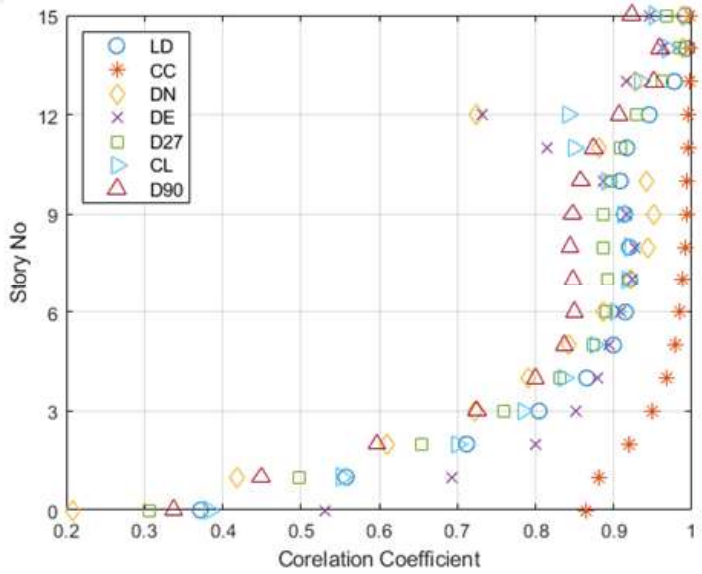

Figure A.15. Story-wise correlation coefficients between the actual and convolved waves with respect to top of the D15.

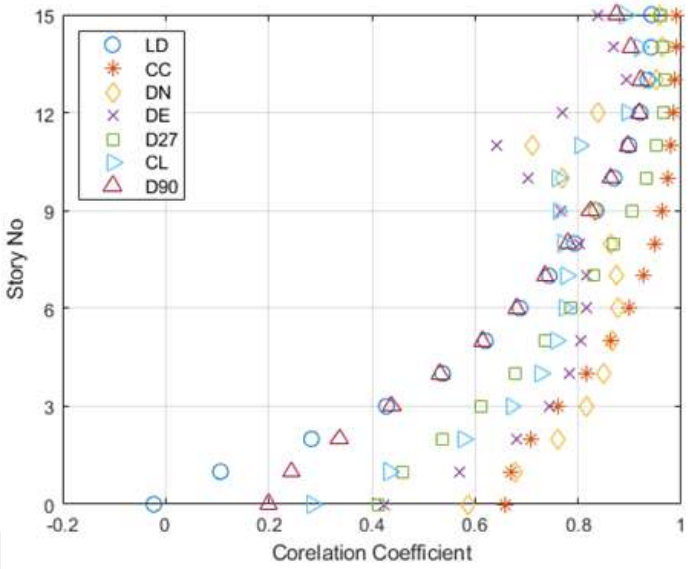

Figure A.16. Story-wise correlation coefficients between the actual and convolved waves with respect to top of the W15 (the earthquakes are scaled with 2.5).

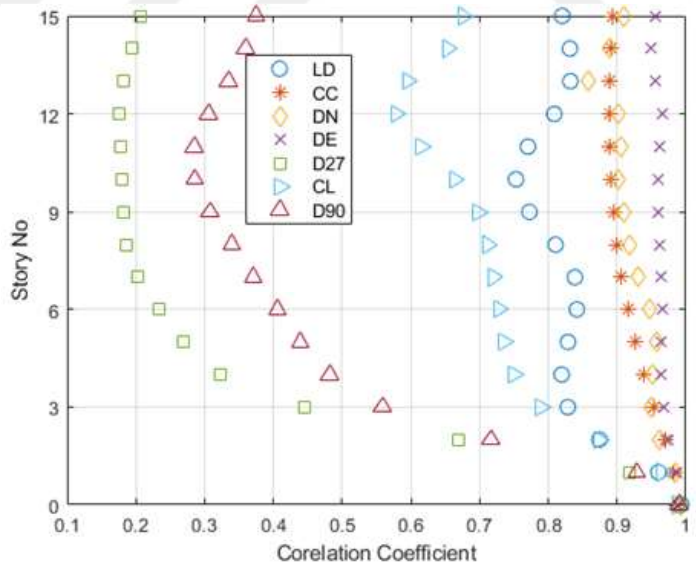

Figure A.17. Story-wise correlation coefficients between the actual and convolved waves with respect to base of the Fr15A.

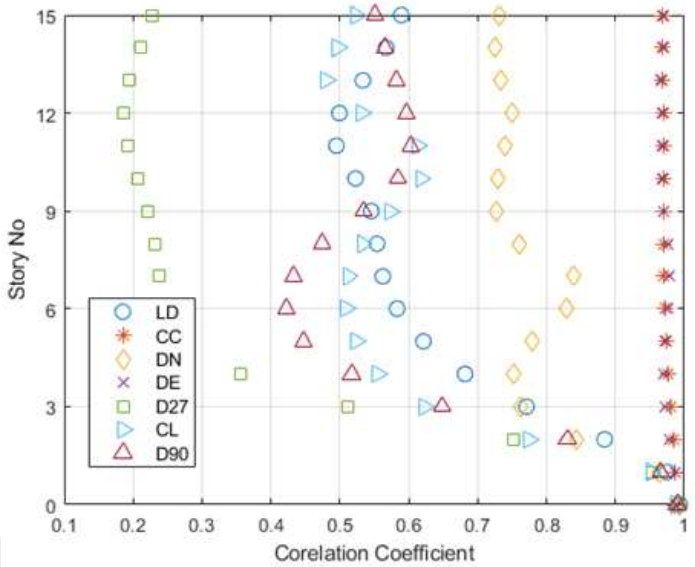

Figure A.18. Story-wise correlation coefficients between the actual and convolved waves with respect to base of the Fr15B.

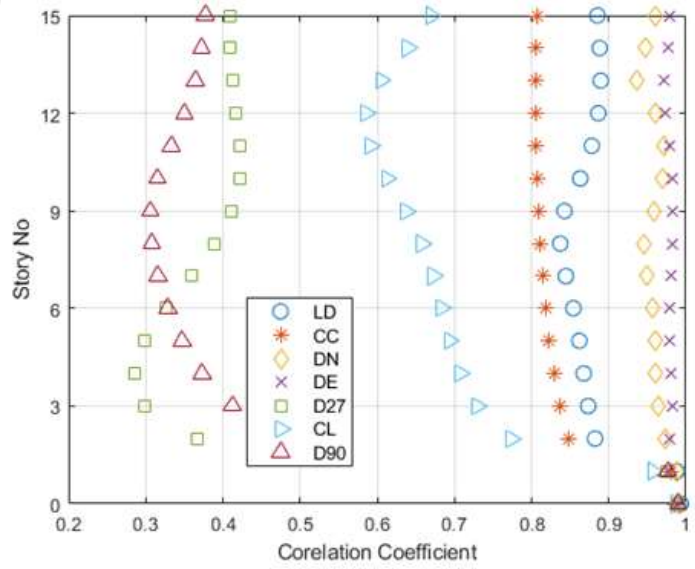

Figure A.19. Story-wise correlation coefficients between the actual and convolved waves with respect to base of the Fr15C.

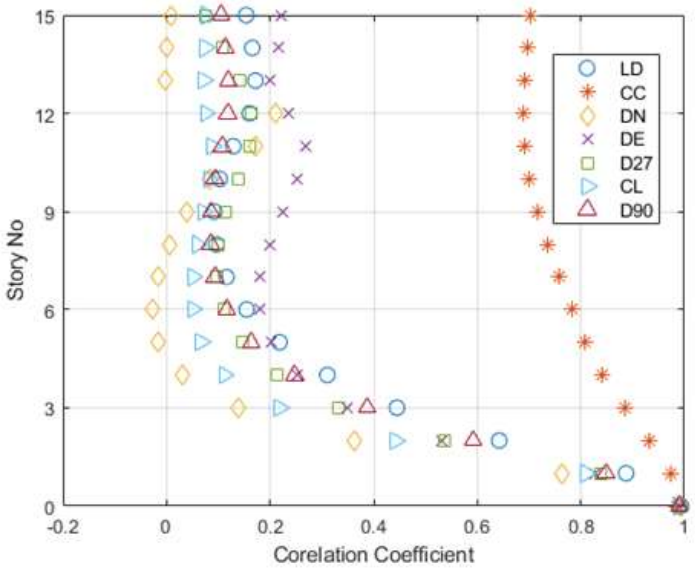

Figure A.20. Story-wise correlation coefficients between the actual and convolved waves with respect to base of the D15.

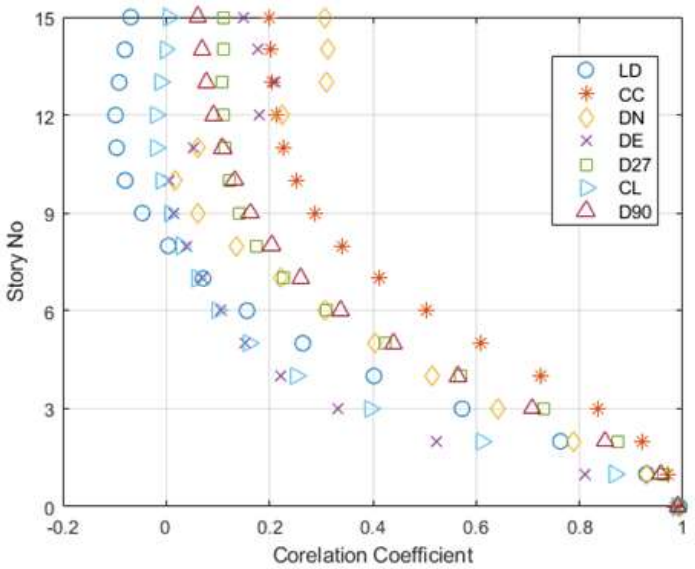

Figure A.21. Story-wise correlation coefficients between the actual and convolved waves with respect to base of the W15 (the earthquakes are scaled with 2.5).

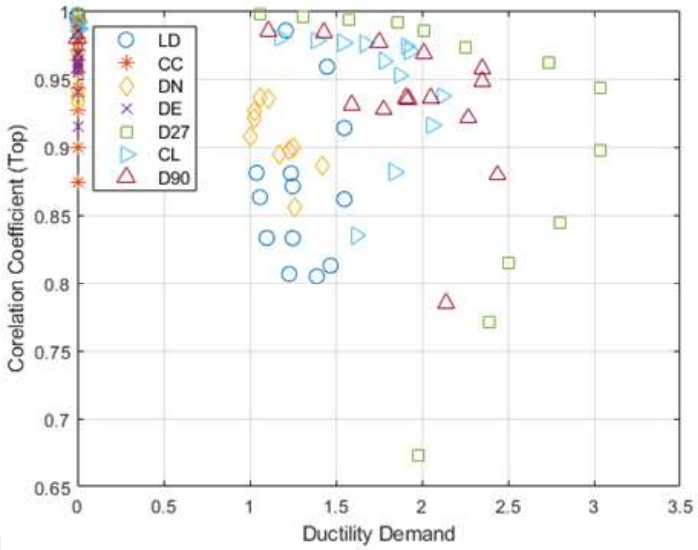

Figure A.22. Correlation coefficients between the actual and convolved waves with respect to top for Fr15A.

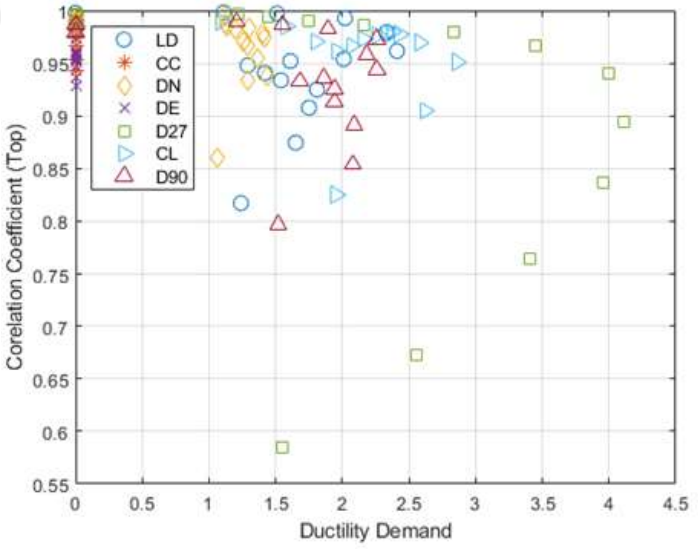

Figure A.23. Correlation coefficients between the actual and convolved waves with respect to top vs the ductility demand for Fr15B.

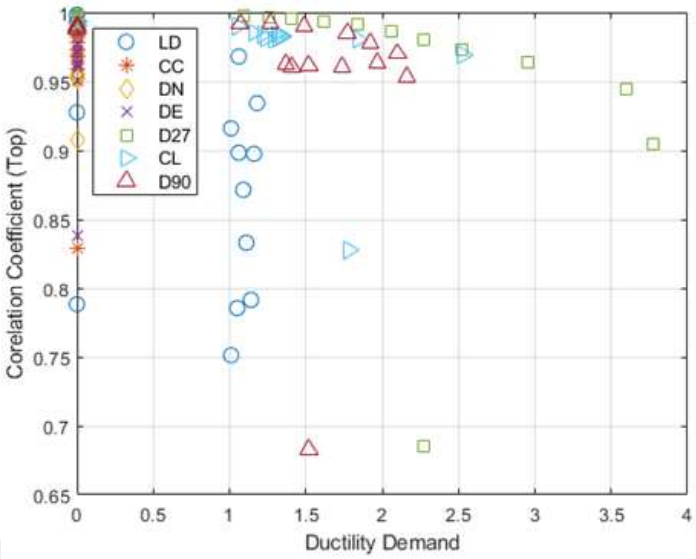

Figure A.24. Correlation coefficients between the actual and convolved waves with respect to top vs the ductility demand for Fr15C.

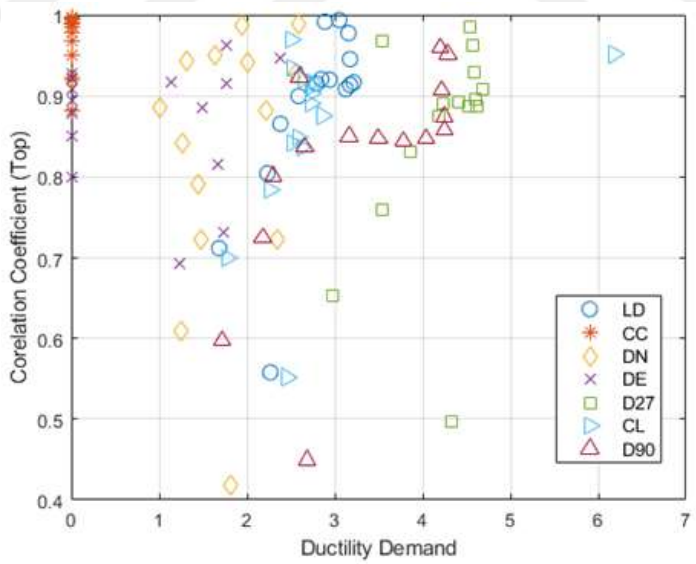

Figure A.25. Correlation coefficients between the actual and convolved waves with respect to top vs the ductility demand for D15.

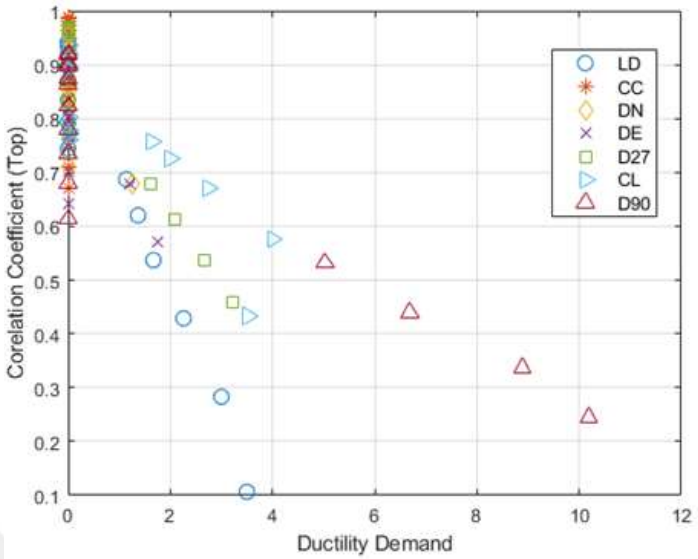

Figure A.26. Correlation coefficients between the actual and convolved waves with respect to top vs the story ductility demand for W15 (the earthquakes are scaled with 2.5).

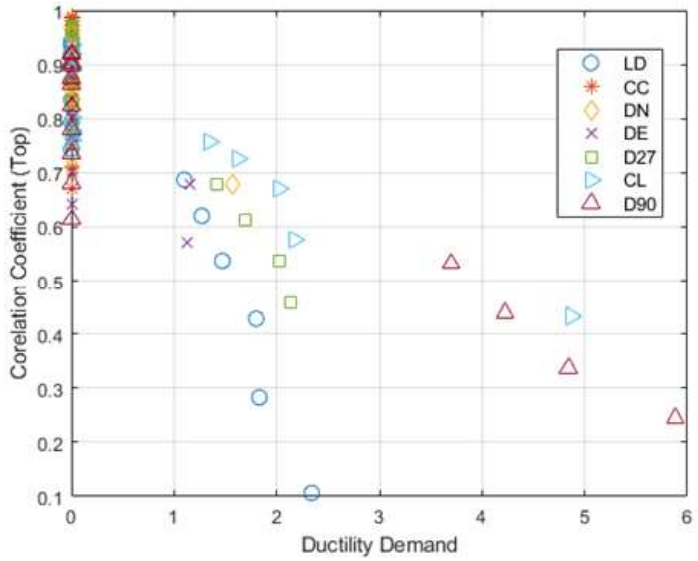

Figure A.27. Correlation coefficients between the actual and convolved waves with respect to top vs the roof ductility demand for W15 (the earthquakes are scaled with 2.5).

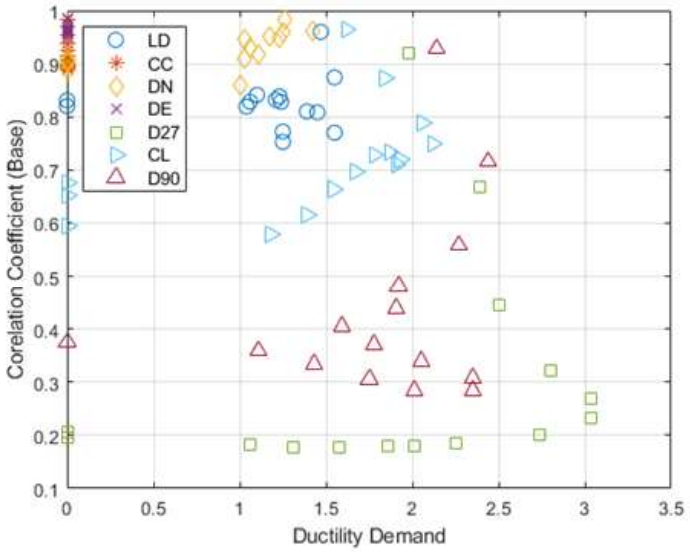

Figure A.28. Correlation coefficients between the actual and convolved waves with respect to base vs ductility demand for Fr15A.

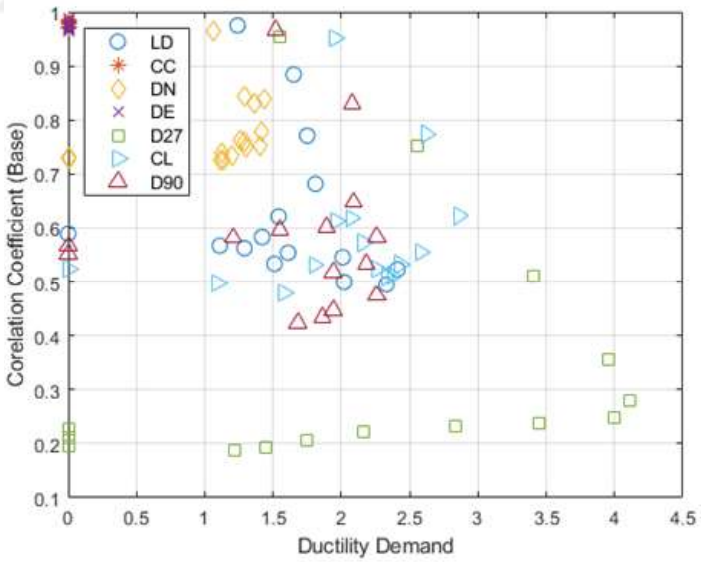

Figure A.29. Correlation coefficients between the actual and convolved waves with respect to base vs ductility demand for Fr15B.

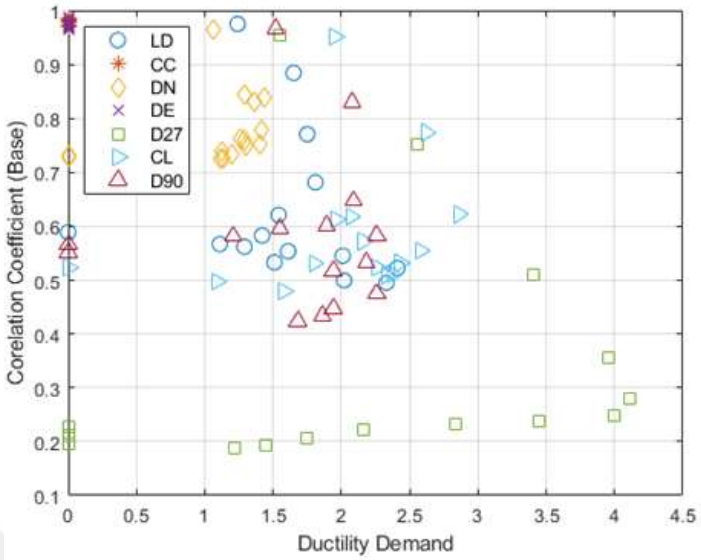

Figure A.30. Correlation coefficients between the actual and convolved waves with respect to base vs ductility demand for Fr15C.

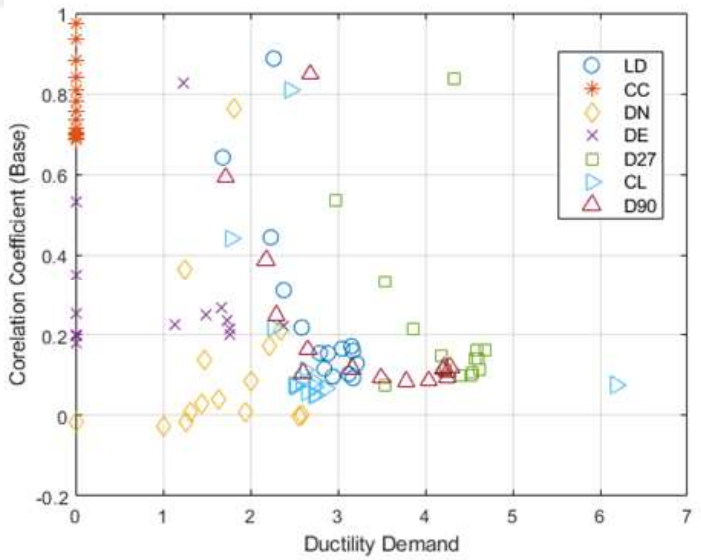

Figure A.31. Correlation coefficients between the actual and convolved waves with respect to base vs ductility demand for D15.

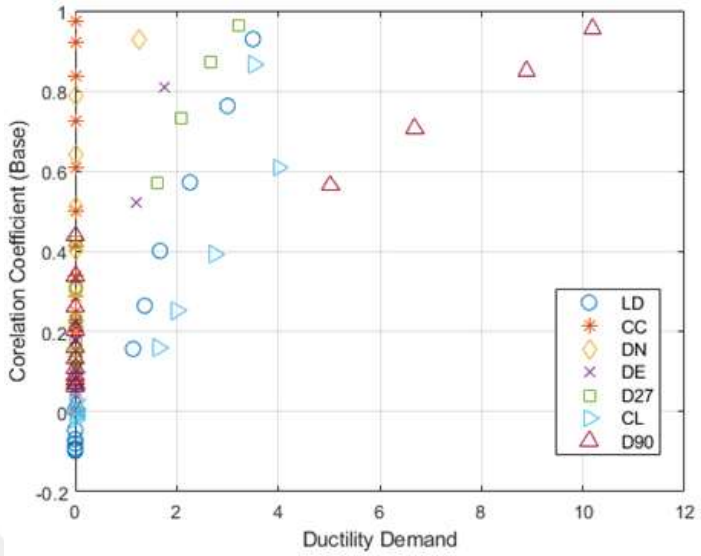

Figure A.32. Correlation coefficients between the actual and convolved waves with respect to base vs the story ductility demand for W15 (the earthquakes are scaled with 2.5).

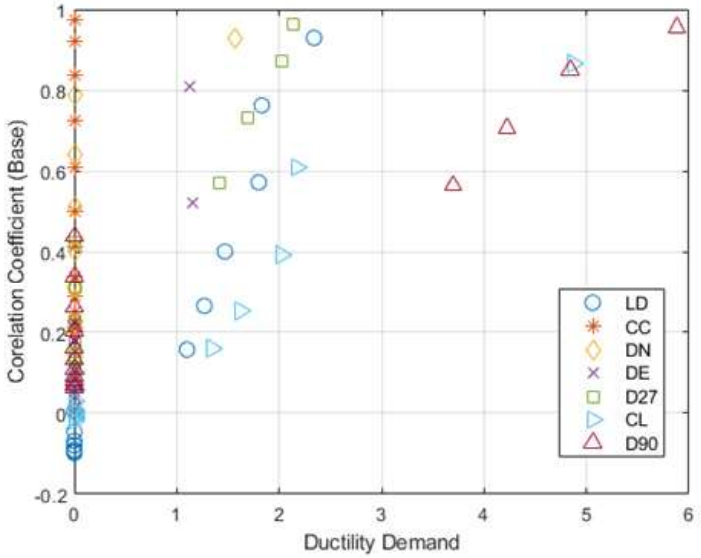

Figure A.33. Correlation coefficients between the actual and convolved waves with respect to base vs the roof ductility demand for W15 (the earthquakes are scaled with 2.5).

APPENDIX B: INTERNAL COLUMN FORCES ESTIMATED BY THE METHOD 2

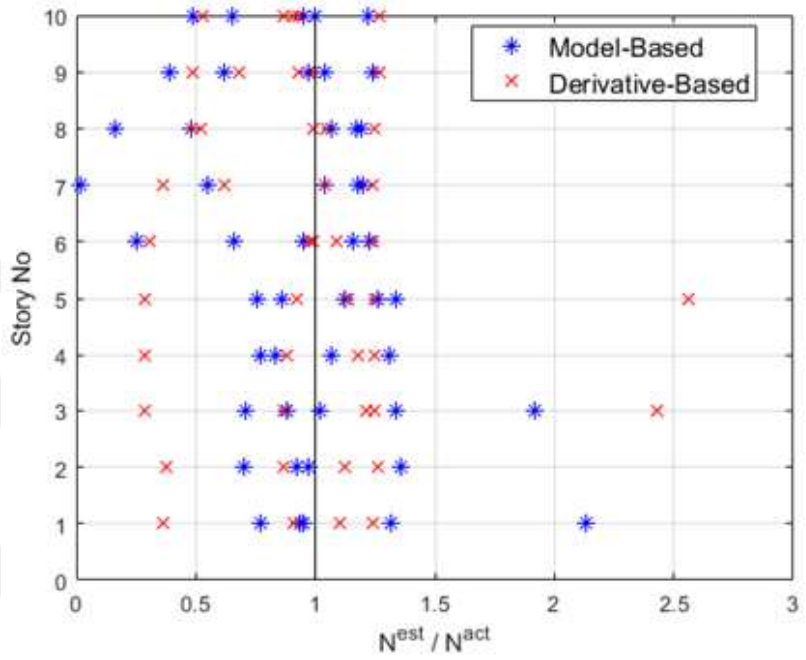

Figure B.1. Ratio of the estimated / actual axial forces for the columns of Fr10A given per story.

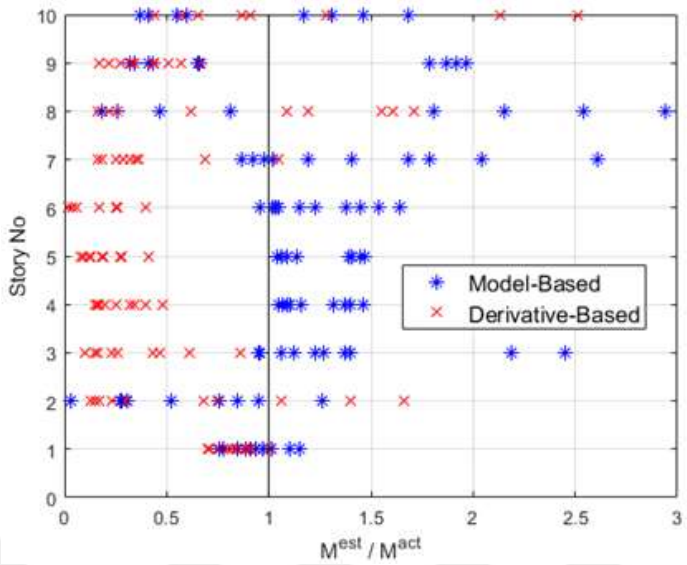

Figure B.2. Ratio of the estimated / actual column end moments of Fr10A given per story.

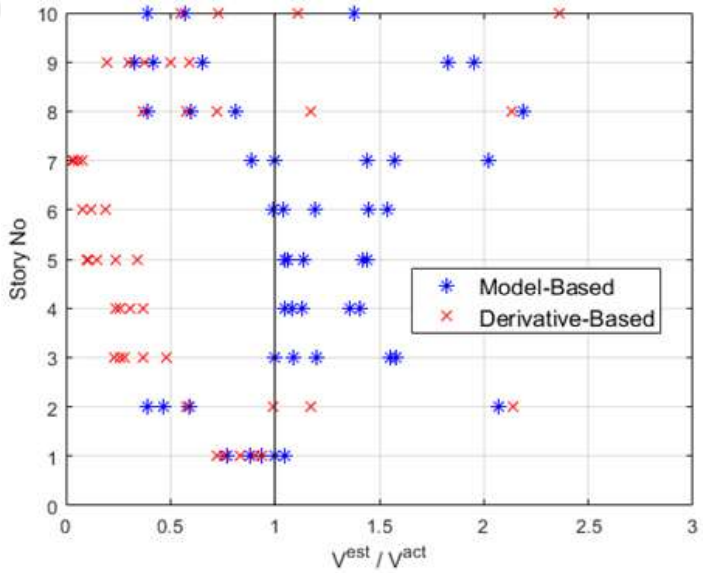

Figure B.3. Ratio of the estimated / actual column shear forces of Fr10A given per story.

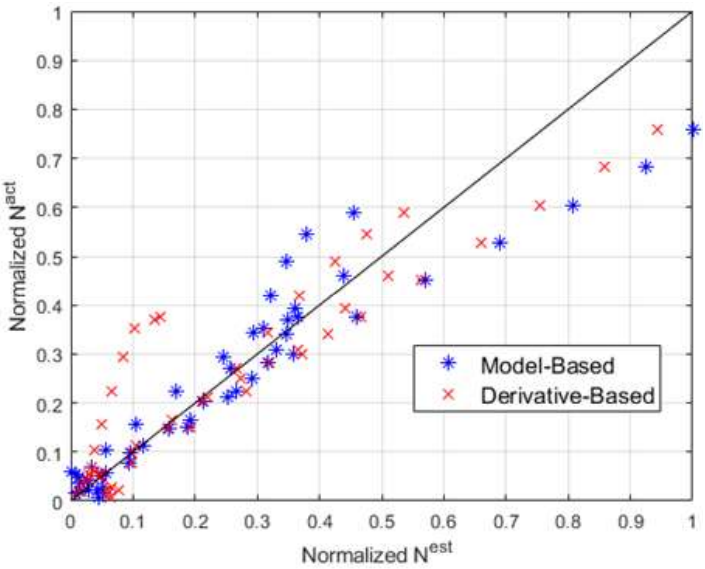

Figure B.4. Ratio of the estimated / actual normalized axial forces for all of the columns of Fr10A.

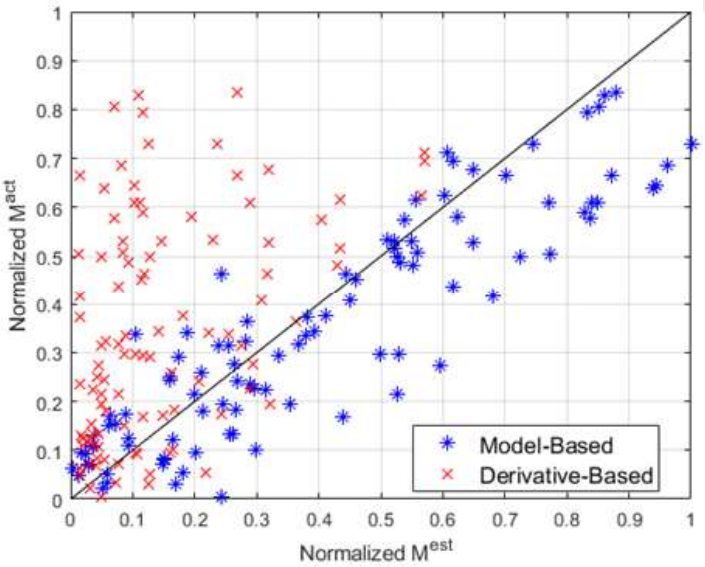

Figure B.5. Ratio of the estimated / actual normalized end moments for all of the columns of Fr10A.

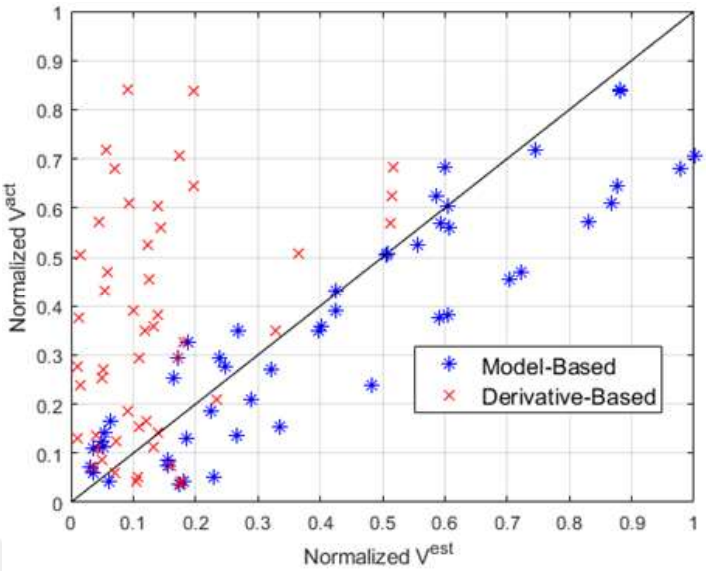

Figure B.6. Ratio of the estimated / actual normalized shear forces for all of the columns of Fr10A.

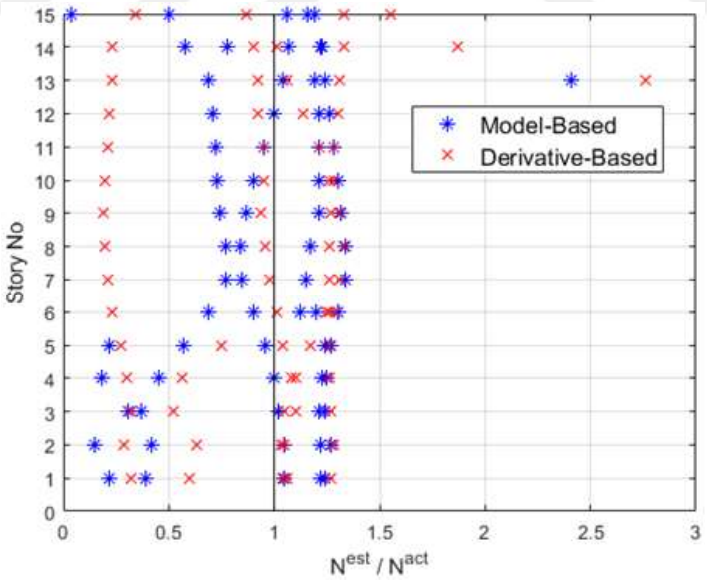

Figure B.7. Ratio of the estimated / actual axial forces for the columns of Fr15A given per story.

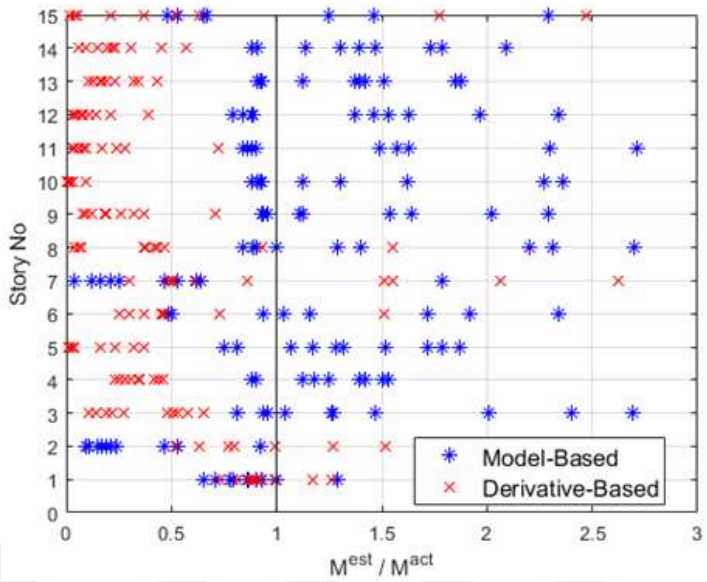

Figure B.8. Ratio of the estimated / actual column end moments of Fr15A given per story.

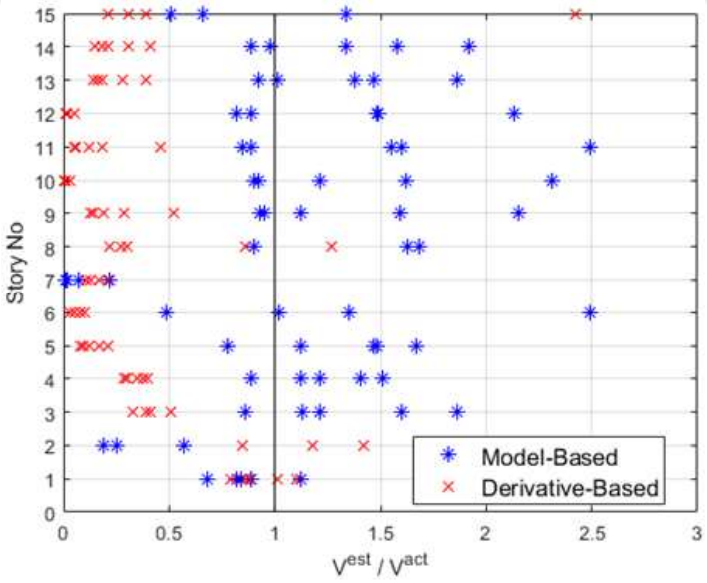

Figure B.9. Ratio of the estimated / actual column shear forces of Fr15A given per story.

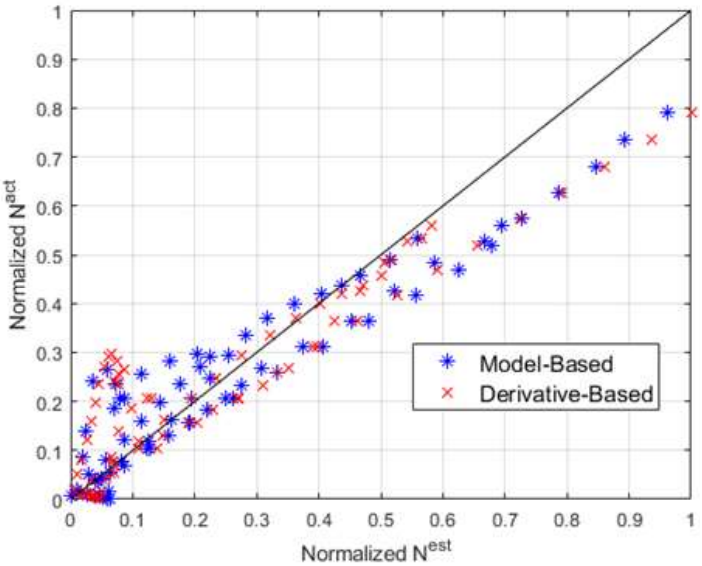

Figure B.10. Ratio of the estimated / actual normalized axial forces for all of the columns of Fr15A.

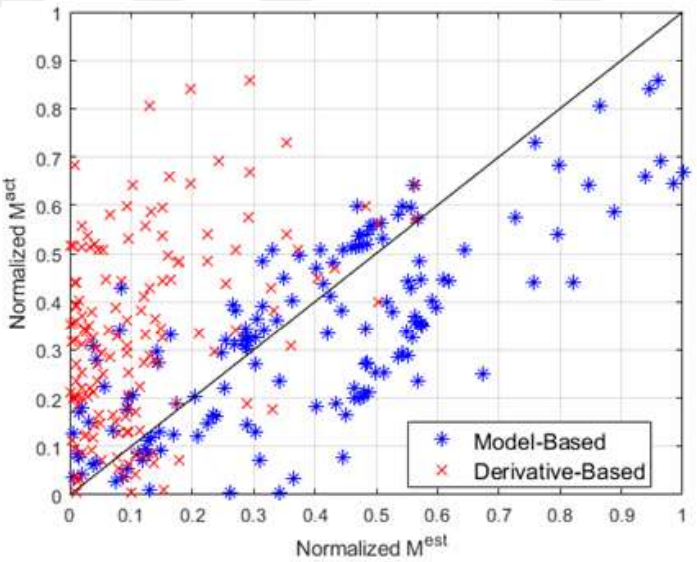

Figure B.11. Ratio of the estimated / actual normalized end moments for all of the columns of Fr15A.

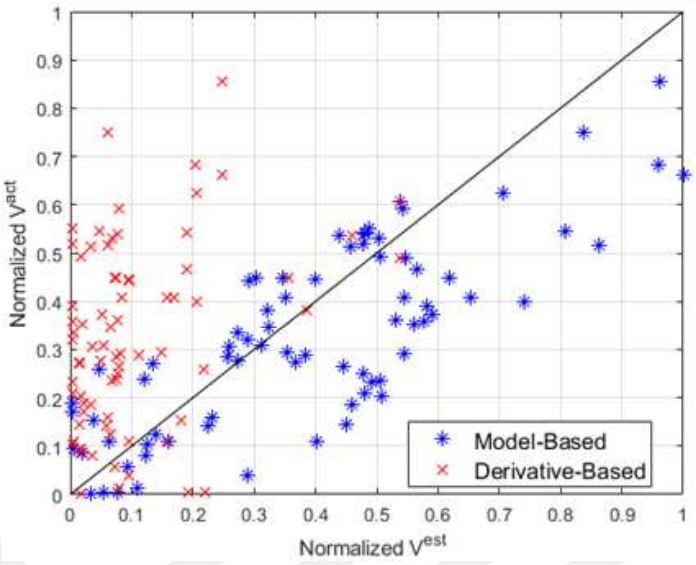

Figure B.12. Ratio of the estimated / actual normalized shear forces for all of the columns of Fr15A.

APPENDIX C: INTERNAL COLUMN FORCES ESTIMATED BY THE METHOD 2 FROM A NOISY DATA

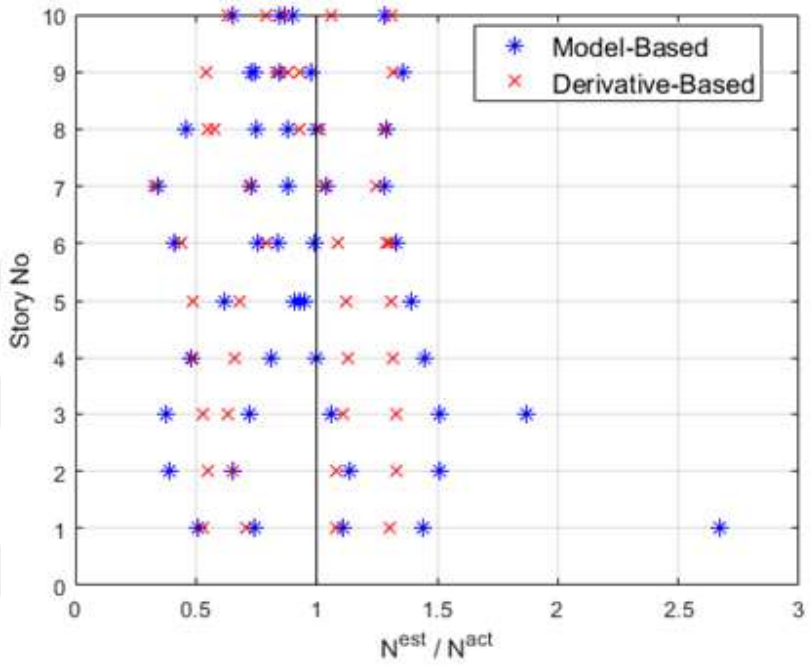

Figure C.1. Ratio of the estimated / actual axial forces for the columns of Fr10A given per story.

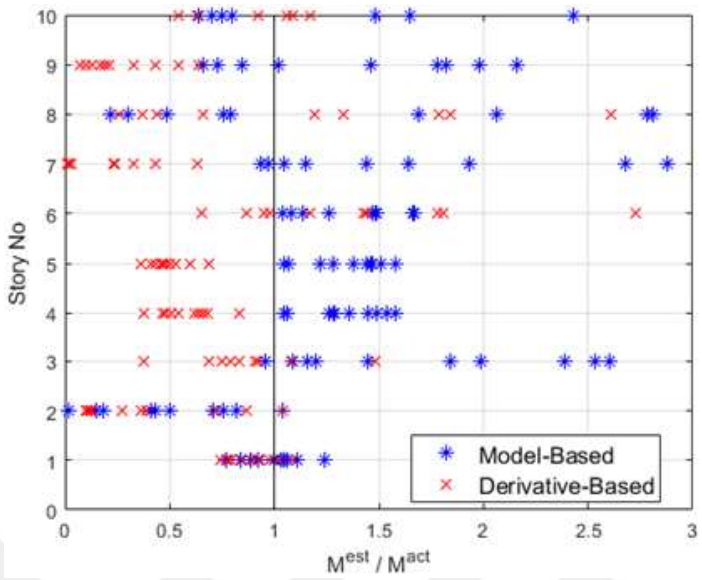

Figure C.2. Ratio of the estimated / actual column end moments of Fr10A given per story.

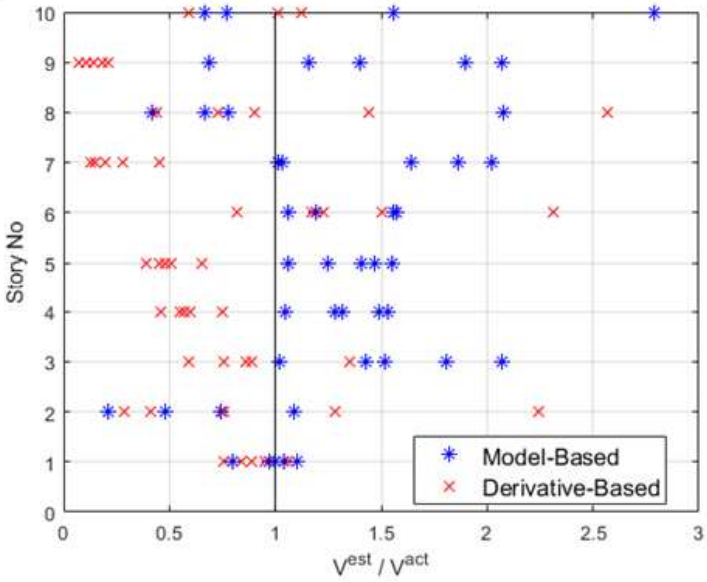

Figure C.3. Ratio of the estimated / actual column shear forces of Fr10A given per story.

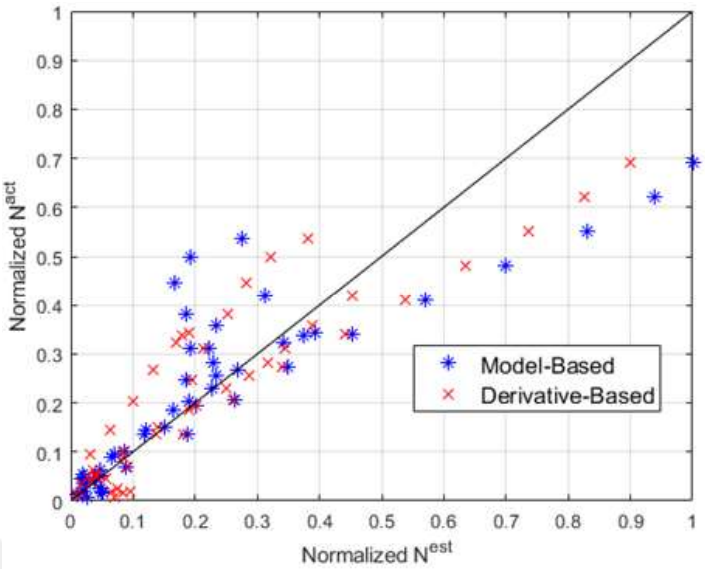

Figure C.4. Ratio of the estimated / actual normalized axial forces for all of the columns of Fr10A.

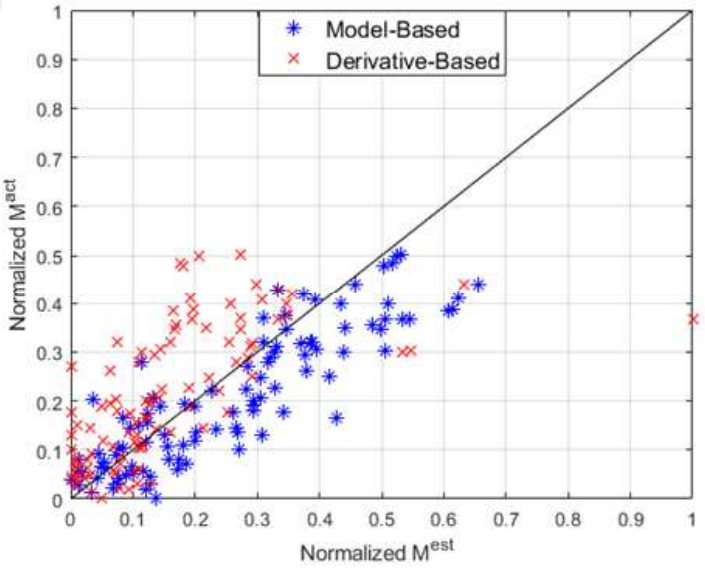

Figure C.5. Ratio of the estimated / actual normalized end moments for all of the columns of Fr10A.

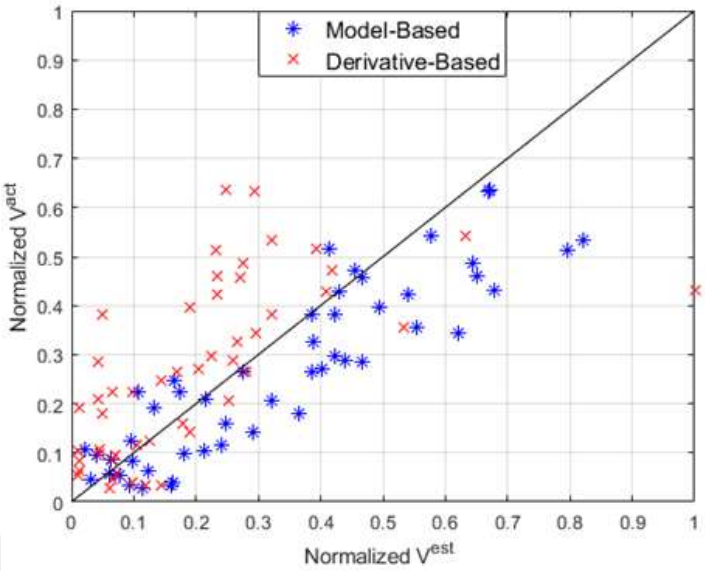

Figure C.6. Ratio of the estimated / actual normalized shear forces for all of the columns of Fr10A.

APPENDIX D: PERMISSIONS FOR THE FIGURES IN THE LITERATURE REVIEW SECTION

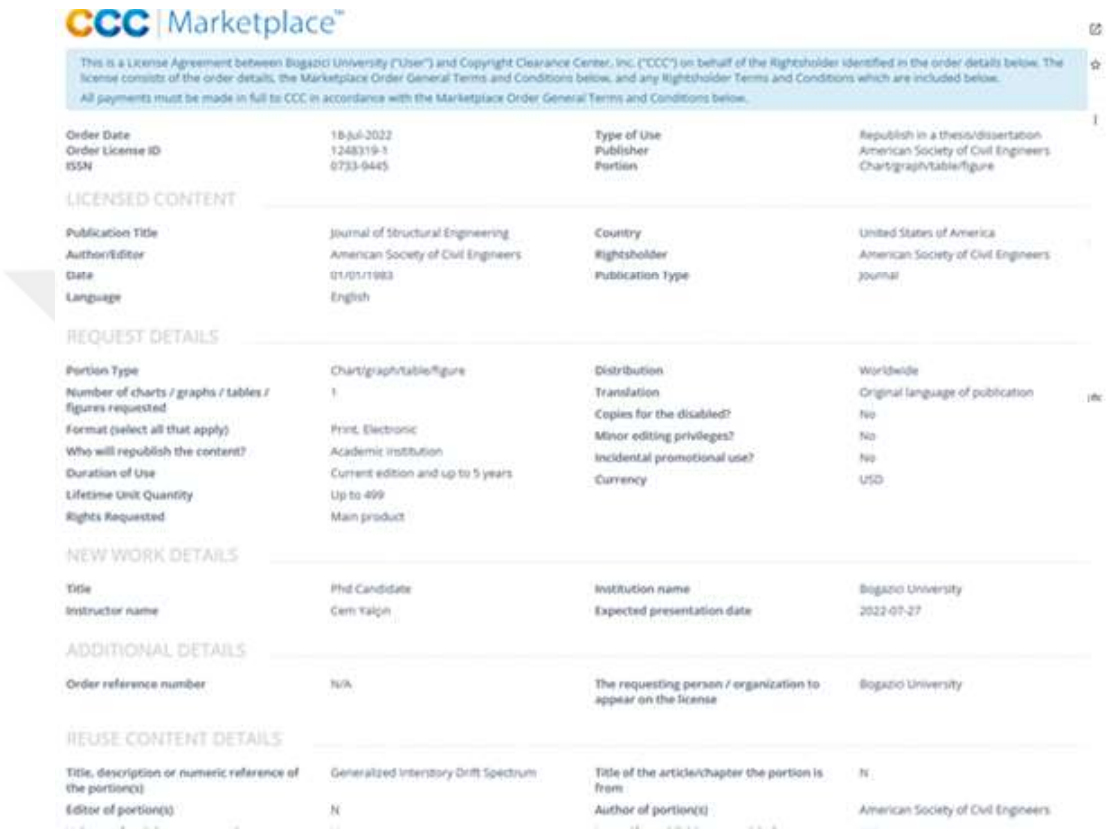

CCC | Marketplace™

This is a License Agreement between Bogazici University ("User") and Copyright Clearance Center, Inc. ("CCC") on behalf of the Rightsholder identified in the order details below. The license consists of the order details, the Marketplace Order General Terms and Conditions below, and any Rightsholder Terms and Conditions which are included below.

All payments must be made in full to CCC in accordance with the Marketplace Order General Terms and Conditions below.

Order Date	18-Jul-2022	Type of Use	Republish in a thesis/dissertation
Order License ID	1248319-1	Publisher	American Society of Civil Engineers
ISSN	0733-9445	Portion	Chart/graph/table/figure

LICENSED CONTENT

Publication Title	Journal of Structural Engineering	Country	United States of America
Author/Editor	American Society of Civil Engineers	Rightsholder	American Society of Civil Engineers
Date	01/01/1983	Publication Type	Journal
Language	English		

REQUEST DETAILS

Portion Type	Chart/graph/table/figure	Distribution	Worldwide
Number of charts / graphs / tables / figures requested	1	Translation	Original language of publication
Format (select all that apply)	Print, Electronic	Copies for the disabled?	No
Who will republish the content?	Academic institution	Minor editing privileges?	No
Duration of Use	Current edition and up to 5 years	Incidental promotional use?	No
Lifetime Unit Quantity	Up to 499	Currency	USD
Rights Requested	Main product		

NEW WORK DETAILS

Title	Phd Candidate	Institution name	Bogazici University
Instructor name	Cem Yalçın	Expected presentation date	2022-07-27

ADDITIONAL DETAILS

Order reference number	N/A	The requesting person / organization to appear on the license	Bogazici University

REUSE CONTENT DETAILS

Title, description or numeric reference of the portion(s)	Generalized Interstory Drift Spectrum	Title of the article/chapter the portion is from	N
Editor of portion(s)	N	Author of portion(s)	American Society of Civil Engineers

Figure D.1. Permission-1.

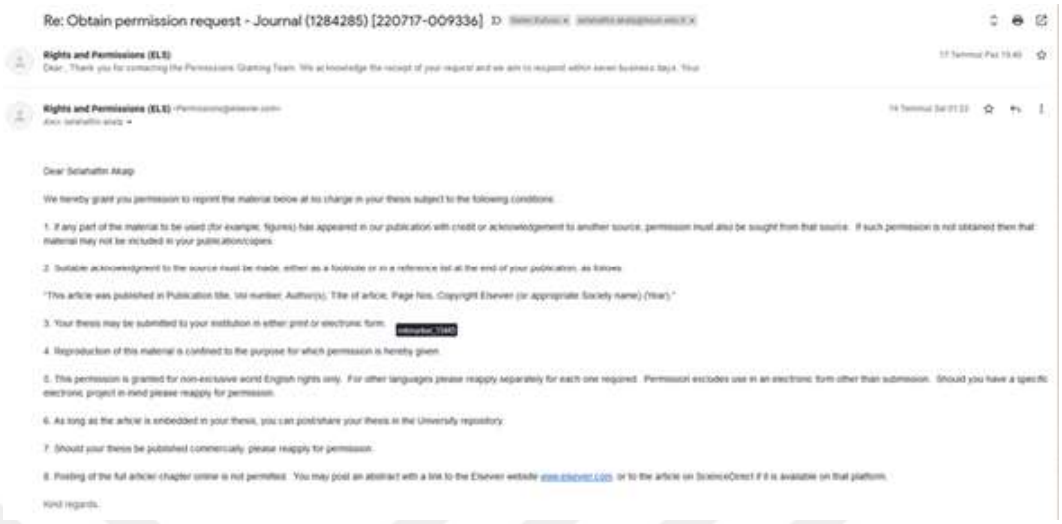

Re: Obtain permission request - Journal (1284285) [220717-009336]

Rights and Permissions (ELS)

Dear , Thank you for contacting the Permissions Granting Team. We acknowledge the receipt of your request and we aim to respond within seven business days. Your

Rights and Permissions (ELS)

Dear Selahattin Akalp

We hereby grant you permission to reprint the material below at no charge in your thesis subject to the following conditions.

1. If any part of the material to be used (for example, figures) has appeared in our publication with credit or acknowledgement to another source, permission must also be sought from that source. If such permission is not obtained then that material may not be included in your publication/copies.

2. Suitable acknowledgment to the source must be made, either as a footnote or in a reference list at the end of your publication, as follows:

"This article was published in Publication title, Vol number, Author(s), Title of article, Page Nos, Copyright Elsevier (or appropriate Society name) (Year)."

3. Your thesis may be submitted to your institution in either print or electronic form.

4. Reproduction of this material is confined to the purpose for which permission is hereby given.

5. This permission is granted for non-exclusive world English rights only. For other languages please reapply separately for each one required. Permission excludes use in an electronic form other than submission. Should you have a specific electronic project in mind please reapply for permission.

6. As long as the article is embedded in your thesis, you can post/share your thesis in the University repository.

7. Should your thesis be published commercially, please reapply for permission.

8. Posting of the full article/ chapter online is not permitted. You may post an abstract with a link to the Elsevier website www.elsevier.com, or to the article on ScienceDirect if it is available on that platform.

Kind regards,

Figure D.2. Permission-2.

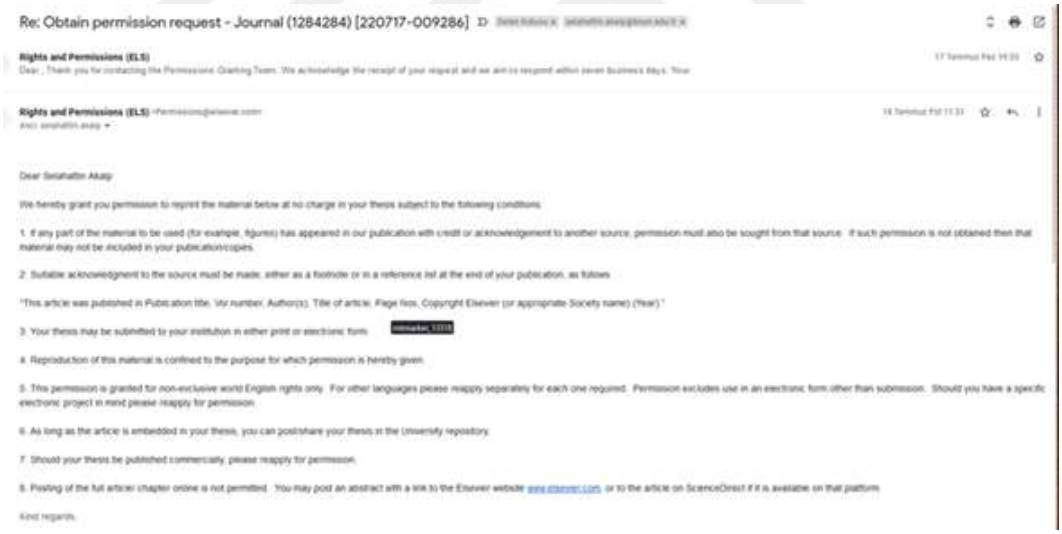

Re: Obtain permission request - Journal (1284284) [220717-009286]

Rights and Permissions (ELS)

Dear , Thank you for contacting the Permissions Granting Team. We acknowledge the receipt of your request and we aim to respond within seven business days. Your

Rights and Permissions (ELS)

Dear Selahattin Akalp

We hereby grant you permission to reprint the material below at no charge in your thesis subject to the following conditions.

1. If any part of the material to be used (for example, figures) has appeared in our publication with credit or acknowledgement to another source, permission must also be sought from that source. If such permission is not obtained then that material may not be included in your publication/copies.

2. Suitable acknowledgment to the source must be made, either as a footnote or in a reference list at the end of your publication, as follows:

"This article was published in Publication title, Vol number, Author(s), Title of article, Page Nos, Copyright Elsevier (or appropriate Society name) (Year)."

3. Your thesis may be submitted to your institution in either print or electronic form.

4. Reproduction of this material is confined to the purpose for which permission is hereby given.

5. This permission is granted for non-exclusive world English rights only. For other languages please reapply separately for each one required. Permission excludes use in an electronic form other than submission. Should you have a specific electronic project in mind please reapply for permission.

6. As long as the article is embedded in your thesis, you can post/share your thesis in the University repository.

7. Should your thesis be published commercially, please reapply for permission.

8. Posting of the full article/ chapter online is not permitted. You may post an abstract with a link to the Elsevier website www.elsevier.com, or to the article on ScienceDirect if it is available on that platform.

Kind regards,

Figure D.3. Permission-3.

Re: Obtain permission request - Journal (1284283) [220717-009208] ID

Rights and Permissions (ELS)
Dear , Thank you for contacting the Permissions Granting Team. We acknowledge the receipt of your request and we aim to respond within seven business days. Your

17 Temmuz Paz 19:24

Rights and Permissions (ELS) <Permissions@elsevier.com>
Alıcı: selahattin akalp

18 Temmuz Pzt 11:15

Dear Selahattin Akalp

We hereby grant you permission to reprint the material below at no charge in your thesis subject to the following conditions

1. If any part of the material to be used (for example, figures) has appeared in our publication with credit or acknowledgement to another source, permission must also be sought from that source. If such permission is not obtained then that material may not be included in your publication/copies.

2. Suitable acknowledgment to the source must be made, either as a footnote or in a reference list at the end of your publication, as follows:

"This article was published in Publication title, Vol number, Author(s), Title of article, Page Nos, Copyright Elsevier (or appropriate Society name) (Year)."

3. Your thesis may be submitted to your institution in either print or electronic form.

4. Reproduction of this material is confined to the purpose for which permission is hereby given.

5. This permission is granted for non-exclusive world English rights only. For other languages please reapply separately for each one required. Permission excludes use in an electronic form other than submission. Should you have a specific electronic project in mind please reapply for permission.

6. As long as the article is embedded in your thesis, you can post/share your thesis in the University repository.

7. Should your thesis be published commercially, please reapply for permission.

8. Posting of the full article/ chapter online is not permitted. You may post an abstract with a link to the Elsevier website www.elsevier.com, or to the article on ScienceDirect if it is available on that platform.

Kind regards,

Figure D.4. Permission-4.

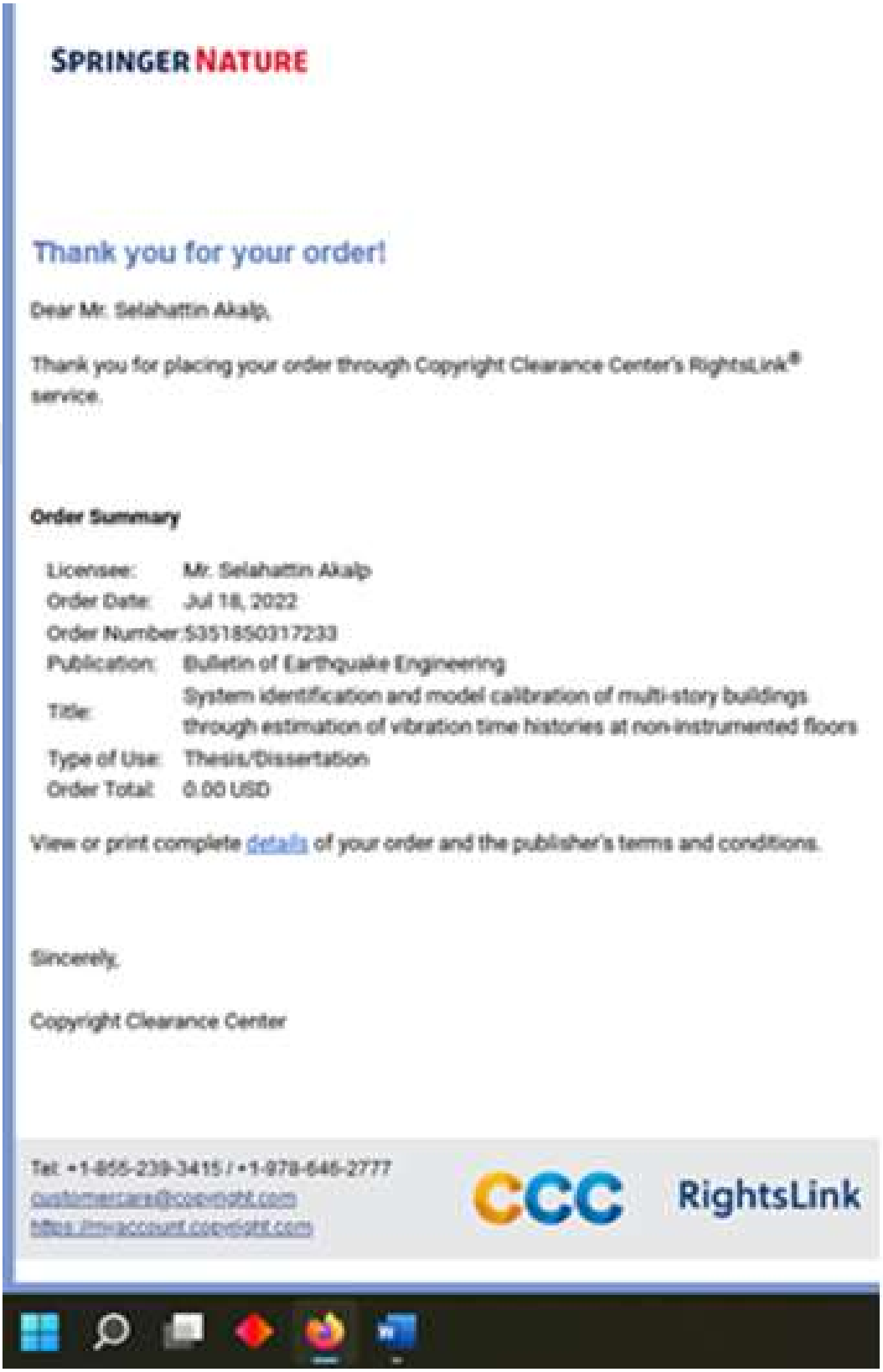

SPRINGER NATURE

Thank you for your order!

Dear Mr. Selahattin Akalp,

Thank you for placing your order through Copyright Clearance Center's RightsLink® service.

Order Summary

Licensee:	Mr. Selahattin Akalp
Order Date:	Jul 18, 2022
Order Number:	5351850317233
Publication:	Bulletin of Earthquake Engineering
Title:	System identification and model calibration of multi-story buildings through estimation of vibration time histories at non-instrumented floors
Type of Use:	Thesis/Dissertation
Order Total:	0.00 USD

View or print complete details of your order and the publisher's terms and conditions.

Sincerely,

Copyright Clearance Center

Tel: +1-855-239-3415 / +1-978-646-2777
customercare@copyright.com
https://myaccount.copyright.com

CCC RightsLink

Figure D.5. Permission-5.

ELSEVIER LICENSE
TERMS AND CONDITIONS

Sep 24, 2022

This Agreement between Mr. Selahattin Akalp ("You") and Elsevier ("Elsevier") consists of your license details and the terms and conditions provided by Elsevier and Copyright Clearance Center.

License Number	5385371221276
License date	Sep 10, 2022
Licensed Content Publisher	Elsevier
Licensed Content Publication	Soil Dynamics and Earthquake Engineering
Licensed Content Title	Prediction of building response at any level from recorded roof response: The Kanai–Yoshizawa formula revisited
Licensed Content Author	M. Ebrahimian,M.D. Trifunac,M.I. Todorovska
Licensed Content Date	Jan 1, 2016
Licensed Content Volume	80
Licensed Content Issue	n/a
Licensed Content Pages	10
Start Page	241
End Page	250

Figure D.6. Permission-6.